

PROGRESSIVE INTER-LAMINAR FATIGUE DAMAGE MODELLING AND  
ANALYSIS OF COMPOSITE STRUCTURES THROUGH A TWO-WAY  
GLOBAL/LOCAL COUPLING METHODOLOGY

A THESIS SUBMITTED TO  
THE GRADUATE SCHOOL OF NATURAL AND APPLIED SCIENCES  
OF  
MIDDLE EAST TECHNICAL UNIVERSITY

BY

BORAY DEĞERLİYURT

IN PARTIAL FULFILLMENT OF THE REQUIREMENTS  
FOR  
THE DEGREE OF DOCTOR OF PHILOSOPHY  
IN  
AEROSPACE ENGINEERING

FEBRUARY 2025



Approval of the thesis:

**PROGRESSIVE INTER-LAMINAR FATIGUE DAMAGE MODELLING  
AND ANALYSIS OF COMPOSITE STRUCTURES THROUGH A TWO-  
WAY GLOBAL/LOCAL COUPLING METHODOLOGY**

submitted by **BORAY DEĞERLİYURT** in partial fulfillment of the requirements  
for the degree of **Doctor of Philosophy in Aerospace Engineering, Middle East  
Technical University** by,

Prof. Dr. Naci Emre Altun  
Dean, **Graduate School of Natural and Applied Sciences**

Prof. Dr. Serkan Özgen  
Head of the Department, **Aerospace Engineering**

Assoc. Prof. Dr. Melin Şahin  
Supervisor, **Aerospace Engineering, METU**

**Examining Committee Members:**

Prof. Dr. Altan Kayran  
Aerospace Engineering Dept., METU

Assoc. Prof. Dr. Melin Şahin  
Aerospace Engineering Dept., METU

Prof. Dr. Erdem Acar  
Mechanical Engineering Dept., TOBB ETÜ

Prof. Dr. Demirkan Çöker  
Aerospace Engineering Dept., METU

Prof. Dr. Ferhat Kadioğlu  
Aerospace Engineering Dept., AYBÜ

Date: 19.02.2025

**I hereby declare that all information in this document has been obtained and presented in accordance with academic rules and ethical conduct. I also declare that, as required by these rules and conduct, I have fully cited and referenced all material and results that are not original to this work.**

Name Last name: Boray Deđerliyurt

Signature :

## **ABSTRACT**

### **PROGRESSIVE INTER-LAMINAR FATIGUE DAMAGE MODELLING AND ANALYSIS OF COMPOSITE STRUCTURES THROUGH A TWO- WAY GLOBAL/LOCAL COUPLING METHODOLOGY**

Değerliyurt, Boray  
Doctor of Philosophy, Aerospace Engineering  
Supervisor : Assoc. Prof. Dr. Melin Şahin

February 2025, 134 pages

Delamination and debonding are crucial failure modes in composite helicopter rotor components, demanding an accurate estimation of their growth and extent. A rapid and robust approach for analysing progressive fatigue delamination is essential to assess the propagation of interlaminar flaws.

Existing literature primarily confines progressive failure investigations to coupon scale due to substantial computation times and convergence challenges. The commonly observed strategy to tackle these issues involves utilising the global-local method. While global-local methods are prevalent in progressive damage computations, they are typically limited to static analyses; and the literature lacks global-local methods designed explicitly for progressive fatigue damage modelling.

Consequently, this study introduces a novel procedure for conducting extensive fatigue delamination analyses with a two-way coupling global-local method. This method applies the displacement field derived from the global model to the local model. Subsequently, the global model is updated iteratively based on internal nodal reactions of cohesive elements extracted from the local model.

The study presents the analysis results of the Double Cantilever Beam (DCB) model employing this method. The method gives consistent results with regular analyses and experimental findings. In 3D models with finer local mesh, the current method has a significant computational advantage over regular analyses.

This verified methodology is then applied to an element-level aerospace structure. The method's computational advantage and accuracy are also compared with the regular method, which shows its computational advantage in aerospace finite element analysis applications.

Keywords: Composites, Delamination, Cohesive Zone Method (CZM), Global-Local Coupling, Fatigue Analyses

## ÖZ

### **KOMPOZİT YAPILARDA İKİ YÖNDE BAĞLI GLOBAL/LOKAL YÖNTEM İLE İLERLEMELİ KATMANLAR ARASI YORULMA HASARININ MODELLENMESİ VE ANALİZİ**

Değerliyurt, Boray  
Doktora, Havacılık ve Uzay Mühendisliği  
Tez Yöneticisi: Doç. Dr. Melin Şahin

Şubat 2025, 134 sayfa

Kompozit helikopter rotor yapılarında, bütünlüğün korunması için delaminasyon (katmanlar arası ayrılma) ve yapışma hasarının ilerlemesinden kaçınılmalıdır. Bu nedenle bu yapılardaki delaminasyona açık bölgelerde hızlı ve doğru bir şekilde katmanlar arası hasar modellemesi yapılmasına ihtiyaç duyulmaktadır.

Ancak uzun hesaplama süreleri ve yakınsama sorunlarıyla karşılaşılması nedeniyle literatürdeki çalışmalar numune ölçeğiyle sınırlıdır. Bu sorunların ortadan kaldırılması için global-lokal yöntemler tercih edilmektedir. Global-lokal yöntemler literatürde yaygın olsa da, bu yöntemin kullanımı statik analizler ile sınırlıdır. Sonuçta literatürde yorulma yükü altında ilerlemeli hasar analizleri konusunda boşluk olduğu görülmektedir.

Bu çalışmada, yeni bir yaklaşımla iki yönde bağlanmış global-lokal yöntemle delaminasyon yorulma analizleri gerçekleştirilmiştir. Bu yöntemde, alt modelleme kullanılarak global modelden elde edilen yer değiştirme dağılımı lokal model sınırlarına uygulanmakta, ve buna ek olarak global model, lokal modelden elde edilen yapışkan eleman iç düğüm reaksiyon kuvvetlerine bağlı olarak

güncellenmektedir. İki model birbirine bağı olduğu için yakınsama sağlanana kadar tekrarlı analiz yapılması gerekmektedir.

Mevcut yöntemin doğrulanması için deneylerle desteklenmiş Çift Dirsekli Kiriş modelleri oluşturulmuş ve bu yöntemle elde edilen sonuçlar alışlagelmiş analiz yöntemleriyle ve deney sonuçlarıyla karşılaştırılmıştır. Bu yöntem, alışlagelmiş analiiz yöntemiyle ve deney verileriyle uyumlu sonuçlar vermiştir. Üç boyutlu analizlerde, özellikle sık ağ örgülü lokal modellerde, hatırı sayılır hesaplama avantajı elde edildiği görülmüştür.

Daha sonra kupon boyutunda doğrulanmış bu yöntem, bir havacılık yapısına uygulanmıştır. Sonuçlar alışlagelmiş yöntem ile karşılaştırılmış, benzer şekilde isabetli sonuçlar elde edildiği ve hesaplama süresinden tasarruf edildiği gösterilmiş, ve mevcut yöntemin havacılık Sonlu Elemanlar Analiz uygulamaları için de avantajlı olduğu sonucuna varılmıştır.

Anahtar Kelimeler: Kompozit, Katman Ayrılması, Yapışkan Arayüz Yöntemi, Global-Lokal Bağlılık, Yorulma Analizi

To my family

## ACKNOWLEDGMENTS

I would like to express my deepest gratitude to his supervisor Assoc. Prof. Dr. Melin Şahin for his guidance, advice, criticism, encouragement and insight throughout the research.

I would also like to thank Prof. Dr. Altan Kayran and Prof. Dr. Erdem Acar for their suggestions and comments during the Thesis Monitoring Committee meetings. I would also like to acknowledge Prof. Dr. Demirkan Çöker for his support and advice. I would like to express my gratitude to Prof. Dr Ferhat Kadiođlu for honouring my thesis defense meeting.

During my work in Turkish Aerospace, the technical assistance, endless support and friendship of my manager Murat Günel, my chief engineer Alperen Ayberk Işık and my colleagues Cansu Karataş Demircan, Berkin Çetinkaya and Seçkin Martin are gratefully acknowledged.

Finally, I must express my gratitude to my mother, Nimet Duyurucu; my father, Mehmet Deđerliyurt, his wife, Özlem Bozođlu Deđerliyurt; my grandmother, Bilge Deđerliyurt, and my love, Tuđçe Demir.

This work is supported and funded by Turkish Aerospace, Directorate of Rotary Wing Design in Helicopter Department.

## TABLE OF CONTENTS

ABSTRACT.....	v
ÖZ .....	vii
ACKNOWLEDGMENTS .....	x
TABLE OF CONTENTS.....	xi
LIST OF TABLES .....	xiv
LIST OF FIGURES .....	xvi
LIST OF ABBREVIATIONS .....	xxi
LIST OF SYMBOLS .....	xxii
CHAPTERS	
1 INTRODUCTION .....	1
1.1 Motivation.....	1
1.2 Objectives .....	3
1.3 Assumptions and Limitations .....	4
1.4 Scope and Outline .....	5
2 LITERATURE REVIEW .....	9
2.1 Introduction.....	9
2.2 Fatigue Analysis Methods.....	11
2.3 Progressive Failure Analysis.....	14
2.4 Delamination Modelling Approaches .....	14
2.4.1 Fracture Mechanics Approach .....	15
2.4.2 Cohesive Zone Model .....	18
2.5 Global-Local Method.....	19

3	STATIC ANALYSES BY TWO-WAY GLOBAL-LOCAL COUPLING	
	METHOD .....	27
3.1	Introduction .....	27
3.2	Verification of the Method with Double Cantilever Beam Analyses.....	42
3.2.1	Description of the Global-Local Finite Element Model.....	42
3.2.2	Baseline Solutions Supported by Experiments.....	43
3.2.3	Mesh Independency Study .....	46
3.2.4	The Effect of Selection of the Extent of the Local Region and Amount of Damage Propagation .....	51
3.2.5	Comparison of the Current Methodology with the Sub-Modelling Approach.....	55
3.2.6	Results and Discussions .....	57
3.3	Application of the Method in Analyzing Tension-Torsion Experiments	59
3.3.1	Test Setup .....	59
3.3.2	Finite Element Model .....	61
3.4	Experiment and Analyses Results .....	63
3.4.1	Stiffening Effect of Axial Force .....	69
3.5	Conclusions .....	72
4	FATIGUE ANALYSES BY TWO-WAY GLOBAL-LOCAL COUPLING	
	METHOD .....	75
4.1	Introduction .....	75
4.2	Description of the Global-Local Finite Element Model.....	79
4.3	Baseline Solutions .....	79
4.4	Mesh Independency Study .....	81

4.5	Comparison of the Current Methodology with the Sub-Modelling Approach.....	83
4.6	Results and Discussions .....	85
4.7	Conclusions.....	87
5	INTERLAMINAR FAILURE ANALYSES OF A T-JOINT STRUCTURE THROUGH THE TWO-WAY GLOBAL-LOCAL COUPLING METHOD .....	89
5.1	Introduction.....	89
5.2	Fatigue Analyses .....	90
5.3	Results and Discussions .....	94
5.4	Conclusions.....	98
6	CONCLUSIONS AND RECOMMENDATIONS .....	99
6.1	General Conclusions .....	99
6.2	Recommendation for Future Work .....	100
	REFERENCES .....	101
	APPENDICES.....	119
A.	Derivation of the Exact formulation of the DCB response.....	119
B.	Derivation of Global and Local Region Expressions of the Analytical DCB Model .....	121
C.	Supplementary Plots of Static DCB Response for Different Selection of Mesh Sizing at the Vicinity of Damage Region .....	124
D.	Derivation of Fatigue Response of the DCB Model.....	128
E.	Supplementary Plots of Fatigue DCB Response for Different Selection of Mesh Sizing at the Vicinity of Damage Region .....	129
	CURRICULUM VITAE.....	133

## LIST OF TABLES

### TABLES

Table 2-1 Preferred Fatigue Analysis Approaches in the Literature .....	13
Table 2-2 Finite Element Models of Various Structures in the Literature for Progressive Failure Analyses .....	15
Table 2-3 Global Local Methods Used in the Literature.....	22
Table 3-1. Calculation of Boundary and Cohesive Criteria .....	38
Table 3-2. Numerical Values of the DCB Model Parameters .....	39
Table 3-3. Exact Solutions of the Arm Reaction and Crack Length .....	40
Table 3-4. DCB Model Parameters for Mesh Size Determination.....	47
Table 3-5. DCB Model Arm Reaction Results for Different Local Mesh Sizes .....	50
Table 3-6. DCB Model Arm Reaction Differences for Different Local Mesh Sizes .....	50
Table 3-7. DCB Model Computational Performance for Different Local Mesh Sizes .....	50
Table 3-8. Selections of the Local Region's Extent.....	51
Table 3-9. Selections of the Expected Damage Propagation Length and Corresponding Arm Separations .....	51
Table 3-10. Summary of Arm Reaction Results under Maximum Arm Opening of 6.5 mm .....	58
Table 3-11 Summary of Arm Reaction Percent Differences Based on Analytical Solution Reference .....	58
Table 3-12 Pure Torsion and Tension-Torsion Specimens .....	59
Table 3-13. Comparison of Computational Effort .....	73
Table 4-1. DCB Model Arm Separation Boundary Conditions .....	80
Table 4-2. Mode-I Interface Parameters.....	80
Table 4-3. Summary of Arm Reaction Results .....	86
Table 4-4. Summary of Delamination Length Results .....	86
Table 4-5. Comparison of Computational Effort .....	87

Table 5-1. Skin and Stringer Stacking Sequences and Total Thicknesses [143]....	93
Table 5-2. Comparison of Computational Effort Reaction Force and Delamination Extent Results .....	97
Table 5-3 Comparison of Computational Effort .....	98

## LIST OF FIGURES

### FIGURES

Figure 1-1. General Structure of the Study .....	6
Figure 2-1. Typical Rotor Blade with Tapered Region of Spar (Adopted from [23]) .....	10
Figure 2-2. Typical Rotor Blade Section with Spar Bonded Joint Regions (Adopted from [24]) .....	10
Figure 2-3 Fatigue Life Curves: (a) a Typical S-N Curve [25] (b) a Typical da/dN- G Curve [26].....	12
Figure 2-4 Virtual Crack Closure Technique Application [26].....	17
Figure 2-5 Global-Local Model with 3 boundaries [2] .....	20
Figure 2-6. Global-Local Coupling by Averaging Stiffness Values of Global Cohesive Elements [1].....	24
Figure 2-7. Global-Local Coupling by Mapping Local Cohesive Stiffness Values to the Global Connector Elements and Global-Local DCB Model [22] .....	24
Figure 2-8. Global-Local Coupling by Submodelling approach with Global Model with Cohesive Elements with Coarser Mesh on a DCB model [125] .....	25
Figure 3-1 Cohesive Element Traction-Separation Behaviour .....	28
Figure 3-2 Two-Way Global-Local Coupling with the Damage Mapping Algorithm .....	31
Figure 3-3. Application of Damage Mapping .....	32
Figure 3-4. Application of Boundary Residuals.....	33
Figure 3-5. Distribution of Local Nodal Force on Corresponding Global/Auxiliary Nodes.....	34
Figure 3-6. One Iteration Loop of Two-Way Global-Local Coupling Methodology .....	35
Figure 3-7. Analytical DCB Model .....	39
Figure 3-8. Crack Length Result of Analytical DCB Model.....	41
Figure 3-9. Arm Reaction Result of Analytical DCB Model .....	41

Figure 3-10. Double Cantilever Beam Global-Local 3-D Finite Element Model ...	43
Figure 3-11. Double Cantilever Beam (DCB) Specimen .....	44
Figure 3-12. Selection of Critical SERR Based on MBT Formula.....	46
Figure 3-13. DCB Response for Different Mesh Sizes without Mesh Regularisation Assessed by Regular FEA (Mesh Size other than the local region is 1 mm) .....	47
Figure 3-14 DCB Response for Different Mesh Sizes with Mesh Regularisation (Mesh Size other than the local region is 1 mm) .....	49
Figure 3-15 Definition of Local Region Extent .....	51
Figure 3-16 Arm Reaction-Separation Plots for Different Local Region Extent ...	53
Figure 3-17 Computational Effort of Regular and Global-Local FEA for Different Damage and Local Region Extents .....	54
Figure 3-18 Computational Performance of Global-Local FEA to Regular FEA for Different Damage and Local Region Extents .....	54
Figure 3-19 Submodelling Method .....	55
Figure 3-20 Delamination Propagation Results of Regular Analyses, Submodelling Method and Two-Way Global Local Coupling Methodology.....	56
Figure 3-21 Arm Reaction versus Arm Separation Results.....	57
Figure 3-22 Tension-Torsion Specimen Dimensions .....	59
Figure 3-23 Tension-Torsion Test Setup .....	60
Figure 3-24 Delamination Failure.....	60
Figure 3-25 3D Beam under Tension-Torsion Model Geometry and Boundary Conditions .....	61
Figure 3-26 Elastoplastic Shear Responses .....	62
Figure 3-27 Thickness Sensitivity Results of T1 Specimens.....	64
Figure 3-28 Shear Stiffness Sensitivity Results of T1 Specimens.....	64
Figure 3-29 Fracture Toughness Sensitivity Results of T1 Specimens .....	65
Figure 3-30 ILSS Sensitivity Results of T1 Specimens.....	65
Figure 3-31 Local Failure of Cohesive Elements with a Depth of 5 mm .....	66
Figure 3-32 Torque vs Angle of Twist Plots of T1 Specimens .....	67

Figure 3-33 Torque vs Angle of Twist Plots of T3 Specimens .....	68
Figure 3-34 Torque vs Angle of Twist Plots of T3 Specimens .....	69
Figure 3-35 Effect of axial force on Hybrid (T3 and TT3) specimens .....	71
Figure 3-36 Effect of Axial Force on Distribution of Angle of Twist and its Span-wise Derivative .....	72
Figure 4-1 Cohesive Element Fatigue Response [26] .....	77
Figure 4-2 Typical G vs da/dN Plot for Mode I (DCB), Mode II (ENF) and Mixed Mode (MMB) Failure [28] .....	77
Figure 4-3 Actual Cyclic Load and Applied Load Envelope in FEA .....	78
Figure 4-4. Double Cantilever Beam Finite Element Model .....	80
Figure 4-5 DCB Fatigue Response for Different Mesh Sizes without Mesh Regularisation (Mesh Size other than the local region is 1 mm) .....	82
Figure 4-6 DCB Fatigue Response for Different Mesh Sizes with Mesh Regularisation (Mesh Size other than the local region is 1 mm) .....	83
Figure 4-7 Damage of Cohesive Elements for the Fatigue Analyses.....	84
Figure 4-8 Arm Reaction Plots of the Fatigue Analyses .....	85
Figure 5-1 T-Joint Pull-off Quasi-Static Test Setup in the Study of Ma et al. [143] .....	89
Figure 5-2 Failure Modes of the T-Joint Specimen after Pull-out Load [143] .....	90
Figure 5-3 Comparison of Regular Analyses with the Results of Ma et al. [143] ..	91
Figure 5-4 Global, Auxiliary and Local Finite Element Models of T-Joint Structure .....	92
Figure 5-5 Boundary Conditions Applied on the Global Finite Element Model of T-Joint Structure.....	92
Figure 5-6 Ply Layup Directions of the T-Joint .....	93
Figure 5-7 Applied Cyclic Displacement .....	93
Figure 5-8 Fatigue response of the T-Joint under cyclic displacement load.....	94
Figure 5-9 Damage States under Specified Cycles .....	95
Figure 5-10 Comparison of Fatigue Response of the T-Joint and Damage State at One-Millionth Cycle.....	96

Figure 5-11 Definition Debonding Propagation Paths.....	97
Figure C-1 Static Response of the DCB Model with Local Mesh Size Selection of 1 mm without Mesh Regularisation .....	124
Figure C-2 Static Response of the DCB Model with Local Mesh Size Selection of 0.5 mm without Mesh Regularisation .....	124
Figure C-3 Static Response of the DCB Model with Local Mesh Size Selection of 0.25 mm without Mesh Regularisation .....	125
Figure C-4 Static Response of the DCB Model with Local Mesh Size Selection of 0.1 mm without Mesh Regularisation .....	125
Figure C-5 Static Response of the DCB Model with Local Mesh Size Selection of 1 mm with Mesh Regularisation .....	126
Figure C-6 Static Response of the DCB Model with Local Mesh Size Selection of 0.5 mm with Mesh Regularisation .....	126
Figure C-7 Static Response of the DCB Model with Local Mesh Size Selection of 0.25 mm with Mesh Regularisation .....	127
Figure C-8 Static Response of the DCB Model with Local Mesh Size Selection of 0.25 mm with Mesh Regularisation .....	127
Figure E-1 Fatigue Response of the DCB Model with Local Mesh Size Selection of 1 mm without Mesh Regularisation .....	129
Figure E-2 Fatigue Response of the DCB Model with Local Mesh Size Selection of 0.5 mm without Mesh Regularisation .....	129
Figure E-3 Fatigue Response of the DCB Model with Local Mesh Size Selection of 0.25 mm without Mesh Regularisation .....	130
Figure E-4 Fatigue Response of the DCB Model with Local Mesh Size Selection of 0.1 mm without Mesh Regularisation .....	130
Figure E-5 Fatigue Response of the DCB Model with Local Mesh Size Selection of 1 mm with Mesh Regularisation .....	131
Figure E-6 Fatigue Response of the DCB Model with Local Mesh Size Selection of 0.5 mm with Mesh Regularisation .....	131

Figure E-7 Static Response of the DCB Model with Local Mesh Size Selection of 0.25 mm with Mesh Regularisation.....	132
Figure E-8 Fatigue Response of the DCB Model with Local Mesh Size Selection of 0.1 mm with Mesh Regularisation.....	132

## LIST OF ABBREVIATIONS

### ABBREVIATIONS

CZM	Cohesive Zone Model
DCB	Double Cantilever Beam
LEFM	Linear Elastic Fracture Mechanics
SERR	Strain Energy Release Rate
SIF	Stress Intensity Factor
UMAT	User Material
VCCT	Virtual Crack Closure Technique

## LIST OF SYMBOLS

### SYMBOLS

$a$	Crack/Delamination Length
$a_0$	Initial Crack/Delamination Length
$b$	Width
$C$	Paris Law Coefficient
$D$	Flexural Rigidity per width
$\mathcal{D}$	Cohesive Damage Parameter
$EI$	Flexural Rigidity
$F$	Force
$G_I$	Mode I Strain Energy Release Rate
$G_{II}$	Mode II Strain Energy Release Rate
$G_{III}$	Mode III Strain Energy Release Rate
$G_C$	Critical Strain Energy Release Rate / Fracture Toughness
$G_T$	Total Strain Energy Release Rate
$G_{th}$	Threshold Strain Energy Release Rate
$h$	DCB arm Thickness
$J$	Jacobian
$K$	Cohesive Elastic Stiffness
$L$	Length
$m$	Paris Law Exponent

$N$	Cycle
$\mathcal{N}$	Shape Function
$R$	Load Ratio
$T$	Traction
$u$	x-Displacement
$v$	y-Displacement
$w$	z-Displacement
$x$	x-Coordinate
$y$	y-Coordinate
$z$	z-Coordinate
$\delta$	Separation
$\Delta$	DCB Arm Separation
$\Delta a$	Crack Propagation
$\Delta G$	Peak to Peak Strain Energy Release Rate
$\chi h$	Crack Length Correction



# CHAPTER 1

## INTRODUCTION

### 1.1 Motivation

Composite structures have flaws due to manufacturing imperfections such as disbonding and weak bonds, delaminations, porosity, and voids. These flaws cannot be avoided during manufacturing. The growth of these inter-laminar flaws may result in significant stiffness drop and catastrophic failure. Therefore, severe delamination/debonding propagation must be avoided under static and fatigue operational loads to preserve the structural integrity of composite rotor components. Hence, layer-to-layer static and fatigue damage modelling is necessary for proper sizing in regions prone to delamination in these structures. However, due to the size of the components, long computation times are encountered.

In progressive interlaminar damage calculations for aviation structures, the Cohesive Zone Model (CZM) is a preferred approach due to its ability to model damage initiation, formation, and propagation [1]. However, this method, mainly when applied to large-scale models such as helicopter rotor blades, results in long computation times due to its requirement for a dense mesh and the modelling of material softening behaviour that leads to instability. Therefore, in the literature, progressive failure analyses are limited to coupon scale in general.

The commonly observed strategy to tackle these issues involves utilising the global-local method. The global-local modelling approach, in general, in the literature, is known as the sub-modelling or sub-structure approach, depending upon the computational procedure [2].

The substructure (or super element) method is a mathematical coupling method in which global and local stiffness matrices are coupled by static condensation

(Guyan's reduction) [2,3]. This method is helpful for linear elastic problems. However, non-linear problems require updating the global stiffness matrix, which results in complicated calculations [3-9].

The sub-modelling approach involves constructing a simplified global model and a detailed local model (i.e., sub-model) of the critical region. The displacement field obtained from the global model is applied to the boundary of the local model, and detailed analyses are performed in the local model [2]. This way, detailed damage analyses are carried out in the smaller local model instead of running the entire model, leading to computational time savings. In the sub-modelling method, although the local model depends on the global displacement field, the global model is not sensitive to local response. Therefore, sub-modelling is a one-way global-local coupling method. This method is preferred in progressive failure analysis [11-16] and micro-meso-macro scale modelling applications [11,17,18].

To eliminate the violation of boundary equilibrium, boundary residuals are applied to the global model iteratively in the studies of Whitcomb and Woo [19-21] and Gossellet et al.[10]. Application of boundary residual makes the global-local method two-way coupled as boundary residual on the global model is dependent on the solution of the local model. However, this method leads to long computation times and convergence issues in damage analyses, creating high stiffness changes. Therefore, in addition to the boundary residuals, the global model must be updated according to the damage condition in the local model. When the global model is updated, the analyses in the local model are refreshed, and then the global model is updated again. Global-local analyses are iteratively conducted until the specified criteria are met.

In the literature, local models are generally connected to the global model with a displacement condition (i.e., the Sub-modelling method), as previously described. However, there are different approaches to connecting the global model to the local one (i.e., updating the global one).

On the other hand, none of the studies in the literature cover global-local fatigue analysis, as explained in detail in Chapter 2. This study covers a two-way global local coupling methodology, which does not suffer from the lack of boundary equilibrium and is more straightforward to apply for cohesive elements for static and fatigue interlaminar progressive damage modelling.

The newly developed two-way global-local coupling methodology for progressive interlaminar damage modelling will shortly thereafter be called “the method” or “the methodology.”

## **1.2 Objectives**

This study aims to develop an accurate and computationally efficient interlaminar damage modelling methodology without convergence difficulties.

The well-known Double Cantilever Beam (DCB) model, the simplest for interlaminar damage calculations with closed-form solutions, shows the method's accuracy through static analyses. Analytical solutions and regular analysis results supported by experiments are baseline solutions for the new global-local method. This method is verified by showing consistent results with regular analyses and closed-form solutions.

The verified method is then applied to analyses of quasi-static Tension-Torsion experiments in which delamination failure occurs. Similarly, the method is verified by showing consistent results with regular analyses.

The method is then extended for the fatigue analyses. Although the cohesive material response formulation is available in commercial software such as Abaqus, fatigue formulation is lacking. Therefore, this study also covers the User Material (UMAT) subroutine that drives the fatigue material response of cohesive elements.

The DCB model under cyclic loading then verifies the extended method with the subroutine. The closed-form solutions and regular analysis results are the method's

baseline solutions. Consistent results with regular analyses and closed-form solutions also verify the method.

This verified methodology is then applied to T-Joint structure models. The method's computational advantage and accuracy are compared with the regular method, which shows its computational advantage in aerospace applications.

### **1.3 Assumptions and Limitations**

The list below gives all assumptions and limitations in the dissertation:

- Material interface modelling through experiments is limited to static Mode I parameters through DCB experiments.
- Softening region of cohesive element material response is shape independent, provided that the area under the traction-separation response is equal to critical SERR (i.e. fracture toughness).
- The method requires tie constraints between the substrates in the global model. Closed delamination requires splitting the host material into two or more, depending upon the number of layers damaged, and tying them back.
- The method is applied to linear solid brick elements only in 3D Finite Element Modelling (FEM).
- The method cannot be used with the Virtual Crack Closure Technique (VCCT) formulation as models suffer from convergence difficulties due to contact formulation.
- Fatigue response is based on maximum loading with a specified load ratio  $R$ . Although geometric non-linearity is considered in the maximum loading condition, all stress and displacement distributions have spatially independent constant minimum to maximum ratios equal to load ratio ( $R$ ).

## 1.4 Scope and Outline

The flowchart in Figure 1-1 summarises the scope of the study. This study mainly covers verifying the methodology and its aerospace applications. The verification is performed by the Double Cantilever Beam Global-Local Finite Element Analyses. Then, the verified method is applied to the Tension-Torsion experiment models and the T-joint model.

Initially, the DCB model under quasi-static loading is considered for verification in static analysis. Mode-I fracture toughness, necessary for cohesive elements, is extracted from the static DCB experiments. Then, global-local FEA is performed and compared with closed-form solutions and the results of regular FEA. Moreover, the computational performance of the method is shown by comparing it with that of the regular FEA.

The verified methodology is then applied to quasi-static Tension-Torsion experiment models. Unlike the DCB model, the failure depends on interlaminar shear strength (ILSS) and fracture toughness. Moreover, high material non-linearity is observed in shear response. Therefore, elastic-plastic shear response is included in the modelling. The results are compared with regular analysis, and the method's computational advantage is shown.

The following procedure incorporates fatigue analysis into the method. Instead of pseudo-time, analyses are driven by number cycles. In ABAQUS software, cohesive elements with fatigue material modelling are not available. Therefore, the User Material (UMAT) subroutine is included in the method. The global-local FEA of the DCB under cyclic load is also performed. The results are compared with those of closed-form solution and regular FEA similarly. Moreover, the computational performance of the method is also shown by comparing it with that of regular FEA.

The verified fatigue methodology is then applied to a T-Joint model, an element-level aerospace structure. The results are compared with regular analysis, and the method's computational advantage is shown in aerospace applications.

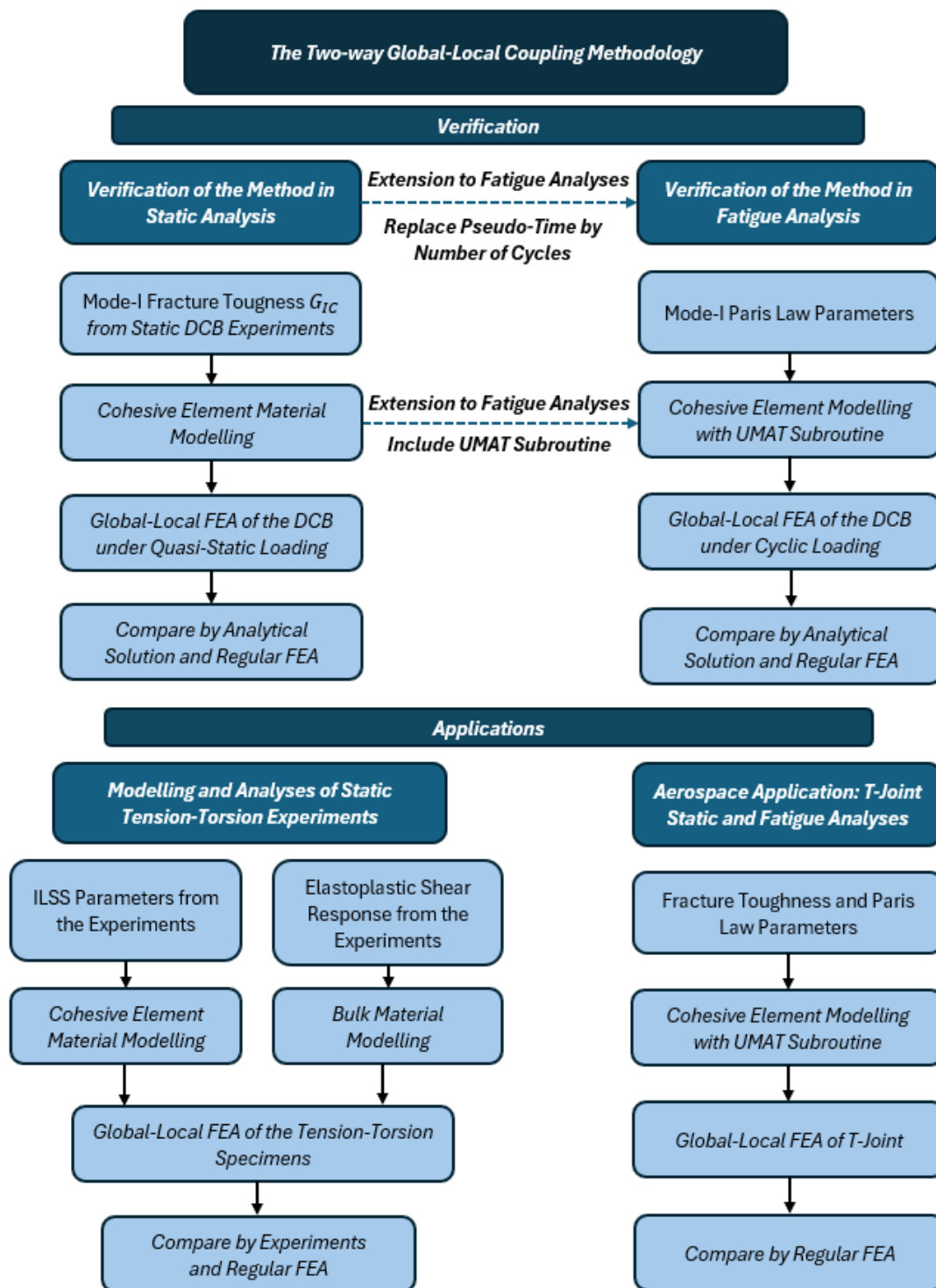


Figure 1-1. General Structure of the Study

The structure of the thesis is summarised in the following paragraphs.

Chapter 2 shows the literature review concerning the subjects of this study. First, this section overviews the methods of fatigue analysis. Progressive damage methods are also examined in this section. Progressive interlaminar damage analysis studies are the main scope. The survey shows that progressive failure studies are on a coupon scale. On the other hand, the global-local method is preferred for damage modelling applications in larger structures. Thus, this section also classifies global-local coupling methods and summarises studies concerning these. This section also shows the gap in the literature on the global-local interlaminar fatigue damage modelling.

Chapter 3 introduces the methodology with static analyses. This chapter verifies the method with application on a well-known DCB specimen, which is also presented with experimental data for cohesive material formulation. The results of the current method are compared with those of the regular ones, as well as analytical solutions and experimental data, which verifies the current proposed method. Computational advantage is also assessed. Moreover, this chapter presents the current method applied to the application of tension-torsion experiments. The results and computational performance of the method are also assessed.

Chapter 4 introduces the methodology extension to fatigue analyses. This chapter verifies the extended method with application to the DCB model under cyclic loading. The results of the current method are compared with those of the regular and analytical ones, which verify the current proposed method.

Chapter 5 shows the method for the aerospace application of the T-joint structure. The results show that the current method has a superior computational advantage in aerospace Finite Element Modelling applications.

Chapter 6 presents this study's ultimate conclusions. It explains what has been accomplished, restates the thesis objective, and discusses the research outcomes. Additionally, it offers recommendations for future work. The key findings from the entire study are summarised, and further study suggestions are provided.



## CHAPTER 2

### LITERATURE REVIEW

#### 2.1 Introduction

This chapter briefly outlines literature studies concerning the scope of the study. It provides fatigue analysis methods appropriate for interlaminar damage analyses. Moreover, it presents an overview of progressive failure studies and shows that it is generally on a coupon scale.

Spar is the primary load-carrying member of the rotor blade and undergoes extremely high cyclic loads (in the order of billion cycles). Composite structures have flaws due to manufacturing imperfections such as disbondings and weak bonds, delaminations, porosity, and voids. These flaws cannot be avoided during manufacturing. The growth of these inter-laminar flaws may result in catastrophic failure.

Figure 2-1 shows the delamination and debonding critical section of a spar (pink region), tapered with ply drop-offs at the blade root region. Moreover, skin, outer wrap, erosion shield, and other adjacent regions of the spar are critical for debonding.

Figure 2-2 shows the debonding crucial section of a spar, which is at a constant cross-section blade region. The spar is connected to adjacent components by bonded joints, which makes the spar debonding critical at blade sections.

Fatigue failure progression at critical sections has to be estimated to guarantee structural integrity under fatigue load. On the other hand, regular progressive failure analyses of large structures such as spar sections require massive computation times, and convergence issues may be encountered. Most progressive failure analysis

studies in the literature are on the coupon scale, and few large-scale analyses are available.

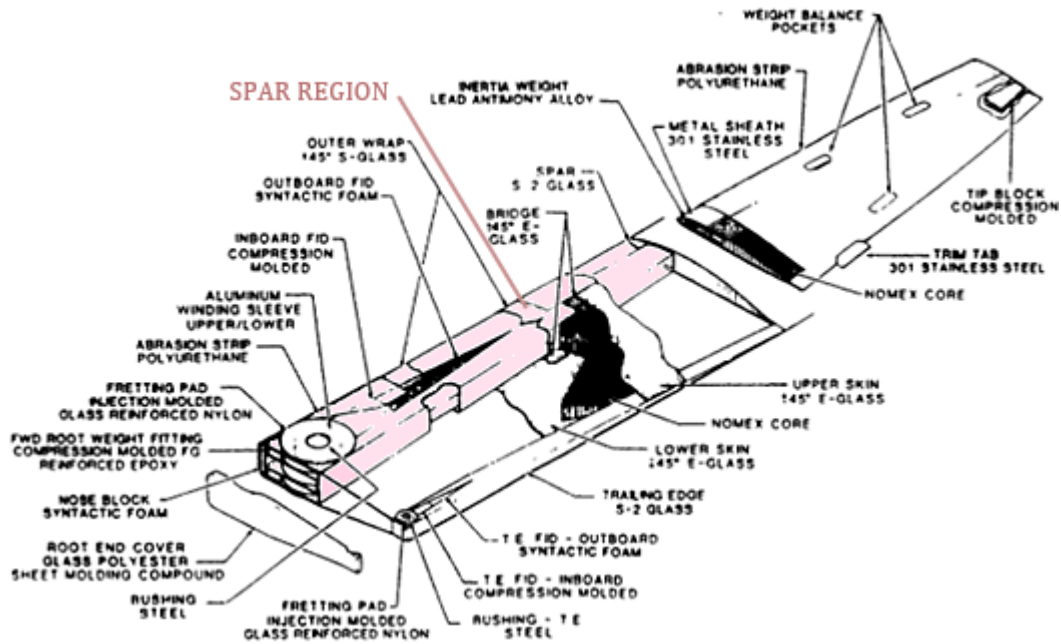


Figure 2-1. Typical Rotor Blade with Tapered Region of Spar (Adopted from [23])

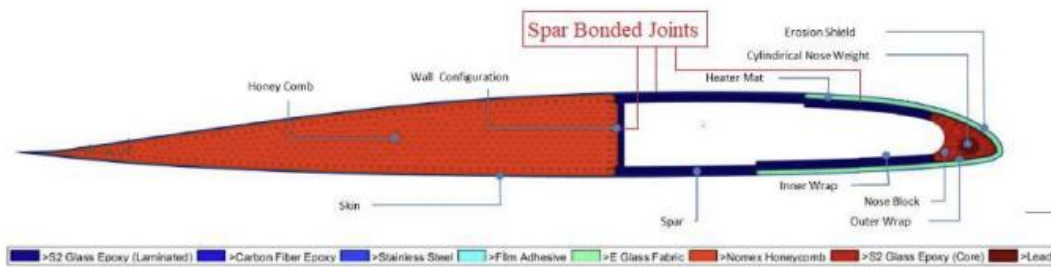


Figure 2-2. Typical Rotor Blade Section with Spar Bonded Joint Regions (Adopted from [24])

## 2.2 Fatigue Analysis Methods

In fatigue life computation methods, two approaches are preferred widely in the literature:

- S-N method: S is traditionally alternating or maximum stress. It can also be strain, displacement, force, strain energy release rate, etc. S can be considered a strength or allowable load. To satisfy the life requirement, the component, coupon, or selected zone must have that parameter at the desired cycle N below the S-N curve.
- da/dN-G (or K) method: G or K is either Strain Energy Release Rate (SERR) or Stress Intensity Factor (SIF), depending on the type of crack. G or K parameters can be either maximum or alternating and can be normalised or non-normalised depending on the selected formulation.

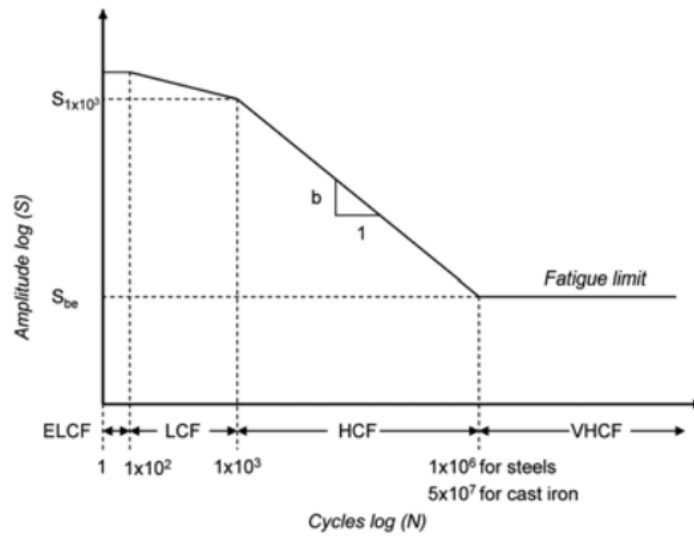
Table 2-1 lists fatigue analysis studies. For interlaminar damage studies, da/dN-G and  $G_{\text{onset}}-N$  methods are preferred with coupon level tests, Mode-I DCB, Mode-II ENF and Mixed Mode MMB. The  $G_{\text{onset}}-N$  method is also an S-N method based on delamination propagation onset calculated by compliance increase of the coupons by %1 or %5 according to ASTM standards. These approaches are also preferred in element-level interlaminar damage studies of ply drop-off specimens.

On the other hand, da/dN-K methods are generally preferred in transverse crack applications in isotropic and composite materials. Calculating SIF (K) is an issue in interlaminar problems of composites; therefore, it is not preferred.

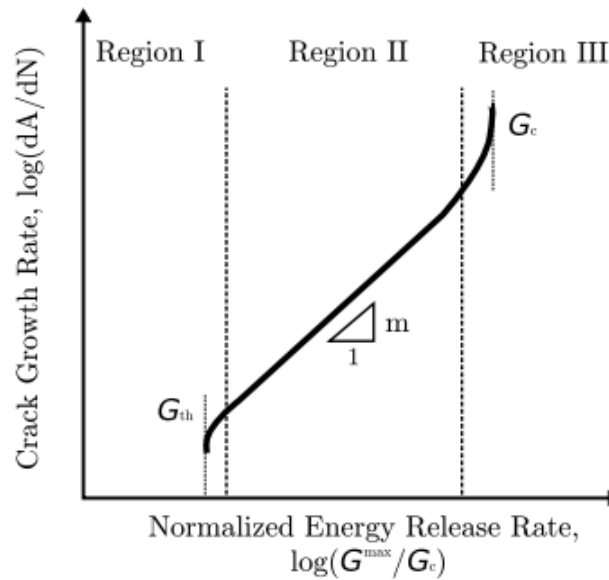
The last column of Table 2-1 shows S-N method studies. S is any strength or allowable parameter except SERR (shown separately in the 2<sup>nd</sup> column for interlaminar methods). In coupon scale, most studies concerning composite materials include material tests with plain laminate to extract S-N curves. Component-level S-N methods are also available in the literature but not listed since these studies are out-of-scope.

In conclusion,  $da/dN$  vs.  $G$  and  $G_{onset}$  vs.  $N$  approaches are preferred in this study for delamination propagation and delamination onset, respectively.

Figure 2-3(a) shows a typical S-N curve, and Figure 2-3(b) shows a typical  $da/dN$  vs.  $G$  curve.



(a)



(b)

Figure 2-3 Fatigue Life Curves: (a) a Typical S-N Curve [25] (b) a Typical  $da/dN$ - $G$  Curve [26]

Table 2-1 Preferred Fatigue Analysis Approaches in the Literature

	<b>da/dN vs. G</b>	<b>G<sub>onset</sub> - N</b>	<b>da/dN vs. K</b>	<b>S - N</b>
Mode I Delamination Specimen (DCB)	[26] [27] [28] [29] [30] [31] [32] [33] [34]	[31] [34]	[27] [35]	
Mode II Delamination Specimen (ENF)	[26] [28] [29] [30] [36] [37]	[38]		
Mixed Mode Delamination Specimen (MMB)	[26] [28] [29] [30] [31] [39] [40] [41]	[42]		
Notched Laminate (with a hole or crack)	[43]		[44] [45] [46] [47] [48] [49]	[37]* [44] [45] [46] [50]
Plain Laminate				[42] [44] [51] [52] [53] [54] [55] [56] [57] [58] [59] [60]
Bolted Joint				[61]
After Impact Fatigue Specimens				[62] [63]
Single Lap Bonded Joint				[64]
Bonded Repair Patch Specimen	[65] [66]			
Tubular Bonded Joint				[67]
Ply Drop-off Specimen	[66]	[68] [69]		[68]* [69]* [70]

\* Based on crack/delamination onset

### **2.3 Progressive Failure Analysis**

Progressive failure analysis is a computational method employed in structural engineering and materials science to forecast the gradual progression of damage and failure in intricate systems. It entails simulating the initiation and propagation of damage within a structure or material across different loading scenarios. Its objective is to forecast the sequence of events culminating in failure, considering the interplay among various failure modes and material responses.

Progressive failure analysis (PFA) of composite materials typically differentiates between intralaminar and interlaminar failure modes, which is essential for comprehending and forecasting the behaviour of laminated composites. Intralaminar failure modes manifest within individual layers (laminae) of the composite laminate, encompassing fibre breakage, matrix cracking, and fibre-matrix debonding. On the other hand, interlaminar failure modes occur between adjacent layers (plies) of the composite laminate and include delamination and debonding.

On the other hand, regular progressive failure analyses of large structures such as rotor components require massive computation times, and convergence issues may be encountered. In Table 2-2, most of the progressive failure analysis studies in the literature are in coupon scale in general. Few large-scale analyses are available in the literature.

### **2.4 Delamination Modelling Approaches**

The procedures used for the numerical simulation of the delamination can be divided into two groups.

The first group is based on the direct application of Fracture Mechanics. The Virtual Crack Closure Technique (VCCT) is preferred in delamination propagation studies.

The second method formulates the problem within the framework of Damage Mechanics. Cohesive elements or surfaces are used, and damage formulation is embedded into the cohesive material.

Table 2-2 Finite Element Models of Various Structures in the Literature for Progressive Failure Analyses

		Type of Progressive Failure Analysis		
		Intralaminar	Interlaminar	Intralaminar and Interlaminar
Structure	Open Hole/Notched/Cracked Specimen	[43] [71] [72] [73] [74] [75] [76] [77] [78] [79] [80] [81] [82] [83] [84] [85]		[29] [51] [86] [87] [88] [89] [90] [91] [92]
	Filled Hole/ Pin Joint Specimen	[83] [85] [93]		[88] [94]
	Plain Laminate	[42] [74] [77] [84] [95] [96] [97] [98]		[99]
	Curved Laminate	[100]	[101]	[102]
	DCB, ENF, MMB Delamination Specimens		[26] [39] [103] [104] [105] [106] [107] [108] [109] [46]	
	Tapered (Drop-off) Specimens	[97]	[69] [110]	[99]
	Bonded Joint Specimens		[65]	
	Stiffener Joint	[111]	[1] [72] [112]	
	Pressure Vessel			[113]
	Wind Turbine Blade Section			[114]
	Helicopter Main Rotor Blade Root			[115]

#### 2.4.1 Fracture Mechanics Approach

Linear Elastic Fracture Mechanics (LEFM) is an effective method in applications where material non-linearities are neglected. J-integral methods are preferred to calculate SERR to estimate the onset of delamination. This method requires defining a possible crack direction.

On the other hand, the VCCT method is also preferred in damage propagation estimations. The Virtual Crack Closure Technique (VCCT) is a widely used numerical method in fracture mechanics for predicting crack growth and estimating energy release rates. The Virtual Crack Closure Technique (VCCT) operates on the principle of Irwin that the energy needed to close a crack is equivalent to the energy released when the crack grows. This method is especially valuable in finite element analysis (FEA) for simulating crack propagation in different materials and structures.

Rybicki and Kanninen [116] first introduced VCCT in the late 1970s. Using finite element analysis, they devised a method to calculate the energy release rate for cracks in linear elastic materials. Their pioneering work established the foundation for VCCT by introducing finite element analysis for calculating energy release rates for crack growth.

In the 1980s, researchers such as Rybicki and Kanninen [116] and others expanded VCCT to more complex geometries and loading conditions, refining the method to enhance its accuracy and applicability. In 1987, I.S. Raju [117] improved the accuracy of VCCT by introducing more refined finite element models and addressing issues related to mesh sensitivity and element size. In 2004, R. Krueger [118] provided a comprehensive review of VCCT, covering its theoretical background, implementation in finite element codes, and applications in composite materials.

VCCT has been widely employed to study delamination and crack propagation in composite materials, aiding in predicting failures and improving composite structure designs. In the aerospace industry, the method predicts the growth of fatigue cracks in aircraft components, ensuring safety and reliability. Additionally, VCCT is utilised to assess the structural integrity of bridges, buildings, and other civil infrastructure by predicting crack growth and potential failure points.

However, this method requires an initial crack, as it cannot estimate the onset of delamination. Compared to the Cohesive Zone Model (CZM), the VCCT method is more mesh-independent. It is based on Irwin's assumption that the energy released

during infinitesimal crack propagation equals the work needed to close the crack to its original size. The strain energy release rate (SERR) components are calculated using the nodal responses adjacent to the crack tip, as described by Turon [26] according to expressions given by Eq.(2-1) to (2-3) according to Figure 2-4.

$$G_I = \frac{1}{2b\Delta a} F_{cd}^y (v_c - v_d) \quad (2-1)$$

$$G_{II} = \frac{1}{2b\Delta a} F_{cd}^x (u_c - u_d) \quad (2-2)$$

$$G_{III} = \frac{1}{2b\Delta a} F_{cd}^z (w_c - w_d) \quad (2-3)$$

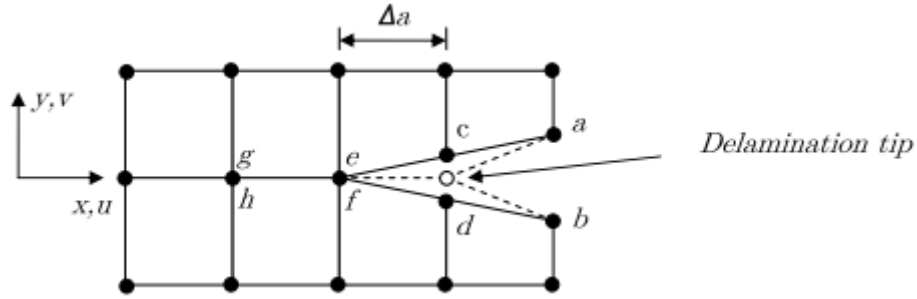


Figure 2-4 Virtual Crack Closure Technique Application [26]

Force components are calculated in the previous increment just before nodes c and d are released. Displacement components are calculated in the current increment, where nodes c and d are just released. However, this requires successive increments to be small. Instead, Rybicki and Kanninen [116] assume that nodal forces between c and d are approximated by nodal forces between e and f, which solves SERR values at a single increment as given by Eq.(2-4) to (2-6).

$$F_{cd}^x = F_{ef}^x \quad (2-4)$$

$$F_{cd}^y = F_{ef}^y \quad (2-5)$$

$$F_{cd}^z = F_{ef}^z \quad (2-6)$$

In Abaqus software, the VCCT method is compatible with fatigue (da/dN) formulation. Although critical SERR values are mode-dependent, fatigue parameters are mode-independent in the software, which is a significant limitation. Moreover,

High-fidelity simulations using VCCT can be computationally expensive, particularly for large-scale problems. It is introduced by contact formulation, and its initiation may lead to divergence.

#### **2.4.2 Cohesive Zone Model**

Another approach to numerically simulate delamination can be developed within the Damage Mechanics framework. Models formulated using Damage Mechanics adopt the cohesive crack model, where the cohesive damage zone forms near the crack front. This zone represents the damage progression as the crack propagates through the material.

The Cohesive Zone Model (CZM) is a computational method in fracture mechanics that simulates the initiation and growth of cracks. It uses a traction-separation law to define the relationship between stresses and displacements in the cohesive zone ahead of a crack tip, allowing for predicting fracture behaviour in different materials. The Cohesive Zone Model (CZM) plays a crucial role in fracture mechanics by predicting the initiation and propagation of cracks across various materials. Despite challenges such as parameter identification and computational costs, continuous research efforts are improving its accuracy, applicability, and efficiency, thereby maintaining its relevance in modern engineering applications.

Cohesive damage zone models establish a relationship between tractions and displacement jumps at an interface where a crack could develop. Damage initiation is linked to the interfacial strength, represented by the maximum traction  $\tau_0$  in the traction-displacement jump relationship. As the cumulative energy release, characterised by the area under the traction-displacement jump curve, reaches the fracture toughness  $G_c$ , the traction decreases to zero, forming new crack surfaces. This process reflects how cracks propagate and evolve within materials under mechanical loading.

The Cohesive Zone Model (CZM) was first introduced by Barenblatt [119] and Dugdale [120] in the early 1960s. Barenblatt [119] introduced the concept of cohesive forces to model brittle fracture, establishing the foundation for CZM. Dugdale [120] adopted a similar approach for ductile materials. Dugdale [120] developed a cohesive model specifically for ductile materials, offering an alternative approach to conventional fracture mechanics. In the 1980s, CZM gained popularity through the contributions of Needleman [121], who expanded the model to encompass more intricate materials and fracture processes, integrating it into finite element analysis (FEA). Needleman [121] expanded CZM to include plasticity and other complex behaviours, incorporating the model into finite element analysis (FEA).

Determining cohesive zone parameters such as traction and separation can be challenging and involves extensive experimentation. High-fidelity simulations using CZM can be computationally demanding, especially for large-scale problems. The accuracy of CZM is significantly affected by mesh size and quality, requiring meticulous mesh design. Compared to VCCT, CZM generally necessitates smaller mesh sizes.

Cohesive elements visualise stress, separation, and damage parameters. CZM is integrated into material models within continuum elements or surfaces, unlike contact formulations. This integration ensures that CZM does not encounter divergence issues when incorporated into models.

## **2.5 Global-Local Method**

Global-local modelling methods have been developed to reduce computational time. The global-local modelling approach, in general, in the literature, is known as the sub-modelling and sub-structure approach, depending upon the computational procedure [2]. Sub-modelling and substructure methods are mostly preferred

approaches in the literature [2,122-124]. These methods are discussed in a typical model shown in Figure 2-5.

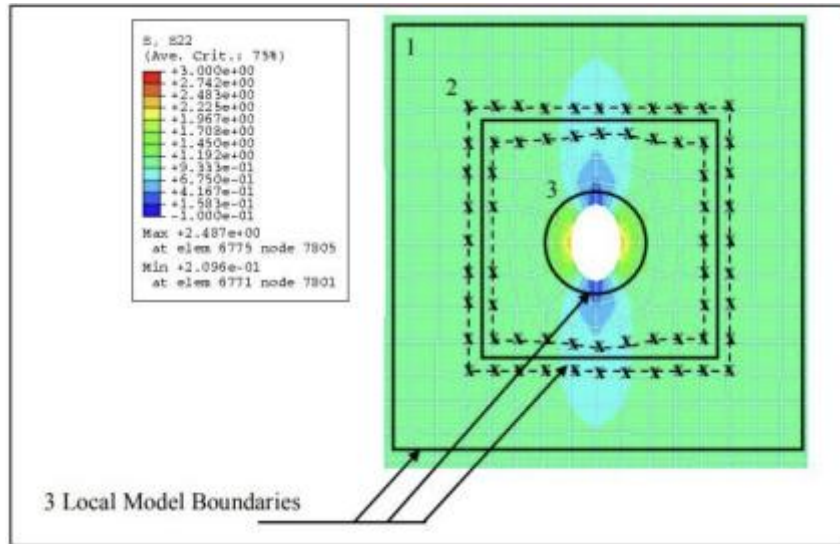


Figure 2-5 Global-Local Model with 3 boundaries [2]

In Figure 5, Boundary 1 is selected as the global model boundary, and Boundary 2 encloses the local region. For the sake of simplicity, Boundary 3 will be ignored.

The sub-structure (or super element) method is a mathematical coupling method where global and local stiffness matrices are coupled by the Static Condensation (Guyan's reduction) method [2,124]. This method is helpful for linear elastic problems. However, for non-linear problems, the method requires updating the global stiffness matrix, which results in complicated calculations, as shown in the studies [3-10]. In the substructure method, the region enclosed by Boundary 1 and Boundary 2 is connected to the local model enclosed by Boundary 2. The stiffness matrix is reduced by eliminating internal nodes of the local region through the Static Condensation (Guyan's Reduction) method [2]. The displacement field on the boundary is calculated from the reduced stiffness matrix. Then, that field is imposed on the local model with a fine mesh with interpolation. The most important advantage is that global and local regions are sensitive to each other (Two-way coupling).

The sub-modelling approach involves constructing a simplified global model and a detailed local model (i.e., sub-model) of the critical region. In sub-modelling, the whole area enclosed by Boundary 1 is analysed with a coarser mesh. The displacement field on Boundary 2 is then extracted. That field is imposed on the local model with finer mesh. As global and local meshes are different on Boundary 2 in general, the calculated displacement field should be interpolated. The displacement field obtained from the global model is applied to the boundary of the local model, and detailed analyses are performed in the local model [1]. This way, detailed damage analyses are carried out in the smaller local model instead of running the entire model, leading to computational time savings. Although the method is straightforward, the global model field is frozen and is not sensitive to the state of the local structure. Therefore, sub-modelling is a one-way global-local coupling method. This method is preferred in progressive failure analysis [11-16] and micro-meso-macro scale modelling applications [11,17,18].

The method requires a sufficiently large local model so that boundaries should be sufficiently away from the region of interest according to St.Venant's principle [3]. Otherwise, the displacement field obtained from the intact global model is invalid, as this field close to the damage region is inconsistent with the intact response, which violates the global-local boundary equilibrium.

To eliminate the violation of boundary equilibrium, boundary residuals are applied to the global model iteratively in the studies of Whitcomb and Woo [19-21] and Gossellet et al.[10]. Application of boundary residual makes the global-local method two-way coupled as boundary residual on the global model is dependent on the solution of the local model. However, this method leads to long computation times and convergence issues in damage analyses, creating high stiffness changes. Therefore, in addition to the boundary residuals, the global model must be updated according to the damage condition in the local model.

When the global model is updated, the analyses in the local model are refreshed, and then the global model is updated again. Global-local analyses are iteratively conducted until the specified criteria are met.

Submodelling is compatible with static and dynamic steps. On the other hand, the substructure is only compatible with the static perturbation step. As the substructure method is more complicated and only compatible with perturbation steps, few studies are available in the literature as shown in Table 2-3. Moreover, neither technique is compatible with the direct cyclic fatigue step. None of the studies shown in Table 2-3 covers fatigue analyses.

Using the S-N approach, Giglio [131] performed fatigue analyses by postprocessing static global/local FEA. Similarly, Liu et al. [130] performed fatigue analyses postprocessing static and transient FEA with plasticity. In both studies, there is no progressive failure analysis.

Table 2-3 Global Local Methods Used in the Literature

<b>Global Structure – Local Region</b>	<b>Submodelling</b>	<b>Substructure</b>	<b>Two-Way Submodelling</b>
Bridge – Bridge Joint	[130]		
Helicopter Rear Fuselage - Connector	[131]		
Specimen – Specimen Section	[132]	[3] [133] [134]	
Laminate - RVE	[11] [15] [17]		[19]
Wind Turbine Blade – Local Region	[16]		
Stiffened Panel – Critical Section	[13]		[1] [125]
Sphere/Tube – Local Contact Wear		[135]	
Laminate – Ply Submodel		[136]	
Pressure Vessel – Critical Section		[137]	
Wing – Leading Edge Section		[138]	

Therefore, global-local progressive fatigue analyses are lacking in the literature, which will be studied in this thesis. The study provides an interlaminar part of the global/local fatigue method.

In the literature, the local model is generally connected to the global model with a displacement condition (i.e., a sub-modelling method), as previously described. On the other hand, different approaches are used to connect the global model to the local model (Updating the global model).

The literature provides several different Global-Local CZM (Cohesive Zone Model) approaches.

In the first approach [1], undamaged cohesive elements are added to the global model, and their material stiffness values are updated physically based on the damage condition obtained from the local analysis. The procedure is applied to the T-Stiffener model and summarised in Figure 2-6.

In the second approach [22], spring connector elements with specific stiffness are added between the damage surfaces of the global model, and the connector stiffness values are updated based on the result obtained from the local model, summarised in Figure 2-7. This study applies the method to the T-Stiffener model and covers a Double Cantilever Beam study to verify their method [22].

In the third approach, the global model with a coarser mesh is directly solved with cohesive elements. Then, the sub-modeling method solves the local region with finer mesh in detail [125]. These studies cover DCB, 3-Point Bending, and Single-Lap Shear (SLS) modelling applications. The DCB application is shown in Figure 2-8.

This study proposes a progressive interlaminar fatigue damage analysis approach with two-way global-local coupling. This approach is more straightforward to apply and does not require interface elements in the global model, which will be further explained in the following sections.

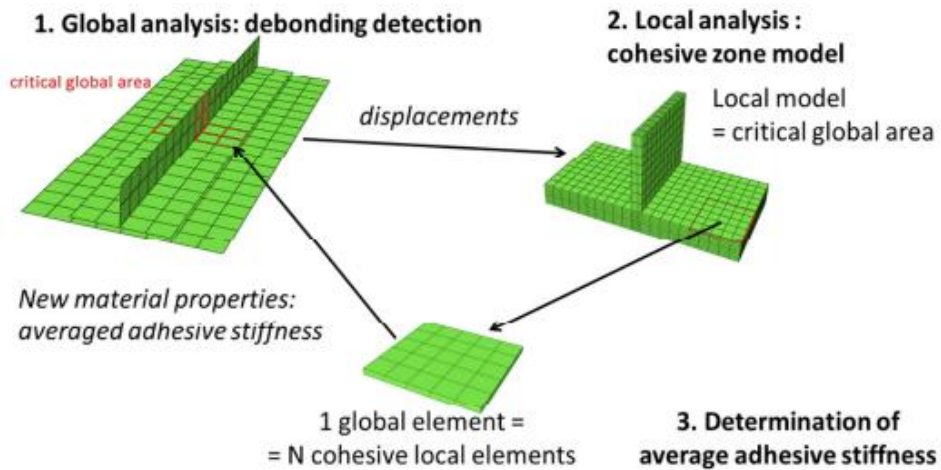


Figure 2-6. Global-Local Coupling by Averaging Stiffness Values of Global Cohesive Elements [1]

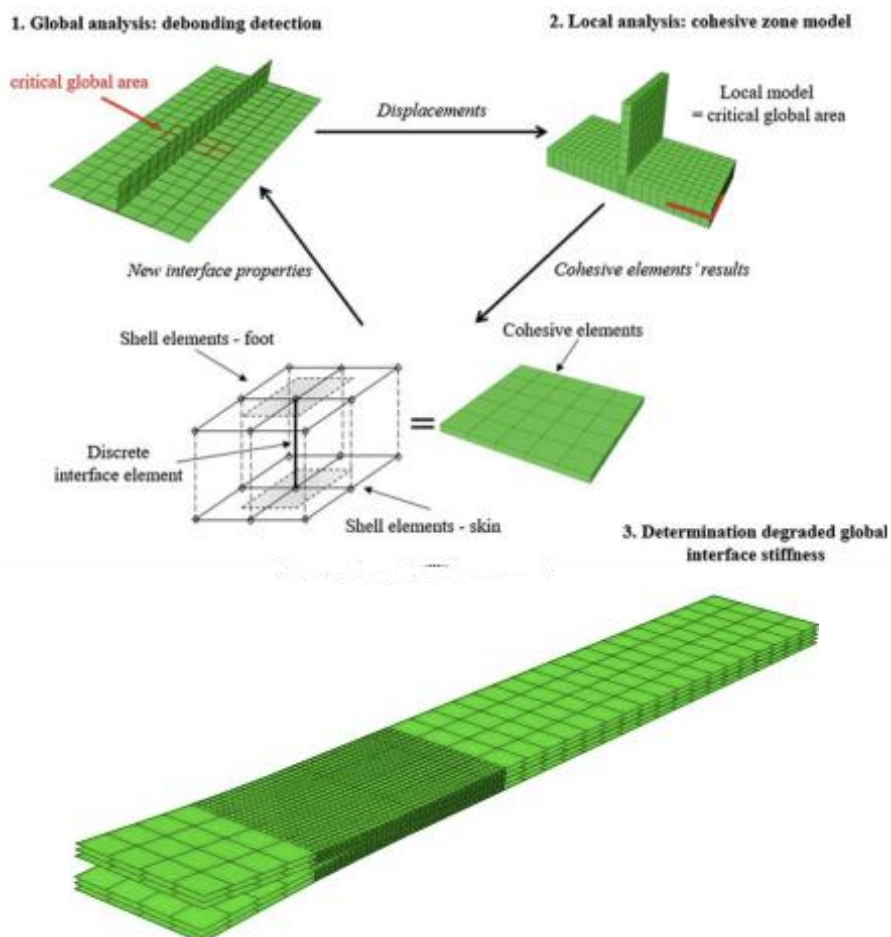


Figure 2-7. Global-Local Coupling by Mapping Local Cohesive Stiffness Values to the Global Connector Elements and Global-Local DCB Model [22]



Figure 2-8. Global-Local Coupling by Submodelling approach with Global Model with Cohesive Elements with Coarser Mesh on a DCB model [125]



## CHAPTER 3

### STATIC ANALYSES BY TWO-WAY GLOBAL-LOCAL COUPLING METHOD

#### 3.1 Introduction

##### Cohesive Zone Model

The methodology covers the detailed formulation of cohesive elements modelling interlaminar failure. Built-in constitutive response with damage mechanics of cohesive elements allows static analyses in Finite Element software such as Abaqus [126].

The amount of damage on cohesive elements is expressed with the damage parameter ( $\mathcal{D}$ ) named "SDEG" in the Abaqus program [126], which is necessary to implement the two-way global-local coupling method explained in Section 2.3.

Figure 3-1 illustrates the material response of a cohesive element. The stress-separation curve represents the response of the cohesive material. There are two different linear regions on this curve. In the region indicated by the line "OA," the cohesive element exhibits linear elastic behaviour in the intact region. If the separation amount at point "A" is exceeded, the cohesive element exhibits softening behaviour represented by the line "AB." When the separation amount at point "B" is exceeded, the cohesive element incurs complete damage and cannot carry the load.

To explain the damage parameter  $\mathcal{D}$  In Figure 3-1, a reference point representing the instantaneous stress-separation condition of the cohesive element is taken ("Point D"). The instantaneous damage parameter can be considered a ratio of reduction of chord stiffness, as schematically shown in Figure 3-1.

In the elastic region, i.e., on the line "OA," the damage parameter equals 0. In the softening region, i.e., on the line "AB," the damage parameter will take a value

between 0 and 1. If the separation amount exceeds the separation at point "B," the parameter equals 1, and the cohesive element cannot carry the load.

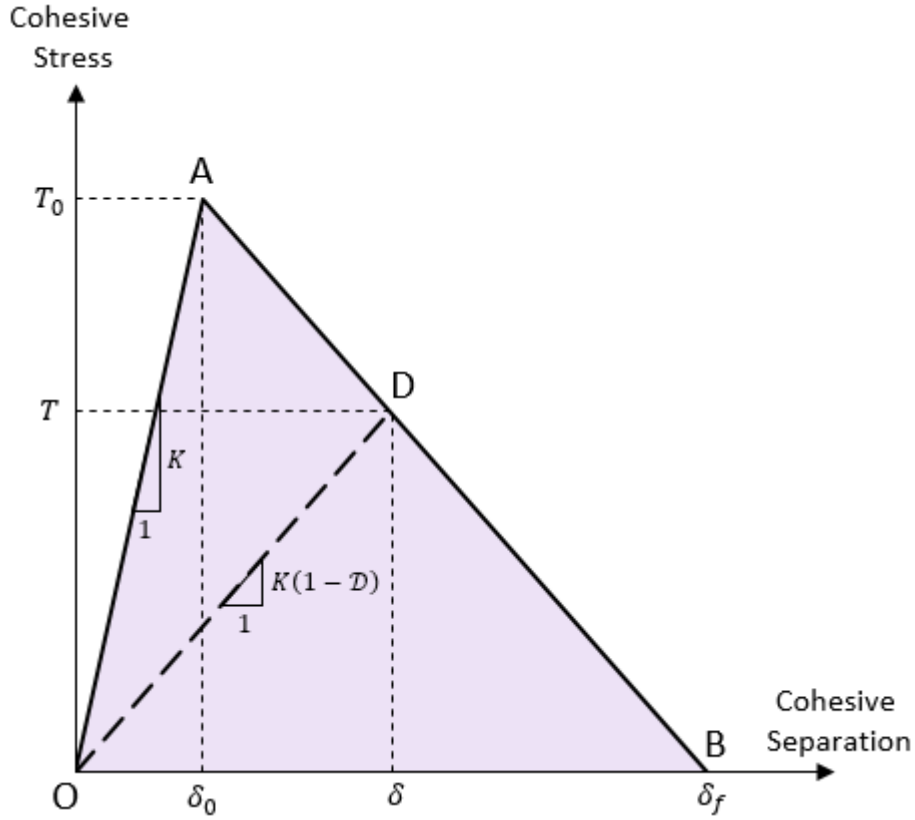


Figure 3-1 Cohesive Element Traction-Separation Behaviour

Cohesive damage is introduced in this method according to the Quadratic Stress Criterion:

$$\left(\frac{\langle T_3 \rangle}{T_{3,0}}\right)^2 + \left(\frac{T_1}{T_{1,0}}\right)^2 + \left(\frac{T_2}{T_{2,0}}\right)^2 = 1 \quad (3-1)$$

where

$$\langle T_3 \rangle = \frac{T_3 + |T_3|}{2} \quad (3-2)$$

The damage parameter drives the evolution of the damage  $\mathcal{D}$  which is defined according to Figure 3-1. It is the ratio of elastic stiffness loss.

$$\mathcal{D} = 1 - \frac{T}{K\delta} \quad (3-3)$$

Traction-separation curve is analytically described by Eq.(3-4).

$$T = K(1 - \mathcal{D})\delta, \quad \delta_0 < \delta \leq \delta_f \quad (3-4)$$

In terms of  $\delta, \delta_0, \delta_f$

$$T = K\delta, \quad 0 \leq \delta \leq \delta_0 \quad (3-5)$$

$$T = K\delta_0 \frac{\delta_f - \delta}{\delta_f - \delta_0}, \quad \delta_0 < \delta \leq \delta_f \quad (3-6)$$

$$T = 0, \quad \delta > \delta_f \quad (3-7)$$

Equating Eq.(3-5)-(3-7) to Eq. (3-4) gives damage parameter expressions in terms of separation parameters.

$$\mathcal{D} = 0, \quad 0 \leq \delta \leq \delta_0 \quad (3-8)$$

$$\mathcal{D} = \frac{\delta_f(\delta - \delta_0)}{\delta(\delta_f - \delta_0)}, \quad \delta_0 < \delta \leq \delta_f \quad (3-9)$$

$$\mathcal{D} = 1, \quad \delta > \delta_f \quad (3-10)$$

The area under Figure 3-1 is defined as the critical SERR, the material interface parameter, as shown by Eq.(3-11).

$$G_C = \int_0^{\delta_f} T(\delta)d\delta = \frac{T_0\delta_f}{2} \quad (3-11)$$

This parameter is mode-dependent, modelled by the Benzeggagh-Kenane [30] expression in this study.

$$G_C = G_{IC} + (G_{IIC} - G_{IC}) \left( \frac{G_{II} + G_{III}}{G_T} \right)^\eta \quad (3-12)$$

For the Benzeggagh-Kenane formulation, the following relations hold:

$$G_T = G_I + G_{II} + G_{III} \quad (3-13)$$

$$G_{IIC} = G_{III} \quad (3-14)$$

## The Global-Local Method

The current Global-Local technique assesses the impact of localised changes within a computational model (such as interlaminar damage) without requiring extensive modifications. Specifically, the goal is to use an aerospace structure model with existing commercial software to simulate the effects of local changes due to interlaminar failure by repeatedly running simulations that only introduce traction loads into the global model. Additionally, these modifications can be computed using any software of choice, including specialised research codes.

For the implementation of the method, the following models are created:

- Global Model: This model encompasses the entire structure. The mesh is coarse and does not contain cohesive elements modelling damage. There are tie constraints on the damage surface. Depending on the damage state of the local model, tie constraints are removed and replaced by nodal forces calculated by internal nodal reactions of cohesive elements in the local model.
- Local Model: This model only constructs the model around the damage zone. The mesh is fine and includes cohesive elements modelling the interlaminar damage.
- Auxiliary Model: This model also constructs the model around the damage zone like the local model. However, the mesh structure is the same as the global model and does not include cohesive elements modelling the damage. Instead, there are tie constraints on the damage surface. This model is a local region cut from the global model without changing property.

In this study, the method described by Gossellet et al. [10] is utilised for boundary residual application due to different mesh sizing. The method of Gossellet et al. [10] requires an auxiliary model for the calculation of boundary residual to satisfy global-local boundary equilibrium.

The boundary conditions connecting the global, local, and auxiliary models are depicted in Figure 3-2. Initially, the boundaries of the auxiliary and local models are assigned with sub-modelling displacement boundary conditions. When this boundary condition is added, the displacement distribution calculated from the global model is applied to the boundaries of the local and auxiliary models, thus connecting the local and auxiliary models to the global model. This condition is illustrated with red arrows in Figure 3-2.

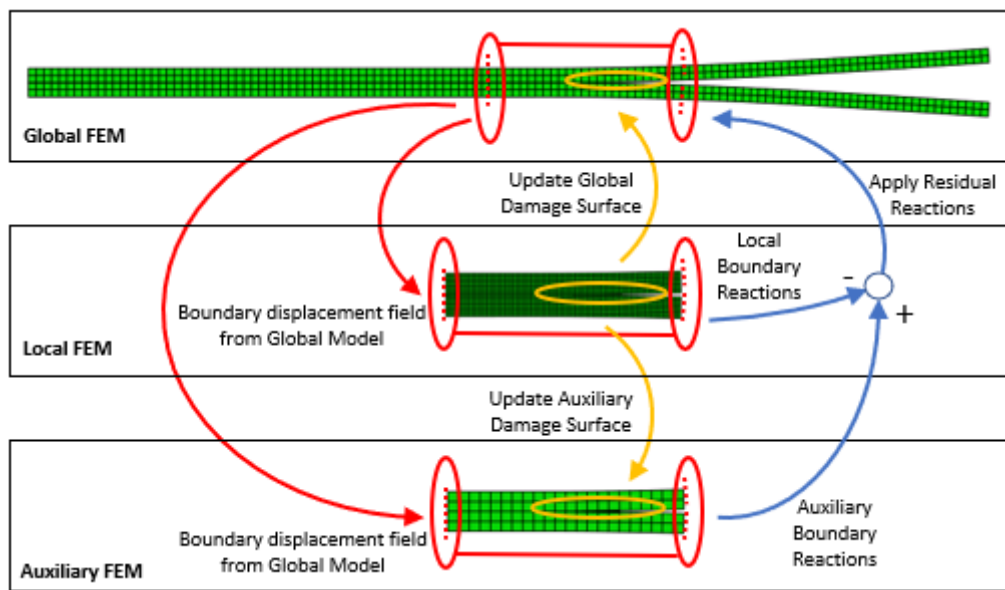


Figure 3-2 Two-Way Global-Local Coupling with the Damage Mapping Algorithm  
 The second boundary condition is applied to the delamination surface in the global model. For simplicity, a detailed application of the procedure is given in Figure 3-3 for the upper half of a DCB model.

This boundary condition is dependent on the damage parameter  $\mathcal{D}$  named "SDEG," obtained from the cohesive elements in the local model, as detailed in this section previously. If this parameter is 0, no damage has occurred in that region, and the tie constraint at the equivalent nodal points in the global model is preserved. When this parameter exceeds 0, damage initiation occurs in that region. In this case, the tie constraint at the equivalent nodal points in the global model is removed. However, when this parameter is less than 1, there is still some weak bonding in that region.

Therefore, the forces at these nodal points are calculated from cohesive elements and applied to the equivalent nodal points in the global model with opposite signs. Since the global and local mesh structures are different, cohesive nodal points should be distributed to global nodal points with consistent load vector formulation. When the damage parameter is 1, the corresponding nodes are disconnected, resulting in no nodal force. This condition is illustrated with yellow arrows in Figure 3-2.

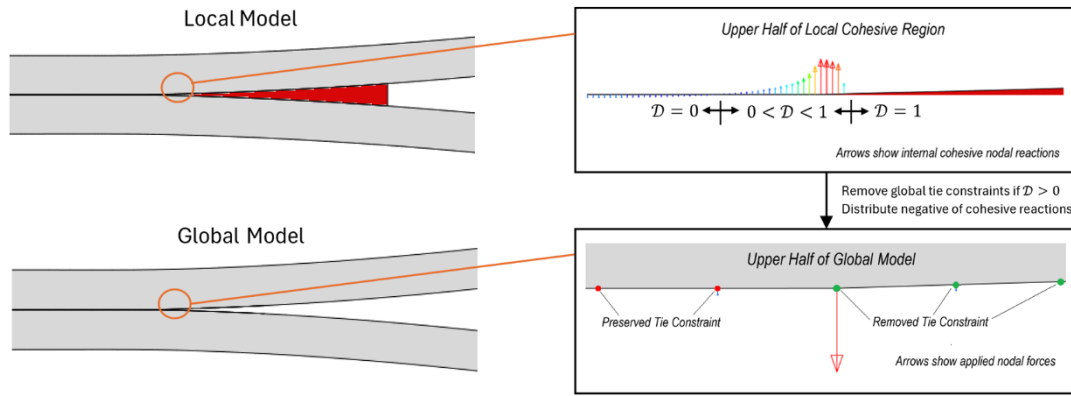


Figure 3-3. Application of Damage Mapping

In the third condition, residual loads are applied to the global model's boundary. These loads arise due to the different mesh structures of the global and local models. This application is illustrated with blue arrows in Figure 3-2. The residuals in the current iteration are applied on top of those from the previous iteration (Residual force application accumulates in iterations), as expressed in Eq.(3-15).

$$R_{i,j}^{k,Global} = R_{i,j}^{k-1,Global} + \Delta R_{i,j}^k \quad (3-15)$$

The subscript “i” represents the node number, and “j” represents the component (x,y or z). The residual loads are calculated by subtracting the local model's boundary reactions from the auxiliary model's boundary reactions, as expressed in Eq.(3-16).

$$\Delta R_{i,j}^k = R_{i,j}^{k,Auxiliary} - R_{i,j}^{k,Local} \quad (3-16)$$

Since the global and local mesh structures differ, local model boundary reactions should be distributed to corresponding global nodal points. Before calculating the applied residual loads in the current iteration, as shown in Eq.(3-16), the local model boundary reactions are mapped to the global boundary nodes with consistent load

vector formulation. Figure 3-4 illustrates the residual application's detailed algorithm.

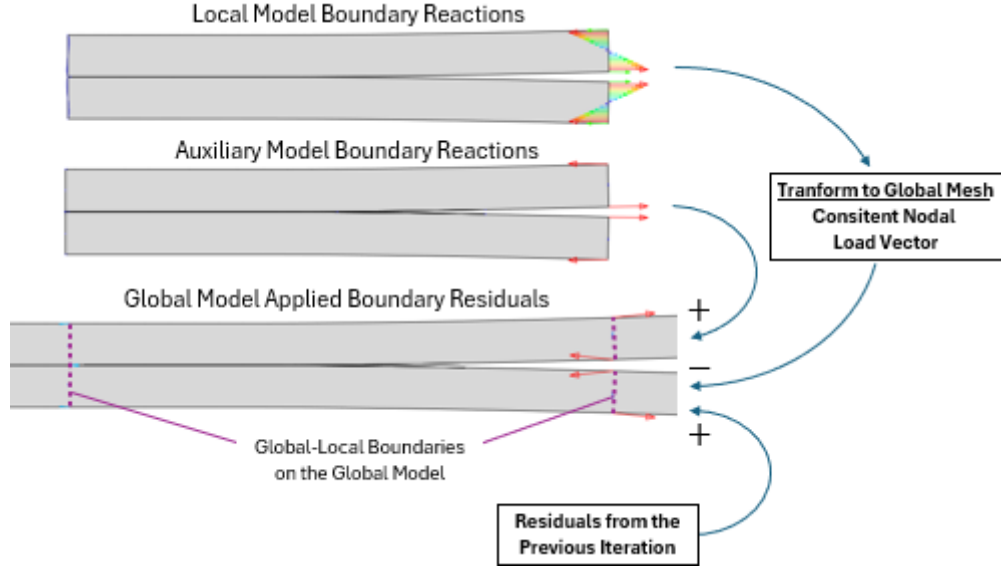


Figure 3-4. Application of Boundary Residuals

As previously mentioned, the meshing of global/auxiliary and local models differs. In general, the local region is finely meshed. Internal cohesive nodal reaction distribution on global and auxiliary damage surfaces requires consistent nodal load formulation. Moreover, for the calculation of boundary residuals, the local boundary reactions should be consistent with the global and auxiliary mesh structure for the boundary residual calculations. Figure 3-5 shows the distribution of a local nodal force on the closest global/auxiliary nodes. For simplicity, 2D meshing is shown with vertical force components.

A single local nodal force is distributed on the global or auxiliary model with the help of the Dirac Delta function, as shown by Eq.(3-17).

$$F_{i,j} = \int_{1 \rightarrow 2} \mathcal{N}_i(x) F_{a,j} \delta(x - x_a) dx = \mathcal{N}_i(x_a) F_{a,j} \quad (3-17)$$

where  $\mathcal{N}$  is the shape function of the global/auxiliary element, “i” is node number 1 or 2, and j is x, y or z.

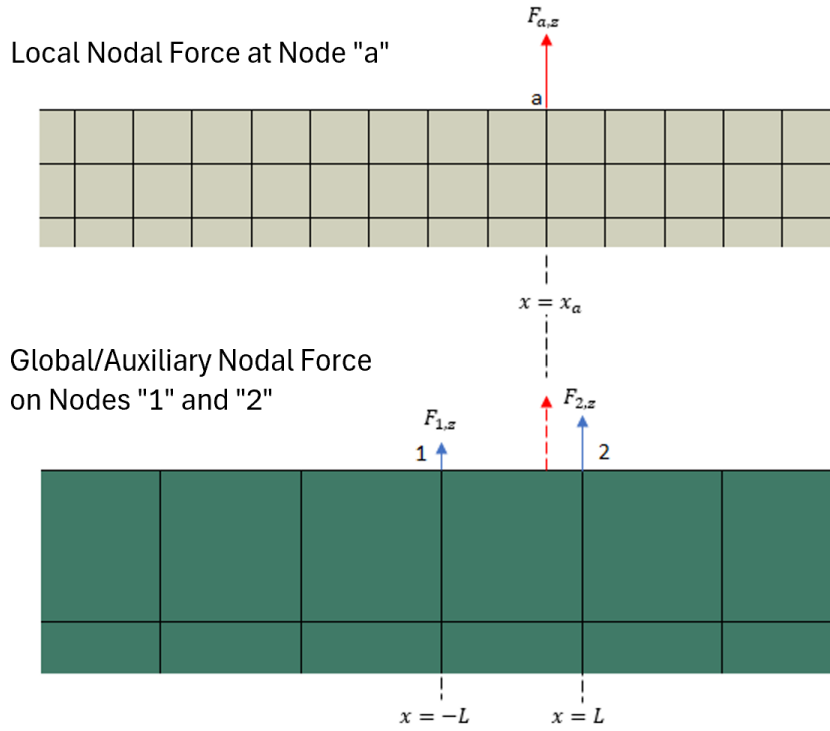


Figure 3-5. Distribution of Local Nodal Force on Corresponding Global/Auxiliary Nodes

For the problem shown in Figure 3-5, assuming that the global/auxiliary element has linear shape functions given by Eq.(3-18a) and (3-18b), nodal forces are calculated in Eq.(3-19a) and (3-19b),

$$\mathcal{N}_1(x) = \frac{1}{2} \left(1 - \frac{x}{L}\right) \quad (3-18a)$$

$$\mathcal{N}_2(x) = \frac{1}{2} \left(1 + \frac{x}{L}\right) \quad (3-18b)$$

$$F_{1,z} = \frac{L - x_a}{2L} F_{a,z} \quad (3-19a)$$

$$F_{2,z} = \frac{L + x_a}{2L} F_{a,z} \quad (3-19b)$$

Similarly, for 3D meshing, the load distribution on 2D surfaces is formulated in Eq.(3-20).

$$F_{i,j} = \int_{A_e} \mathcal{N}_i(x, y) F_{a,j} \delta(x - x_a) \delta(y - y_a) dx dy = \mathcal{N}_i(x_a, y_a) F_{a,j} \quad (3-20)$$

Eq.(3-17) and (3-20) do not require numerical integration but only require evaluation of shape functions at nodal points. For isoparametric formulation, the substitutions shown in Eq.(3-21) and Eq.(3-22) [129] are applied to Eq.(3-20).

$$dxdy = \|J\|d\xi d\eta \quad (3-21)$$

$$\delta(x - x_a)\delta(y - y_a) = \frac{1}{\|J\|} \delta(\xi - \xi_a)\delta(\eta - \eta_a) \quad (3-22)$$

where  $\|J\|$  is Jacobian between  $(x,y)$  and  $(\xi, \eta)$  coordinates. Eq.(3-21) and (3-22) result in the cancellation of Jacobian in Eq.(3-20), and therefore, the isoparametric formulation does not contain the Jacobian term, which simplifies the integral as shown by Eq.(3-23). Therefore, applying local forces with the help of the Dirac Delta function simplifies the integration of consistent nodal load vector calculations, and the evaluation of shape function at nodal points is sufficient. In applying the current method, deformed nodal coordinates are considered in calculations.

$$F_{i,j} = \int_{-1}^1 \int_{-1}^1 \mathcal{N}_i(\xi, \eta) F_{a,j} \delta(\xi - \xi_a) \delta(\eta - \eta_a) d\xi d\eta = \mathcal{N}_i(\xi_a, \eta_a) F_{a,j} \quad (3-23)$$

Figure 3-6 summarises one iteration loop. This algorithm has been modelled with the MATLAB code created within the scope of the study. The complete algorithm involves submodelling boundary conditions, cohesive damage mapping and application of boundary residuals.

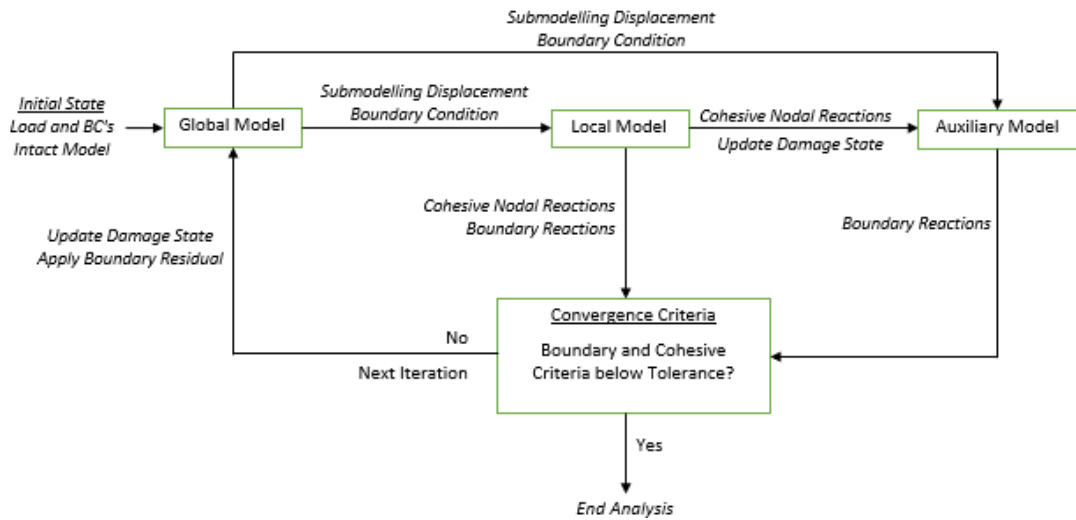


Figure 3-6. One Iteration Loop of Two-Way Global-Local Coupling Methodology

The method can also be summarised as follows:

1. Create a local model with cohesive elements.
2. Create a global model with tie constraints representing possible failure surfaces of local region with cohesive elements.
3. Create an auxiliary model with tie constraints. The auxiliary model is the local region identical to the global one.
4. Run the global model (with all possible tie constraints (intact) in the first iteration).
5. By submodeling driven by the global model, apply the boundary displacement field on the local model.
6. Extract local node numbers with softening ( $SDEG > 0$ ) and corresponding nodal reactions.
7. Calculate local boundary reactions.
8. Map local node numbers with  $SDEG > 0$  to auxiliary node numbers.
9. Remove tie constraints from these nodes in the auxiliary model and apply nodal reactions (from step 6) to them.
10. Calculate auxiliary boundary reactions
11. Check termination criteria to be satisfied simultaneously
  - a. Relative error of cohesive nodal residual below tolerance
  - b. Normalized boundary residual (Difference of Local and Auxiliary boundary reactions).
12. If the criteria are met. Accept the solution. If not, map local node numbers with  $SDEG > 0$  to global node numbers.
13. Remove tie constraints from these nodes in the global model and apply nodal reactions (from step 6) to them.
14. Apply additional boundary residual on the global model. Keep residuals from the previous iteration.
15. Run the updated global analysis and go to step 4.

The boundary conditions of the local model are dependent on the global model, and the damage surfaces of the global model are dependent on the local model. Since the two models are interdependent, iterative calculations are required to achieve the correct solution. For iterative computation to be terminated close to the correct solution, two criteria are selected for termination:

- Boundary Residual Criterion for Global-Local Boundary Equilibrium: Absolute value of maximum boundary residual among all boundary nodes divided by average boundary internal nodal reaction of the global model at the current iteration
- Cohesive Relative Nodal Force Error for Convergence of Damage State: Absolute value of maximum cohesive internal nodal reaction change to the previous iteration among all cohesive nodes divided by average cohesive internal nodal reaction at the current iteration

Formulations of these criteria are explicitly shown in Table 3-1 with the following notation:

- $i$  : Node number
- $j$  :  $x, y, z$  component
- $k$  : Iteration number
- $R$  : Boundary Residual applied on the Global Model
- $Q$  : Cohesive Nodal Reactions from the Local Model

For termination, a tolerance (TOL) value of 1% is selected for both criteria.

The methodology is applied to the Analytical DCB Model to clarify this method. The DCB model is schematically shown in Figure 3-7. The loading is displacement-controlled. Therefore, arm separation is the input, and arm reaction and crack length are the outputs. The global model is the beam itself, and the local model is the zone between  $x=l$  and  $x=s$ . Initially, the global model crack length is equal to  $a_0$ . The crack length is updated using the local model solution.

Table 3-1. Calculation of Boundary and Cohesive Criteria

Boundary Criterion	Cohesive Criterion
$\eta_{BC} < TOL$	$\eta_{CC} < TOL$
$\eta_{BC} = \frac{ \Delta R _{max}}{ R _{average}}$	$\eta_{CC} = \frac{ \Delta Q _{max}}{ Q _{average}}$
$ \Delta R _{max} = \max_i  \Delta R_i^k $	$ \Delta Q _{max} = \max_i  \Delta Q_i^k $
$ R _{average} = \frac{1}{N} \sum_{i=1}^N  R_i^k $	$ Q _{average} = \frac{1}{N} \sum_{i=1}^N  Q_i^k $
$ \Delta R_i^k  = \sqrt{(\Delta R_{i,x}^k)^2 + (\Delta R_{i,y}^k)^2 + (\Delta R_{i,z}^k)^2}$	$ \Delta Q_i^k  = \sqrt{(\Delta Q_{i,x}^k)^2 + (\Delta Q_{i,y}^k)^2 + (\Delta Q_{i,z}^k)^2}$
$ R_i^k  = \sqrt{(R_{i,x}^k)^2 + (R_{i,y}^k)^2 + (R_{i,z}^k)^2}$	$ Q_i^k  = \sqrt{(Q_{i,x}^k)^2 + (Q_{i,y}^k)^2 + (Q_{i,z}^k)^2}$
$\Delta R_{i,j}^k = R_{i,j}^{k,Auxiliary} - R_{i,j}^{k,Local}$	$\Delta Q_{i,j}^k = Q_{i,j}^k - Q_{i,j}^{k-1}$

The local model boundary displacement and rotations are calculated from the global model deflection field. Displacement and rotation boundary conditions are applied to the local model boundary at  $x=l$ . Note that at  $x=s$ , displacement and rotation are always zero.

After applying sub-modelling boundary conditions, the crack length is updated using the local model's SERR solution. The new crack length is imposed on the global model. Then, the boundary conditions of the local model are determined again for the next iteration. This procedure is repeated until convergence is achieved. Detailed formulation is given in Appendix B. Numerical parameters are listed in Table 3-2.

For displacement-controlled input, exact solutions of the arm reaction and the propagated crack length are given in Eq. (3.24) and (3.25). According to the numerical parameters shown in Table 3-2, the exact values of the arm reaction and crack length are listed in Table 3-3.

$$P = \frac{3D\delta}{2a^3} \quad (3-24)$$

$$a = \sqrt[4]{\frac{9D\delta^2}{4G_{IC}}} \quad (3-25)$$

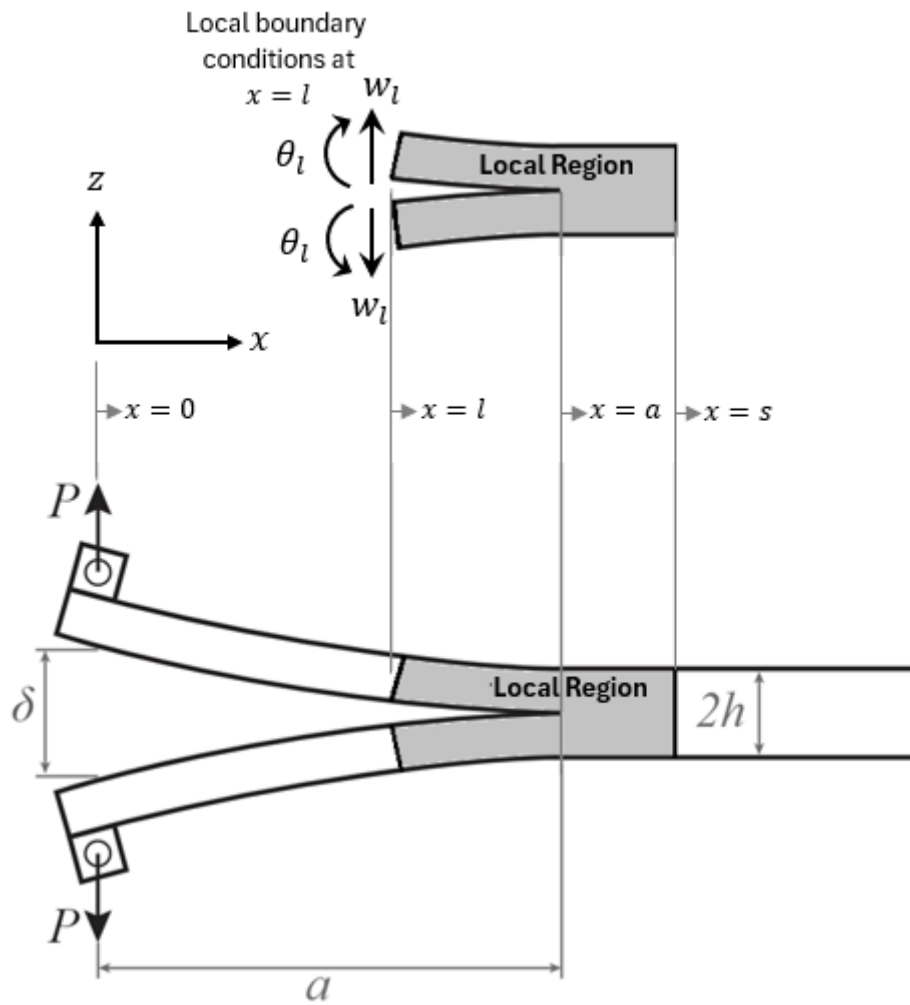


Figure 3-7. Analytical DCB Model

Table 3-2. Numerical Values of the DCB Model Parameters

Parameter	Definition	Value
$D$	Flexural Rigidity ( $Eh^3/12$ )	40000 N.mm
$G_{IC}$	Critical SERR	0.25 N/mm
$\delta$	Arm Separation	8 mm
$a_0$	Initial Crack Length	50 mm
$l$	Global-Local Boundary x-Coordinate	30 mm

Table 3-3. Exact Solutions of the Arm Reaction and Crack Length

Parameter	Definition	Value
$P$	Arm Reaction	1.38 N/mm
$a$	Propagated Crack Length	66.40 mm

Application of the algorithm:

1. Solve the global model with input separation  $\delta$  and delamination length  $a$ . For the first calculation, start with the initial crack length ( $a = a_0$ ). Calculate  $w_l, \theta_l$  with Eq. (3-26) and (3-27). Also calculate the arm reaction with Eq.(3-24), which is valid for the algorithm.

$$w_l = \frac{\delta}{4} \left( 2 + \frac{l}{a} \right) \left( 1 - \frac{l}{a} \right)^2 \quad (3-26)$$

$$\theta_l = \frac{3\delta}{4a} \left( 1 - \frac{l^2}{a^2} \right) \quad (3-27)$$

2. Solve local model with  $w_l, \theta_l$  boundary conditions. Calculate SERR with Eq.(3-28).

$$G_I = D \left[ \frac{6w_l}{(a-l)^2} - \frac{2\theta_l}{(a-l)} \right]^2 \quad (3-28)$$

Check  $G_I \geq G_{IC}$  then determine new crack length with Eq.(3-29). Otherwise, terminate the analysis.

$$a = l + \frac{-D\theta_l + \sqrt{D^2\theta_l^2 + 6w_l\sqrt{D^3G_{IC}}}}{\sqrt{DG_{IC}}} \quad (3-29)$$

3. If convergence is achieved, terminate the analysis. Otherwise, Return to Step 1 with the new crack length given in Eq.(3-29).

This algorithm is fixed point iteration to solve equations (3-26), (3-27), and (3-29) with an initial guess of  $a = a_0$ . The crack length results are shown in Figure 3-8, and

the arm reaction results are shown in Figure 3-9. The results show that crack length and arm reaction values are converged to the exact results.

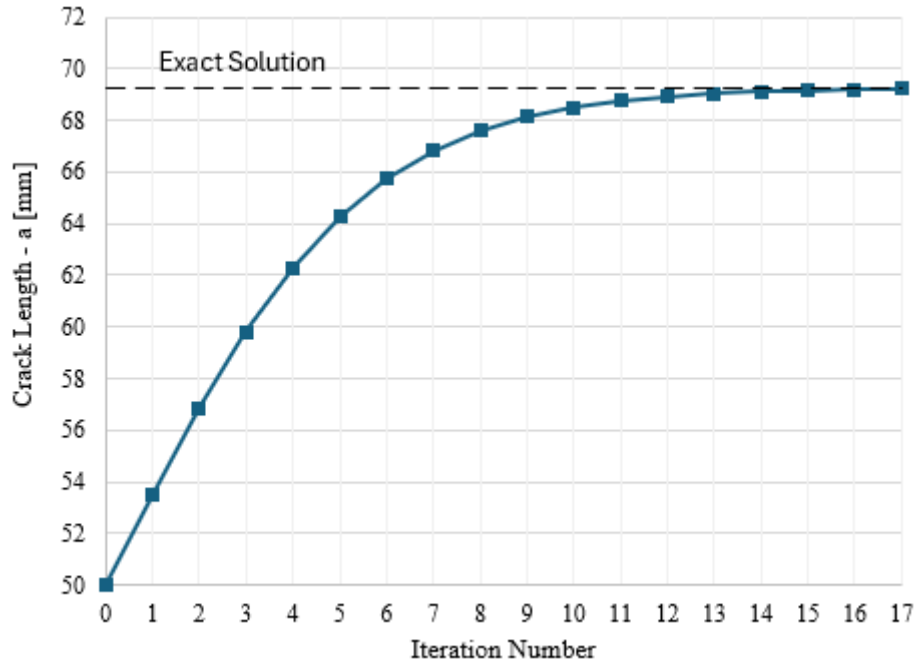


Figure 3-8. Crack Length Result of Analytical DCB Model

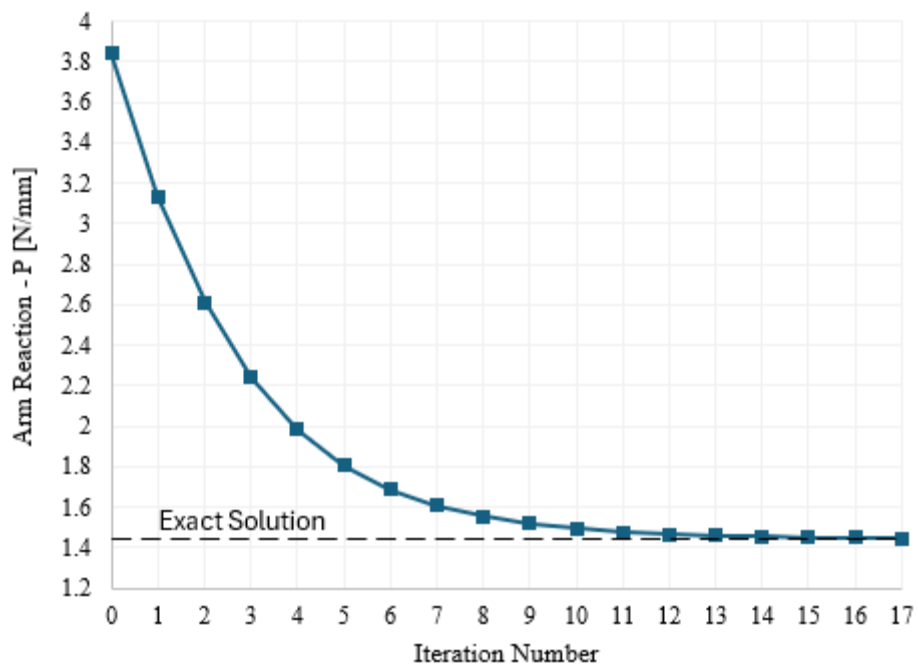


Figure 3-9. Arm Reaction Result of Analytical DCB Model

## **3.2 Verification of the Method with Double Cantilever Beam Analyses**

This section covers the verification of the method, damage mapping algorithm with application of boundary residuals. The DCB response is well-known, and closed-form solutions are available. The modelling of the DCB and its analyses are supported by experiments.

Regular analyses are also performed to verify the current method. Regular analyses are defined as finite element analyses (FEA) that are directly applied to the complete model in detail without applying the global-local method. Consequently, the results of the current global-local method are compared with analytical and regular analysis solutions in terms of accuracy to verify the method.

### **3.2.1 Description of the Global-Local Finite Element Model**

Figure 3-10 shows the Double Cantilever Beam (DCB) model. It is the simplest model for observing the interlaminar response and a standard experimental specimen for determining interlaminar fracture toughness. Closed-form solutions are available for comparison because of the simplicity of the model. Moreover, it suits the two-way global-local coupling analysis as the global stiffness is highly sensitive to local crack length.

Modelling was performed using the Abaqus CAE [126] interface. C3D8I brick elements with incompatible modes, with a side length of 1 mm for global and auxiliary models and 0.1 mm for local models, are selected. These elements are assigned orthotropic material properties of CFRP oriented at 0 degrees. Beams in the models are divided into two parts, connected by tie constraints in the global and auxiliary models and cohesive (COH3D8) elements in the local model.

In the global model, the left end of the beam is fixed, while the ends of the beam arms at the right are vertically opened relative to each other by an amount of  $\delta$ .

Nonlinear geometric effects (large displacements - large strains) are included in the analyses. Maximum arm separation of  $\delta=6.5$  mm is applied to the model.

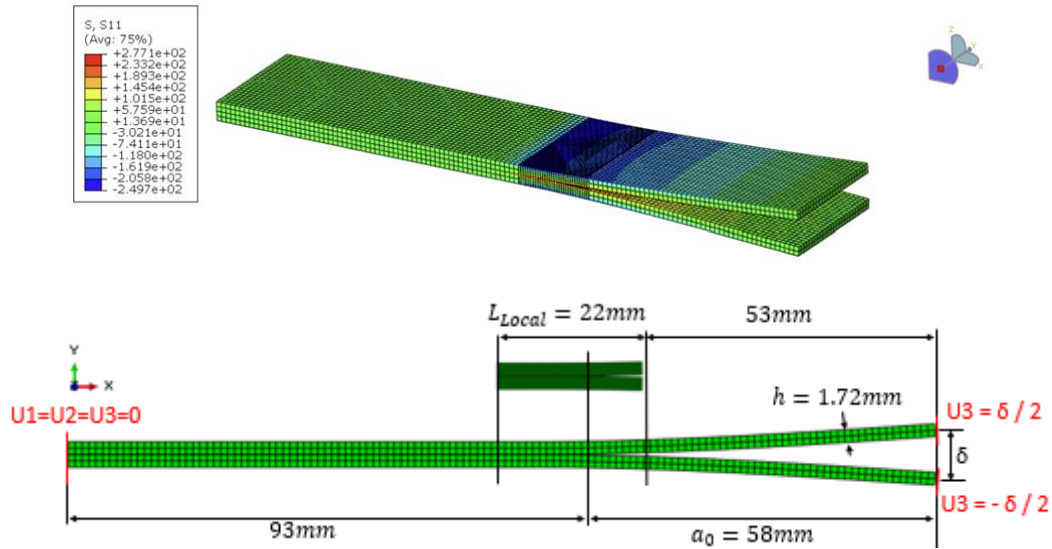


Figure 3-10. Double Cantilever Beam Global-Local 3-D Finite Element Model

### 3.2.2 Baseline Solutions Supported by Experiments

This study determined the Mode-I critical SERR (fracture toughness) values through standardised DCB tests for CFRP material. The parameters extracted from these experiments have been utilised in the material formulation of cohesive elements. The experiments were performed in the Turkish Aerospace facility.

A typical DCB specimen is shown in Figure 3-11. The specimen comprises CFRP material with a stacking sequence of  $[0_n//0_n]$  according to the coordinate system shown in Figure 3-11, the x-axis being the 0-degree direction and the y-axis being the 90-degree direction. The sign “//” indicates the location of the PTFE insert and crack plane. The specimens have a total length  $L$  of 150 mm, width  $b$  of 25 mm and each arm has a nominal thickness  $h$  of 1.72 mm. The piano hinges are bonded to the ends of each arm by adhesive for load and displacement application. Then, the hinges are held by the grips of the tension machine, which opens the arms by the desired amount.

Before the tests, pre-cracking was introduced since the current CFRP material does not suffer from fibre bridging severely. The initial crack length  $a_0$  is then marked from the piano hinge to the end of the pre-crack with the region of the PTFE insert, as shown in Figure 3-11.

Static tests are conducted to determine the critical SERR ( $G_c$ ), which is determined using the Modified Beam Theory (MBT) method according to ASTM D5528 [127]. Static tests are performed under displacement control. The samples are loaded at an opening rate of 2 mm/min until the total crack length reaches approximately 100 mm. Then, the specimens are unloaded at 10 mm/min. Calculation methods for critical SERR are provided in ASTM D5528 [127].

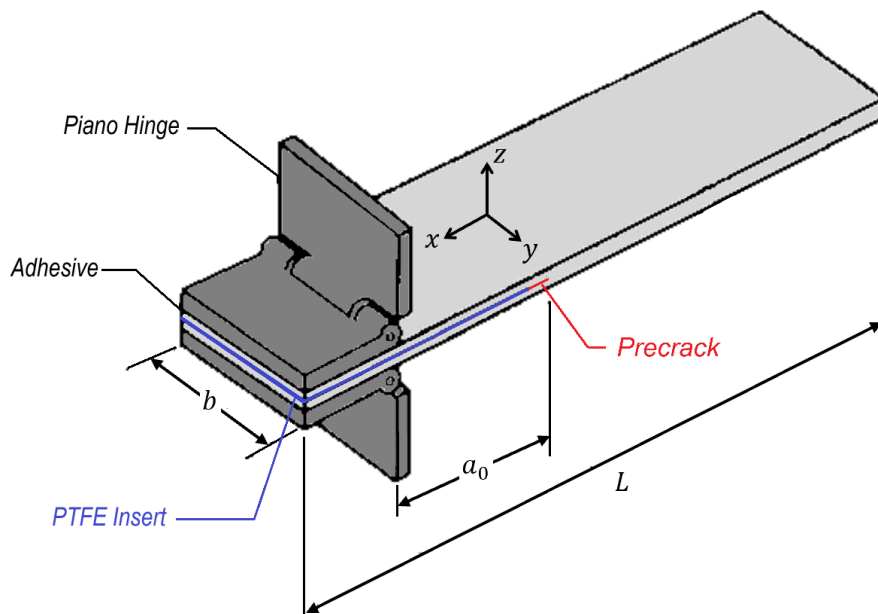


Figure 3-11. Double Cantilever Beam (DCB) Specimen

Regular finite element analysis has also been conducted to compare the accuracy and computation times of the global-local analyses. This model encompasses the entire structure. The damaged region of the structure is densely meshed, and the damage is modelled using cohesive elements. The parts of the model away from the damage are coarsely meshed, and the damage surfaces are connected with tie constraints. This model is an adaptation of the global-local model described in the previous

section to the regular method, and it is expected that the solutions of the global-local analyses are consistent with the solution of this model.

The DCB (Double Cantilever Beam) structure can also be solved analytically, and analytical solutions are provided as references for all solutions. Analytical formulation requires extraction of Critical SERR from the experiments.

In static analyses, the Modified Beam Theory (MBT) formulation is widely used in DCB tests, and relevant expressions are given in ASTM Standards [127,128] and the study of Harper and Hallett [110]. The closed-form solution of arm reaction as a function of arm opening is given in Eq. (3-30). Derivation of Eq.(3-30) is presented in Appendix A.

$$P = \begin{cases} \frac{3D\delta}{2(a_0 + \chi h)^3} & , \delta \leq \delta_{cr} \\ \sqrt[4]{\frac{4DG_{IC}^3}{9\delta^2}} & , \delta > \delta_{cr} \end{cases} \quad (3-30)$$

Eq.(3-30) involves critical arm separation  $\delta_{cr}$ , defined as the amount of separation where crack propagation starts. Its expression is given in Eq.(3-31)

$$\delta_{cr} = \frac{2}{3} \sqrt{\frac{G_{IC}}{D}} (a_0 + \chi h)^2 \quad (3-31)$$

where  $\chi h$  is the crack length correction, and its expression is given in the study of Harper and Hallett [110]. In the current example, crack length correction is calculated as 3.2 mm, close to the crack length correction calculated from the experiments according to ASTM D5528 [127]. Figure 3-12 shows the determination of Critical SERR based on MBT, as shown in Eq.(3-32).

$$G_{IC} = \frac{P_{cr}^2 (a_0 + \chi h)^2}{D} \quad (3-32)$$

where  $P_{cr}$  is the force where propagation starts, which is experimentally determined from ASTM D5528 [127]. This parameter corresponds to the arm reaction evaluated at critical separation  $\delta_{cr}$  from Eq.(3-32). Based on the worst specimen, SERR is 0.20

N/mm using Eq.(3-32) according to ASTM D5528 [127]. The analytical curve from Eq.(3-30) for the critical SERR of 0.2 N/mm is also given. The Regular FEA also verifies the expression with a mesh size of 0.1 mm.

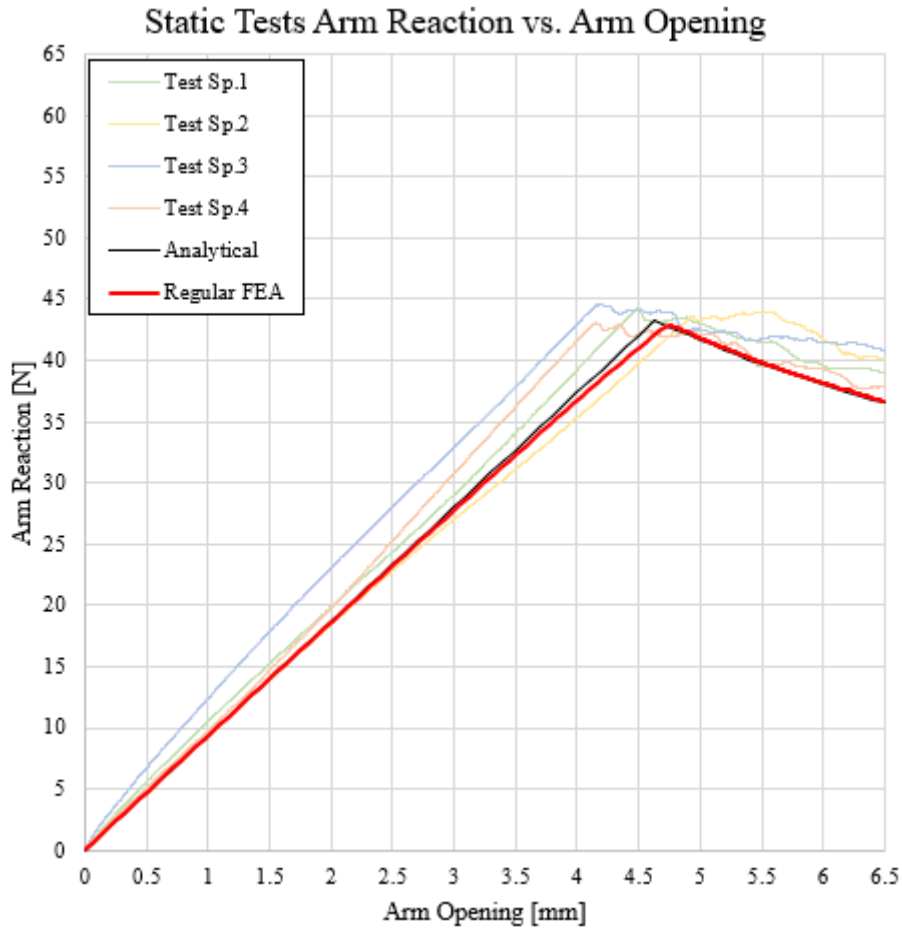


Figure 3-12. Selection of Critical SERR Based on MBT Formula

### 3.2.3 Mesh Independency Study

For the DCB model, four mesh sizes of 1 mm, 0.5 mm, 0.25 mm and 0.1 mm are selected. The maximum cohesive element length required to capture the damage onset is given in Eq.(3-33) [26,108]. For the values shown in Table 3-4, the maximum element length is calculated as 0.1 mm. Mesh convergence is not expected for larger cohesive elements, as shown in Figure 3-13.

$$l_{e,max} = \frac{9\pi E_3 G_{IC}}{32 N_e T_{n,0}^2} \quad (3-33)$$

Table 3-4. DCB Model Parameters for Mesh Size Determination

Parameter	Definition	Value
$E_3$	Out-of-Plane Young Modulus	10000 MPa
$G_{IC}$	Critical SERR in Mode I	0.2 N/mm
$T_{n,0}$	Interlaminar Tensile Strength	30 MPa
$N_e$	Number of elements per cohesive zone [26,108]	20
$l_{e,max}$	Maximum cohesive element size for convergence	0.1 mm

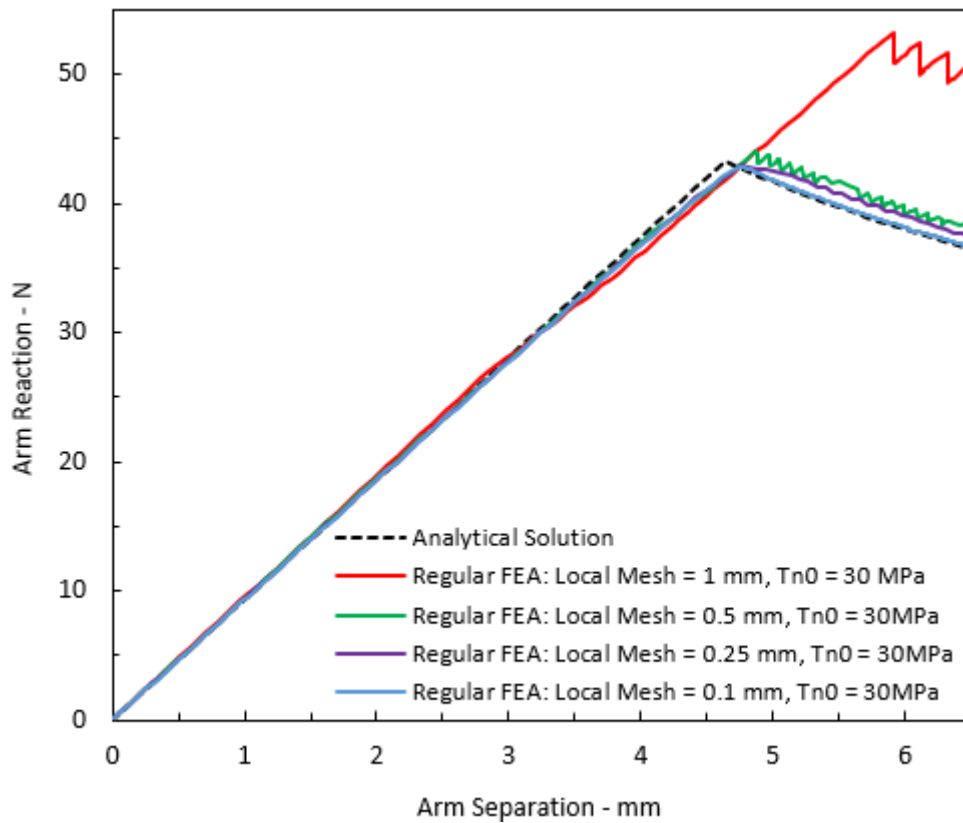


Figure 3-13. DCB Response for Different Mesh Sizes without Mesh Regularisation Assessed by Regular FEA (Mesh Size other than the local region is 1 mm)

However, mesh sizes below 0.1 mm are impractical due to the enormous computational expense, especially for larger aerospace structures. Instead, interfacial strength is artificially reduced to increase the maximum cohesive element length. It

is observed that interface strength has no significant effect on estimating delamination propagation, although the stress field around the delamination tip changes. Therefore, using Eq.(3-33), new interface strength can be modified for larger mesh sizes, as shown in Eq.(3-34).

$$T_{n,0,new} = T_{n,0} \sqrt{\frac{l_{e,max}}{l_e}}, \quad l_e > l_{e,max} \quad (3-34)$$

Eq.(3-34) applies mesh regularisation to interfacial strength. Mesh regularised results are shown in Figure 3-14. Although the response is oscillatory for the largest mesh size of 1 mm, the results are consistent with analytical formulation in the softening region. However, reduction of interface strength leads to early softening, which is more evident for larger mesh sizes.

Figure 3-14 also shows the current global-local methodology results at the maximum displacement. The results are consistent with the regular ones and the analytical formulation.

Figure 3-13 and 3-14 include multiple curves. In Appendix C, supplementary plots are given separately for different mesh size selections to clearly show the difference between the analytical solution and FEA.

In static analyses, a mesh size of 0.1 mm is necessary if mesh regularisation is not applied. By mesh regularisation application, an element size of 1 mm is sufficient for the static analysis. However, this approach results in an error in the elastic region due to early softening.

Table 3-5 lists the arm reaction results for four different local mesh sizes with mesh regularisation. The analytical solution is the baseline for difference calculations. Table 3-6 shows the corresponding differences. Below the mesh size of 1 mm, regular analyses give differences below 1%, and global-local analyses give differences below 1.5 %. Therefore, the current method is verified with four different mesh sizes.

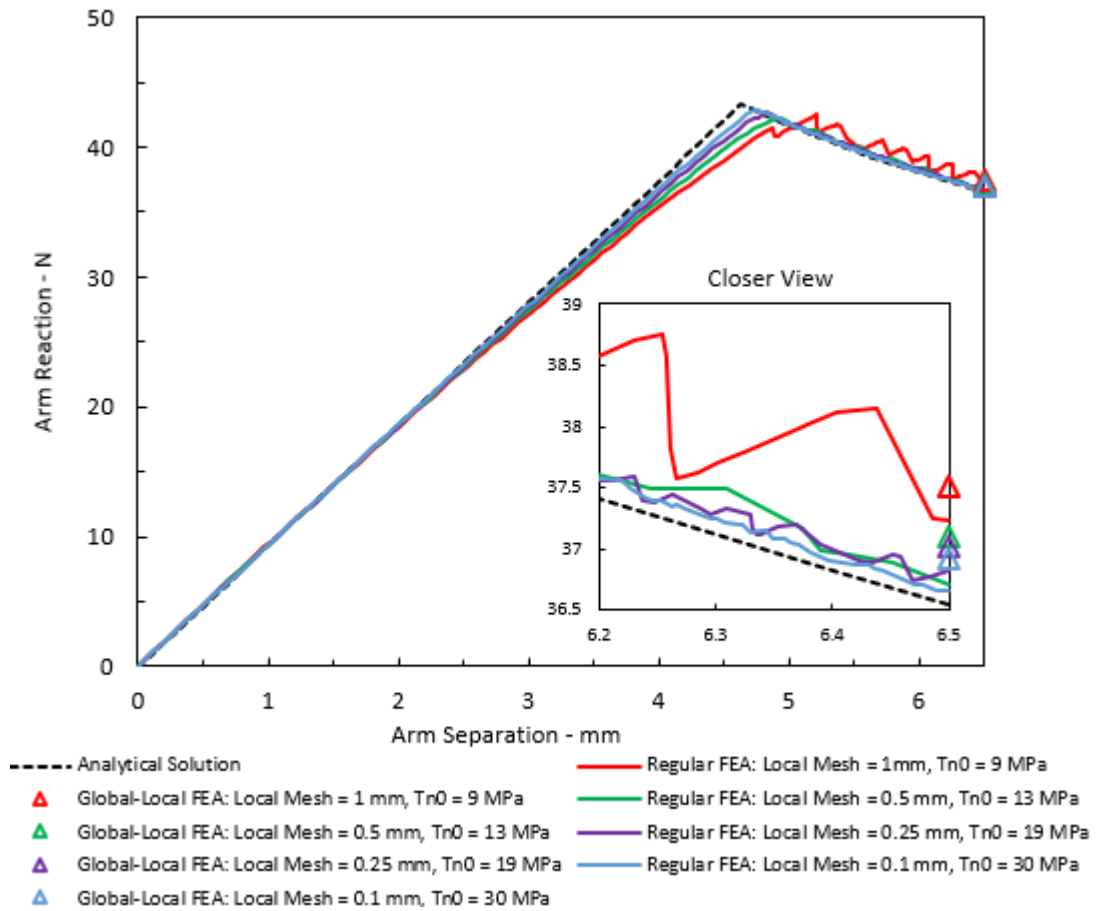


Figure 3-14 DCB Response for Different Mesh Sizes with Mesh Regularisation (Mesh Size other than the local region is 1 mm)

After verification of the method, the computational advantage is shown in Table 3-7. For the local mesh size of 1 mm, Global-Local analysis has a computational disadvantage. The regular analysis does not suffer from convergence issues since the number of damaged elements is small; on the other hand, for smaller mesh sizes, regular analyses suffer from convergence problems, and the current methodology improves computational effort by up to 48% for a local mesh size of 0.5 mm. For smaller local mesh sizing, the DOF of the local model is much higher than the global DOF. In this case, detailed local analyses require longer computational times. Therefore, the computational advantage is decreasing.

Table 3-5. DCB Model Arm Reaction Results for Different Local Mesh Sizes

	3D DCB Model Static Analysis: Arm Reaction Results		
	Analytical	Regular Analysis	Global-Local
Local mesh 1 mm	36.54 N	37.23 N	37.48 N
Local mesh 0.5 mm	36.54 N	36.71 N	37.06 N
Local mesh 0.25 mm	36.54 N	36.82 N	37.02 N
Local mesh 0.1 mm	36.54 N	36.67 N	36.92 N

Table 3-6. DCB Model Arm Reaction Differences for Different Local Mesh Sizes

	3D DCB Model Static Analysis: Arm Reaction Percent Differences	
	Regular Analysis	Global-Local Analysis
Local mesh 1 mm	1.9 %	2.6 %
Local mesh 0.5 mm	0.5 %	1.4 %
Local mesh 0.25 mm	0.8 %	1.3 %
Local mesh 0.1 mm	0.3 %	1.0 %

Table 3-7. DCB Model Computational Performance for Different Local Mesh Sizes

	$\frac{DOF_{Local}}{DOF_{Global}}$	3D DCB Model: Computation Times		
		Regular Analysis	Global-Local Analysis	Change
Local mesh 1 mm	0.09	26 min	34 min	29 %
Local mesh 0.5 mm	0.43	98 min	51 min	-48 %
Local mesh 0.25 mm	3.36	317 min	181 min	-43 %
Local mesh 0.1 mm	44.68	878 min	536 min	-36 %

### 3.2.4 The Effect of Selection of the Extent of the Local Region and Amount of Damage Propagation

The local region extent ( $L_{Local}$ ) is defined as the sum of the local region length on top of the initial crack surface ( $L_1$ ) and the local region beyond the initial crack tip ( $L_2$ ), as shown in Figure 3-15. The local region length values listed in Table 3-8 are selected for comparison. The ratio of  $L_1/L_2$  is kept nearly constant. A mesh size of 0.5 mm was selected for the calculations.

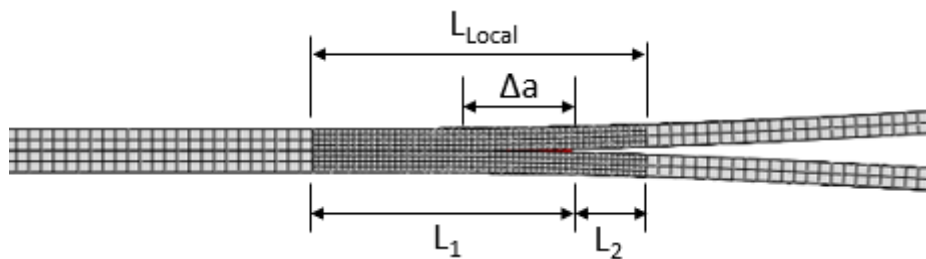


Figure 3-15 Definition of Local Region Extent

Moreover, different loading scenarios are considered, as shown in Table 3-9, which results in different damage propagation amounts  $\Delta a$ . The cohesive zone where the damage parameter  $\mathcal{D}$  is below 1 is excluded from the crack length  $\Delta a$ . In other words, the crack length is measured by considering cohesive elements with complete failure ( $\mathcal{D} = 1$ ).

Table 3-8. Selections of the Local Region's Extent

$L_{Local}$	$L_1$	$L_2$	$DOF_{Local}/DOF_{Global}$
14.5 mm	11 mm	3.5 mm	0.28
17 mm	13 mm	4 mm	0.33
22 mm	17 mm	5 mm	0.43
27 mm	21 mm	6 mm	0.53

Table 3-9. Selections of the Expected Damage Propagation Length and Corresponding Arm Separations

$\Delta a$	2 mm	4 mm	6 mm	10 mm
$\delta$	5.1 mm	5.5 mm	5.8 mm	6.5 mm

Figure 3-16 shows the response of the DCB for different local region extents. Results become erroneous when the local region boundary (measured by  $L_1$ ) is close to the expected delamination length ( $\Delta a$ ). For example, the arm reaction is incorrect if  $L_1$  is 11 mm sufficiently close to the expected delamination length of 10 mm under arm separation of 6.5 mm. When  $L_1$  is 13 mm, the arm reaction is still erroneous but with a more acceptable level for arm separation of 6.5 mm. Similar behaviour is observed in the response due to other loadings listed in Table 3-9. From all the results, it is recommended that the new crack tip, after propagation, should have an offset of at least 6 mm to the local region boundary. Mathematically, the following requirement is recommended for accurate solutions.

$$\Delta a = L_1 - L_{offset} \quad (3-35)$$

$$L_{offset} \geq 6 \text{ mm} \quad (3-36)$$

On the other hand, global-local solutions are close to the analytical curve with a percentage difference from the analytical solution below 2% for the crack tip-local boundary offset greater than 6 mm. The global-local method is not applied for the erroneous results with the smaller offset.

Figure 3-17 shows the computational time of the regular and global-local analyses for the different local regions and the delamination propagation extent. Figure 3-18 shows the computational time per cent change of the global-local method from the regular analyses. The global-local method has no computational advantage for a delamination extent of around 2 mm. The global-local method has a significant computational advantage by increasing the delamination extent. From Figure 3-18, independent of delamination extent, the optimum local region extent for computational advantage of the global-local method is 22 mm, corresponding to a local-to-global DOF ratio of 0.43.

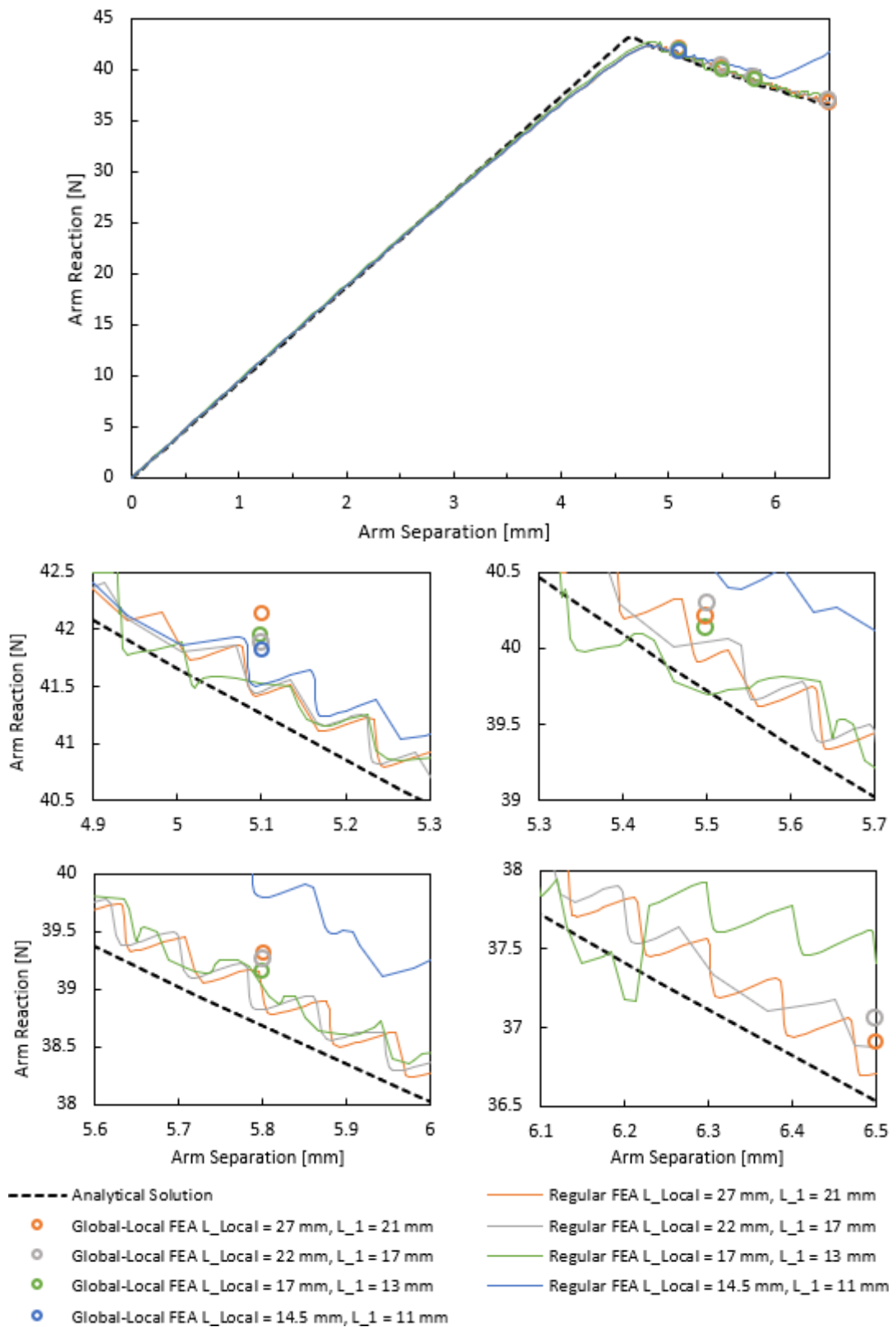


Figure 3-16 Arm Reaction-Separation Plots for Different Local Region Extent

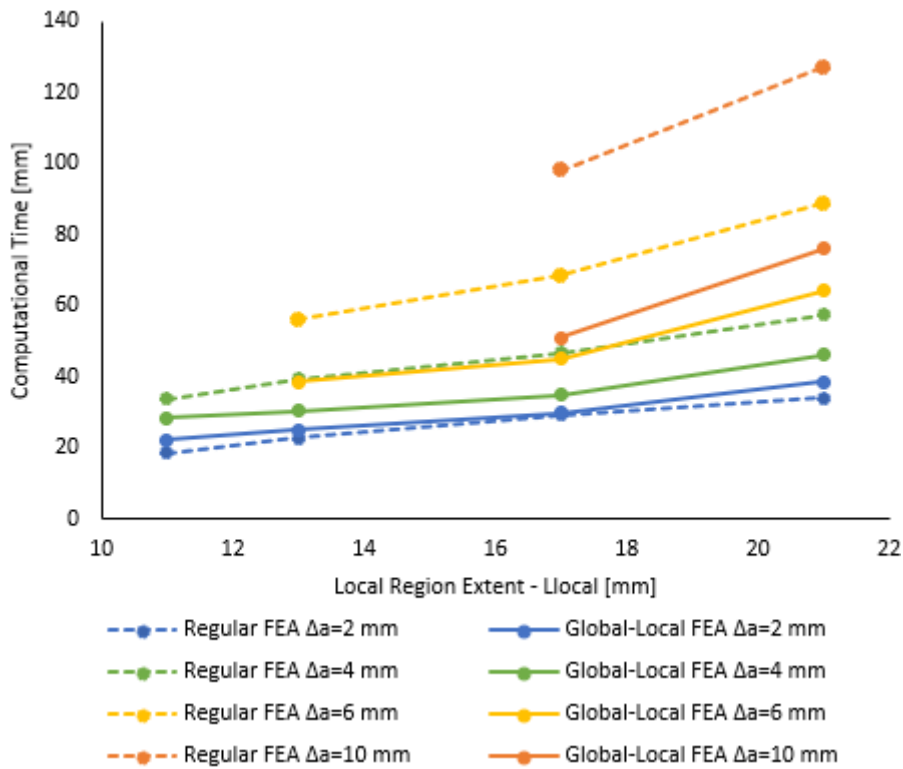


Figure 3-17 Computational Effort of Regular and Global-Local FEA for Different Damage and Local Region Extents

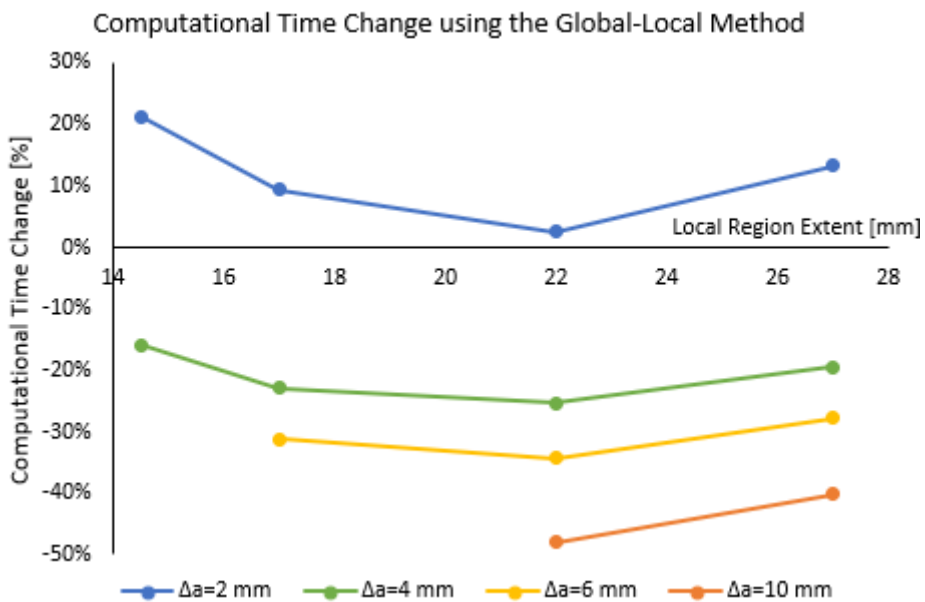


Figure 3-18 Computational Performance of Global-Local FEA to Regular FEA for Different Damage and Local Region Extents

### 3.2.5 Comparison of the Current Methodology with the Sub-Modelling Approach

The submodelling approach is a widely preferred method, especially in detailed stress analyses requiring very fine meshing, as concluded from the studies in Table 2-3. This method is not iterative, as the displacement field of the intact global model is applied to the local model once, as shown in Figure 3-19.

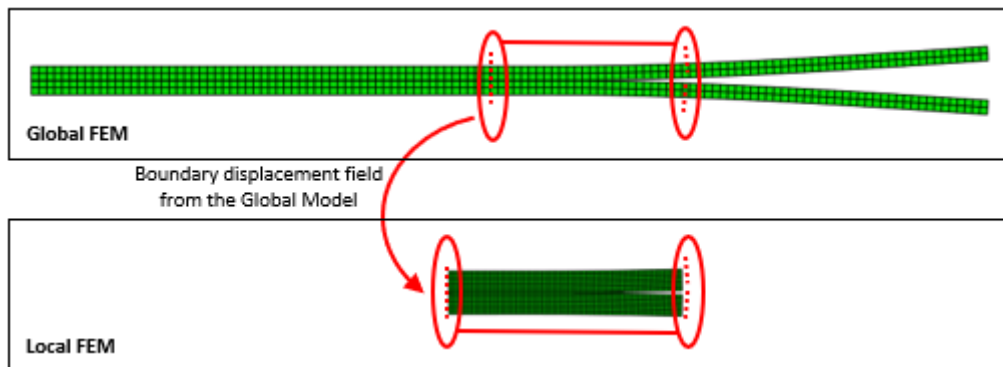


Figure 3-19 Submodelling Method

However, in the current DCB analyses, the crack length cannot be estimated by the sub-modelling method, as shown in Figure 3-20. This is due to the global model's significant displacement field and stiffness change as the damage propagates. In the studies in Table 2-3, the submodelling method is accurate in elastic analyses and useful in RVE applications without losing accuracy. However, this method leads to incorrect solutions for significant stiffness change in the global model, as shown in Figure 3-20.

On the other hand, the current two-way coupling methodology accurately calculates the crack propagation by comparing it with regular analysis. This shows that in the current example, where global model stiffness change is significant, a two-way global-local method is essential, which involves updating the global model according to the damage state of the local model.

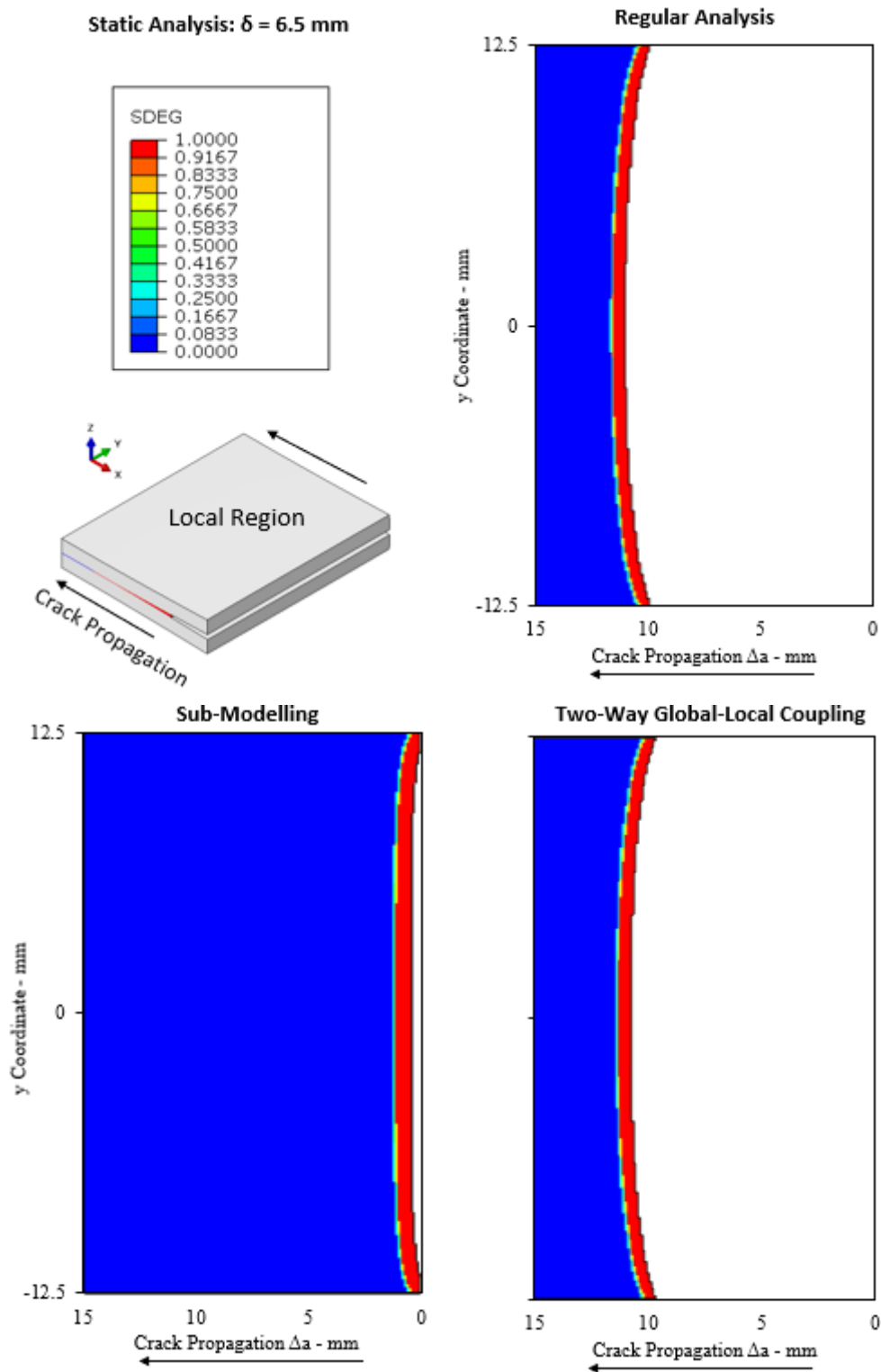


Figure 3-20 Delamination Propagation Results of Regular Analyses, Submodelling Method and Two-Way Global Local Coupling Methodology

### 3.2.6 Results and Discussions

Static analyses of the DCB with the local mesh size of 0.1 mm are examined in more detail. As shown in Chapter 4, a local mesh size of 0.1 mm is necessary for the fatigue analyses. Therefore, a mesh size of 0.1 mm is taken as the reference for the methodology.

Figure 3-21 shows static analysis results in the Arm Reaction versus Arm Separation plot. The model's analysis using the current method, regular FEA, and analytical solutions for comparison are presented.

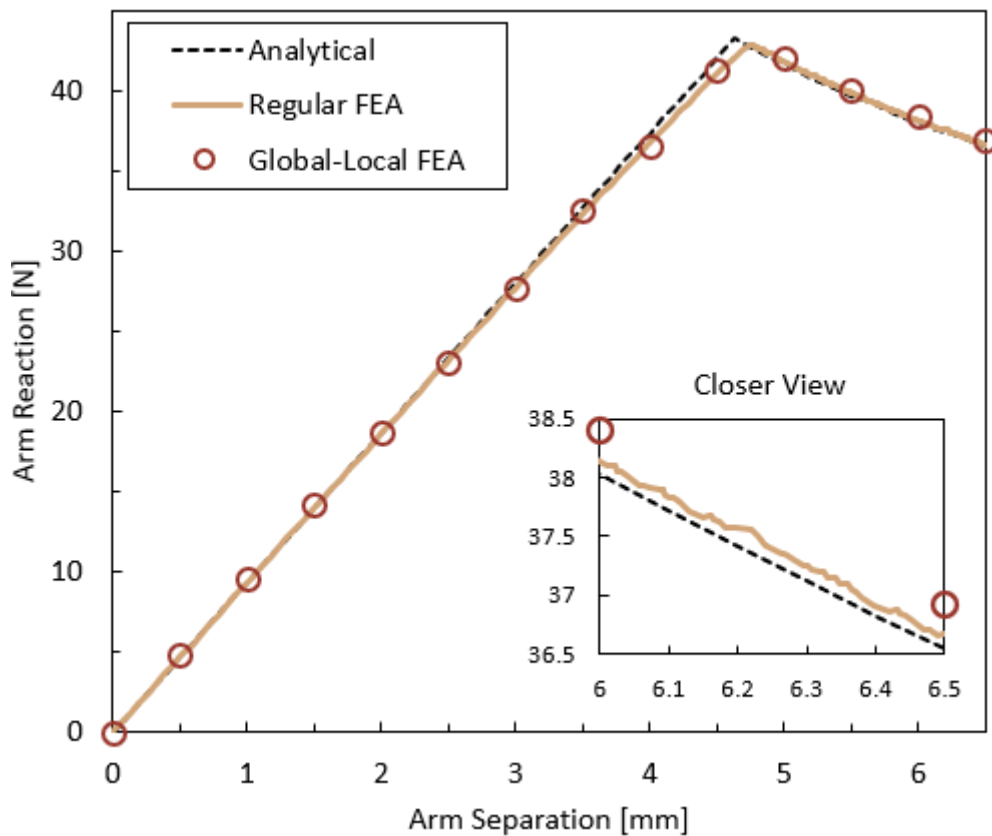


Figure 3-21 Arm Reaction versus Arm Separation Results

Table 3-10 numerically lists the maximum displacement arm reaction results shown in Figure 3-21, and Table 3-11 lists the corresponding percent differences from the analytical solutions. The current two-way coupling methodology provides consistent

results with the baseline analytical solution and regular analyses, with an arm reaction difference of around 1% from the analytical solution.

On the other hand, the delamination results shown in Figure 3-20 are also listed numerically in Table 3-10 for the maximum displacement, and the corresponding percent differences from the analytical solutions are listed in Table 3-11. The current two-way coupling methodology provides consistent results with the baseline analytical solution and regular analyses with a delamination length difference of around 1% from the analytical solution. Also, the results show that the current two-way global-local coupling methodology agrees well with the regular analysis and the analytical solution, which verifies the current method.

Table 3-10. Summary of Arm Reaction Results under Maximum Arm Opening of 6.5 mm

	Analytical	Regular Analysis	Global-Local
Arm Reaction	36.54 N	36.67 N	36.92 N
Delamination Length	69.5 mm	69.1 mm	68.7 mm

Table 3-11 Summary of Arm Reaction Percent Differences Based on Analytical Solution Reference

	Regular Analysis	Global-Local
Arm Reaction Percent Difference	0.4 %	1.0 %
Delamination Length Percent Difference	-0.6 %	-1.2 %

### 3.3 Application of the Method in Analyzing Tension-Torsion Experiments

#### 3.3.1 Test Setup

Tension-torsion tests were performed in METUWIND (ODTÜ-RÜZGEM), which Turkish Aerospace Industries fund. Figure 3-22 and Table 3-12 show the specimen geometry and tension loads. Figure 3-23 shows the test setup (1100 N.m MTS tension-torsion machine). All specimens are loaded with a maximum angle of twist of 40 degrees.

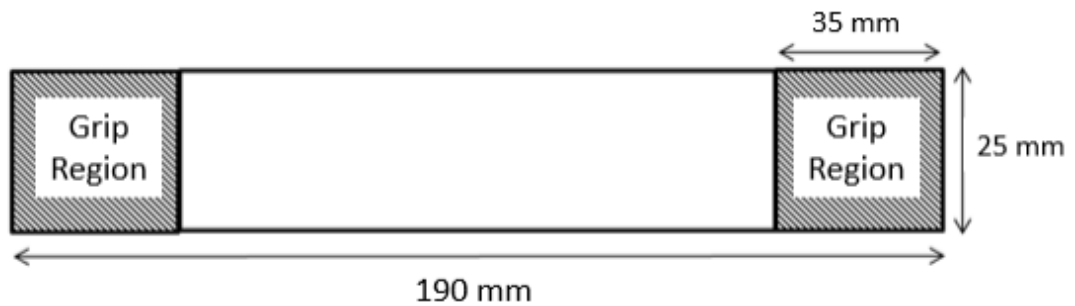


Figure 3-22 Tension-Torsion Specimen Dimensions

The specimens are selected as thick as possible to initiate edge delaminations, as shown in Table 3-12. Figure 3-24 shows a typical failure. Delamination is perceived after an audible click sound and a sudden torque drop.

Table 3-12 Pure Torsion and Tension-Torsion Specimens

Specimen Set	Stacking Sequence G: GFRP, C: CFRP	Thickness t (mm)	Angle of Twist $\varphi$ (deg)	Axial Force $F_x$ (kN)
T1	[ (0 <sub>32</sub> ) <sub>G</sub> ]	7.30	40	0
T3	[ (0 <sub>13</sub> ) <sub>C</sub> / (0 <sub>16</sub> ) <sub>G</sub> / (0 <sub>13</sub> ) <sub>C</sub> ]	7.07	40	0
TT3	[ (0 <sub>13</sub> ) <sub>C</sub> / (0 <sub>16</sub> ) <sub>G</sub> / (0 <sub>13</sub> ) <sub>C</sub> ]	7.07	40	45



Figure 3-23 Tension-Torsion Test Setup

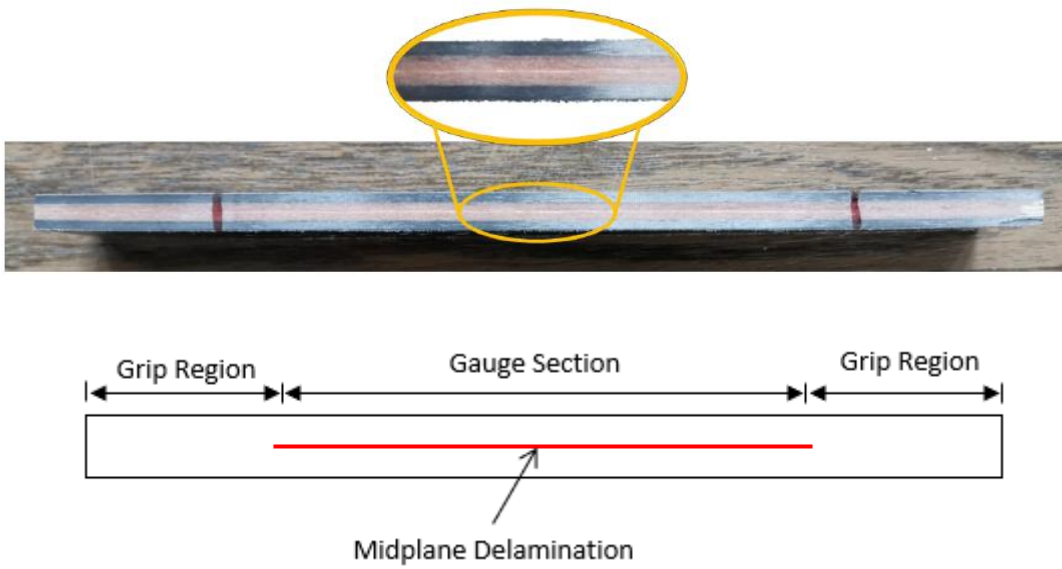


Figure 3-24 Delamination Failure

### 3.3.2 Finite Element Model

The geometry of the beam and applied boundary conditions are shown in Figure 3-25. The models consist of linear brick elements with improved surface visualisation (C3D8S). The interface of the local model is made of 3D cohesive elements (COH3D8). To capture edge delamination, the local region is selected at the edges located at the centre of the gauge region.

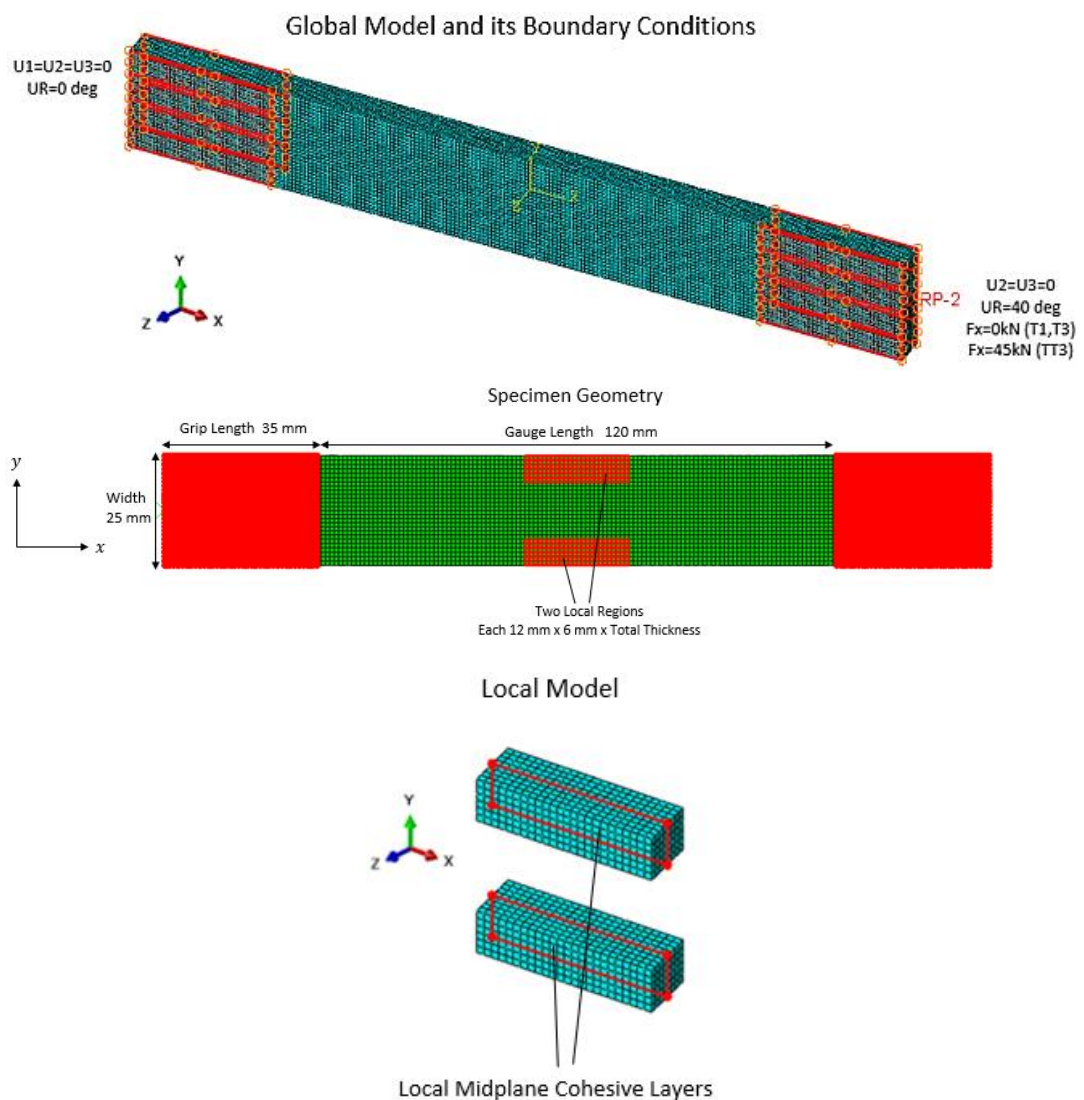


Figure 3-25 3D Beam under Tension-Torsion Model Geometry and Boundary Conditions

Grip regions are rigidly tied and assigned to reference points. At one end, the specimen is fixed, and at the other end, the angle of the twist and tension force (if it exists) are applied. According to test results, shear response is highly non-linear, so elastoplastic material modelling is necessary. The elastoplastic response is only assigned to shear stress-shear strain components. Normal stress and strain components are left linearly elastic. Figure 3-26 shows elastoplastic curves for the GFRP and CFRP materials. It is assumed that each shear component has an identical response.

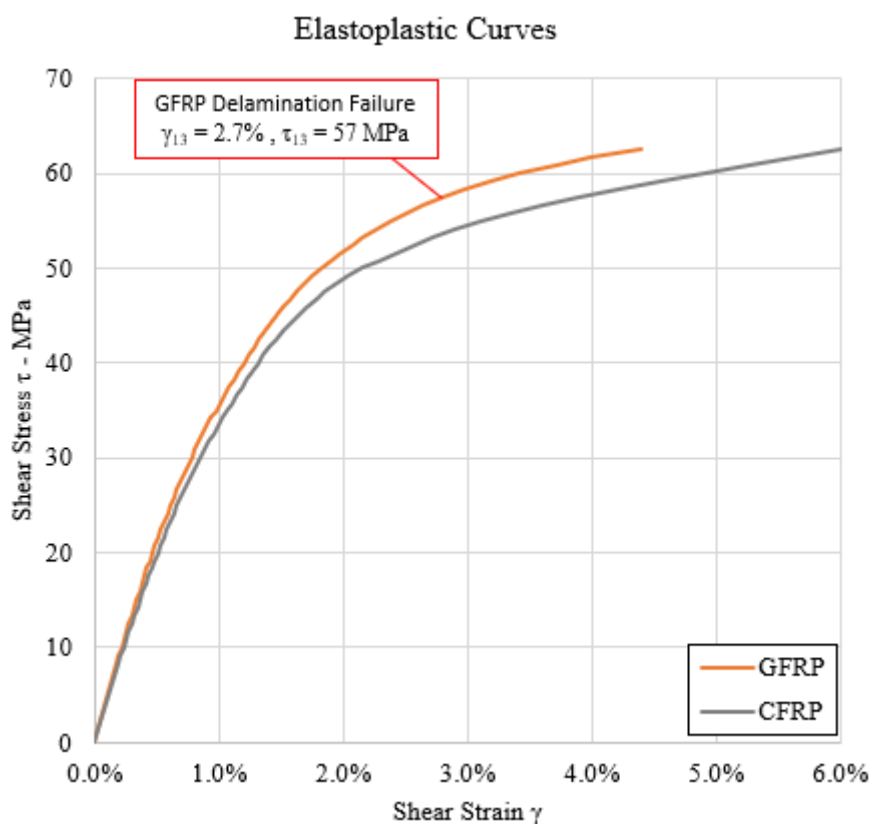


Figure 3-26 Elastoplastic Shear Responses

Experiments determine the failure point shown in the GFRP curve. It is based on the minimum failure load of pure GFRP (T1) specimens. In-plane shear response is not subjected to failure, as in the experiments, in-plane shear mode failure is not observed. On the other hand, the failure criterion is assigned to cohesive elements but not the host material itself. Interlaminar failure of CFRP material does not occur in the experiments.

### 3.4 Experiment and Analyses Results

#### Sensitivity Analyses

The specimens in each set have different thickness values measured; therefore, their effect is assessed in this section. Moreover, the effect of non-linear shear modulus, interlaminar shear strength (ILSS), and fracture toughness is assessed in this section. Representative sensitivity analyses are performed on the specimen set T1.

Initially, measured specimen thicknesses vary between 7.25 and 7.34 mm. Specimen average thickness is 7.30 mm. Figure 3-27 shows the torque-twist response of each specimen and corresponding analyses with maximum, minimum and average thickness. Between the specimens, there is no thickness-to-torque relation. For example, T1\_4 has maximum torsional stiffness in the intact region. However, its thickness is close to the minimum. Moreover, specimen T1\_1, having the maximum thickness, is one of the specimens with the lowest torsional stiffness. Furthermore, the thickness variation of the model does not cover the torsional response variability.

Figure 3-28 shows the variability of shear modulus. Scaling is applied to the elastoplastic curve of GFRP, as shown in Figure 3-26.  $G_0$  represents the nominal chord shear modulus as a function of shear strain. 3% stiffness variability covers the variation of torque-twist response of all specimens, as shown in Figure 3-28.

Figure 3-29 shows the effect of selecting the fracture toughness. Fracture toughness of 1 N/mm represents GFRP and CFRP materials under Mode II and Mode III loading. A fracture toughness value of 2 N/mm is also presented. Although this value is unlikely high for composite materials, its response cannot capture the specimens without delamination up to the machine limit of 40 degrees.

On the other hand, Figure 3-30 shows ILSS variation analyses. Slight variation of ILSS from 57 MPa to 62 MPa, minimum to maximum failure angle of twist and corresponding torque values can be captured. Therefore, the variation of failure points of the specimens may be due to the material variation in ILSS.

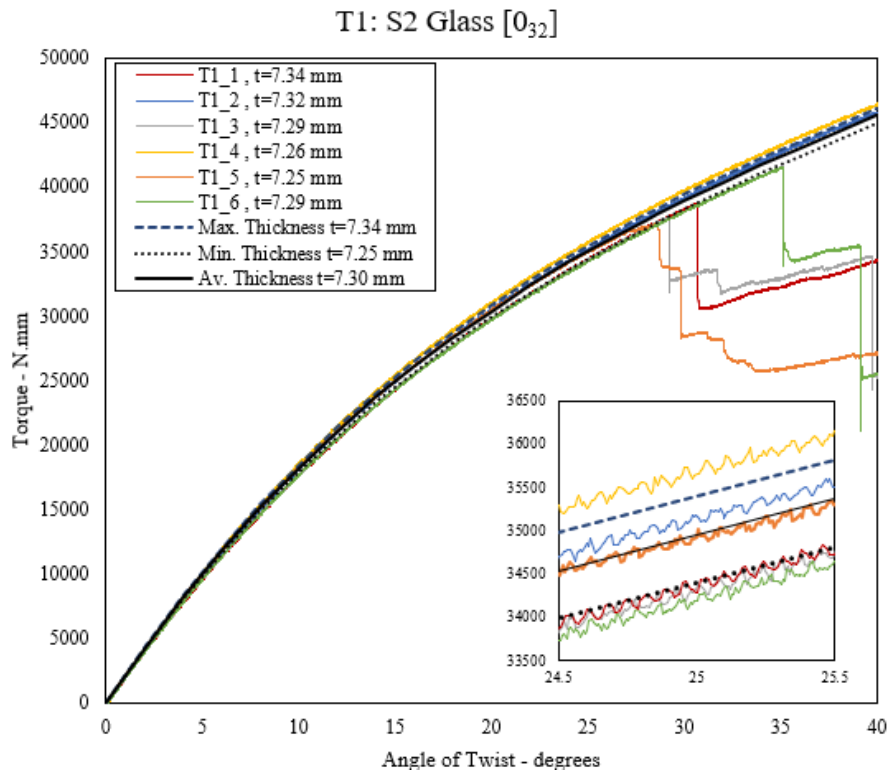


Figure 3-27 Thickness Sensitivity Results of T1 Specimens

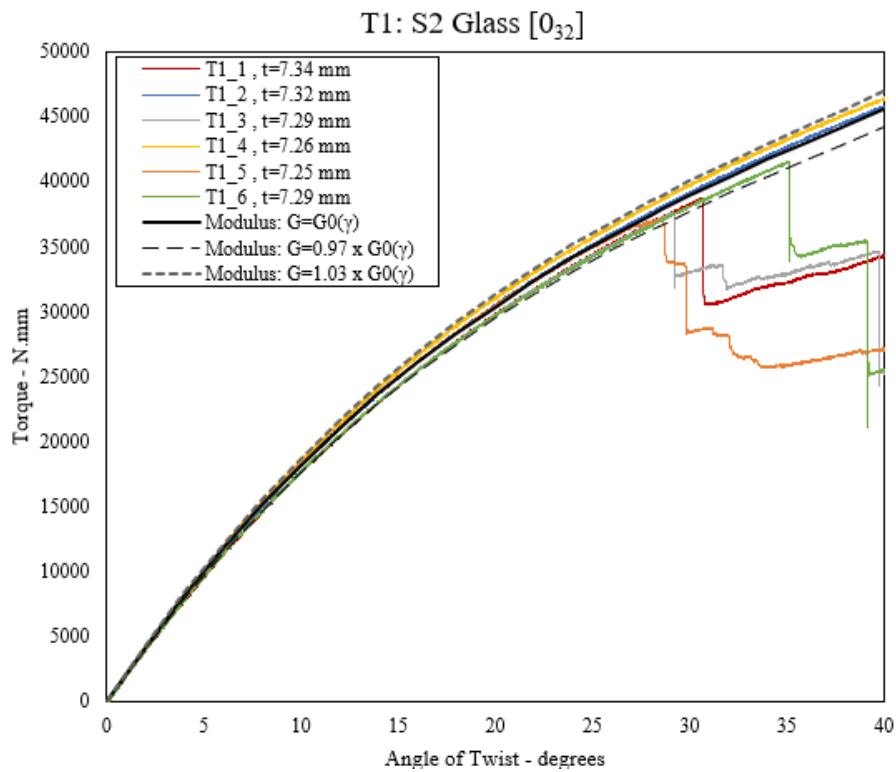


Figure 3-28 Shear Stiffness Sensitivity Results of T1 Specimens

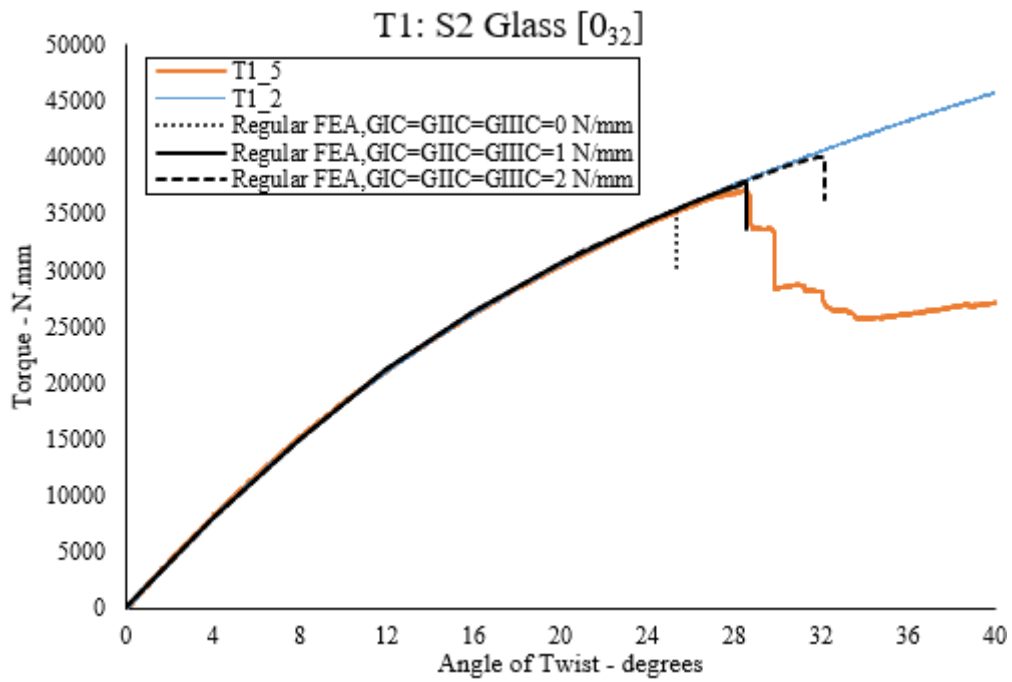


Figure 3-29 Fracture Toughness Sensitivity Results of T1 Specimens

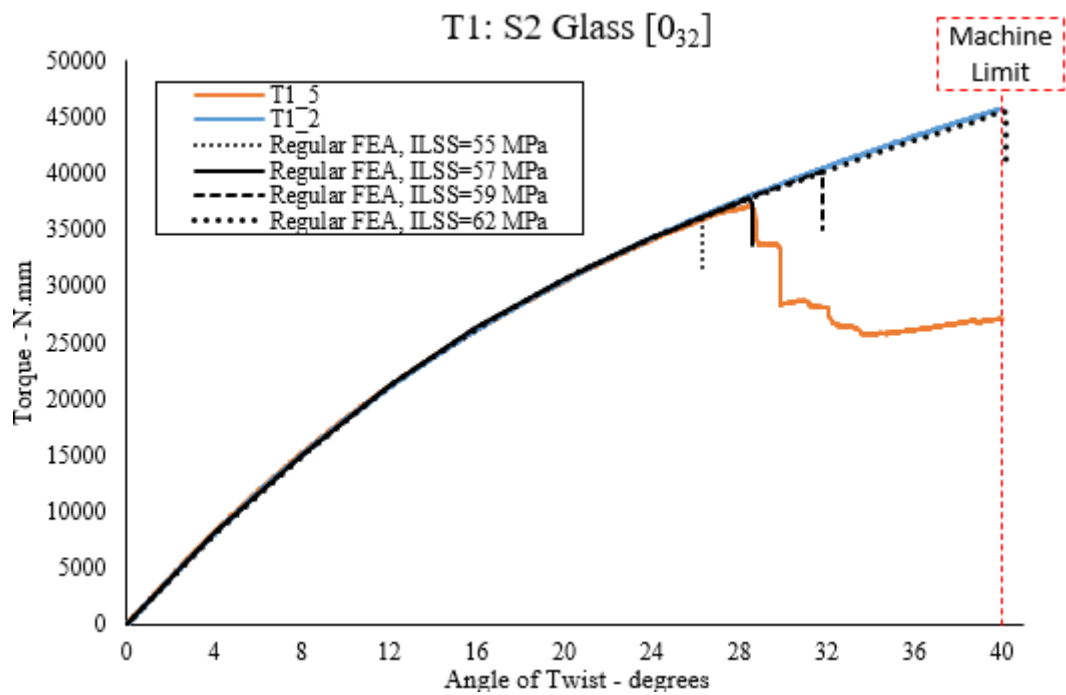


Figure 3-30 ILSS Sensitivity Results of T1 Specimens

## Delamination Failure Mode

The typical failure of the local region is shown in Figure 3-31. A damage depth of 5 mm is observed for regular and global-local analyses.

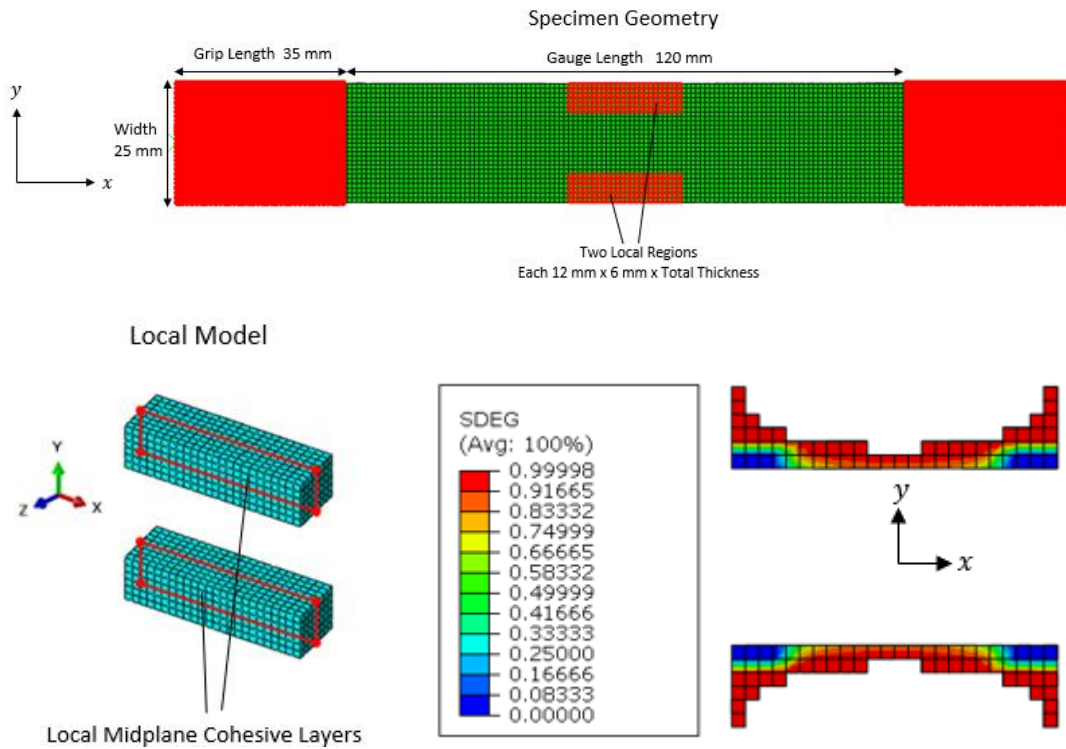


Figure 3-31 Local Failure of Cohesive Elements with a Depth of 5 mm

## T1 (Pure GFRP Torsion) Specimen Results

Figure 3-32 shows the Torque vs. Angle of twist responses. Among all specimens, the minimum failure point is observed at an angle of twist of 28.6 degrees. The regular analysis gives the same result. Global-local analyses are performed at 28.4 and 28.8 degrees (Near failure) to capture the delamination point correctly.

Figure 3-32 shows that damage is not observed in the global-local analysis at 28.4 degrees, just before the failure point. On the other hand, unstable damage propagation and torque drop are observed at an angle of twist of 28.8 degrees just after the failure. Therefore, the current method can capture the correct failure point with an accuracy of 0.2 degrees.

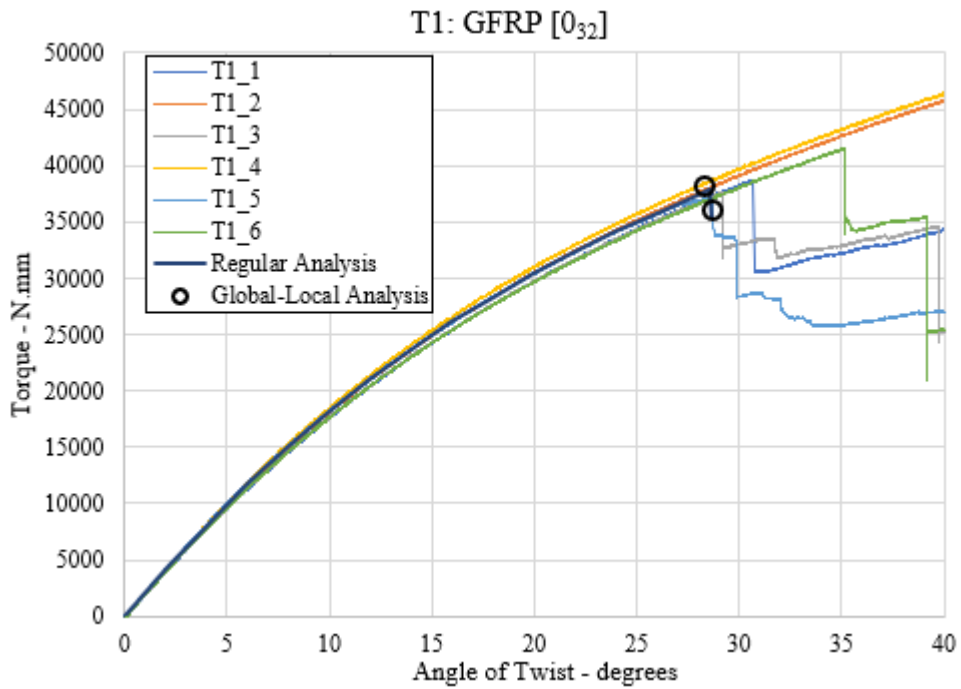


Figure 3-32 Torque vs Angle of Twist Plots of T1 Specimens

### T3 (Hybrid Torsion) Specimen Results

Figure 3-33 shows the Torque vs. Angle of twist responses. Among all specimens, the minimum failure point is observed at an angle of twist of 27.1 degrees. On the other hand, regular analyses give the failure point at an angle of twist of 26.9 degrees. Therefore, global-local analyses are performed for 26.7 and 27.1 degrees (Near failure) to capture the delamination point correctly.

Figure 3-33 shows that damage is not observed in the global-local analysis at 26.7 degrees, just before the failure point. On the other hand, unstable damage propagation and torque drop are observed at an angle of twist of 27.1 degrees just after the failure. Therefore, the current method can capture the correct failure point with an accuracy of 0.2 degrees.

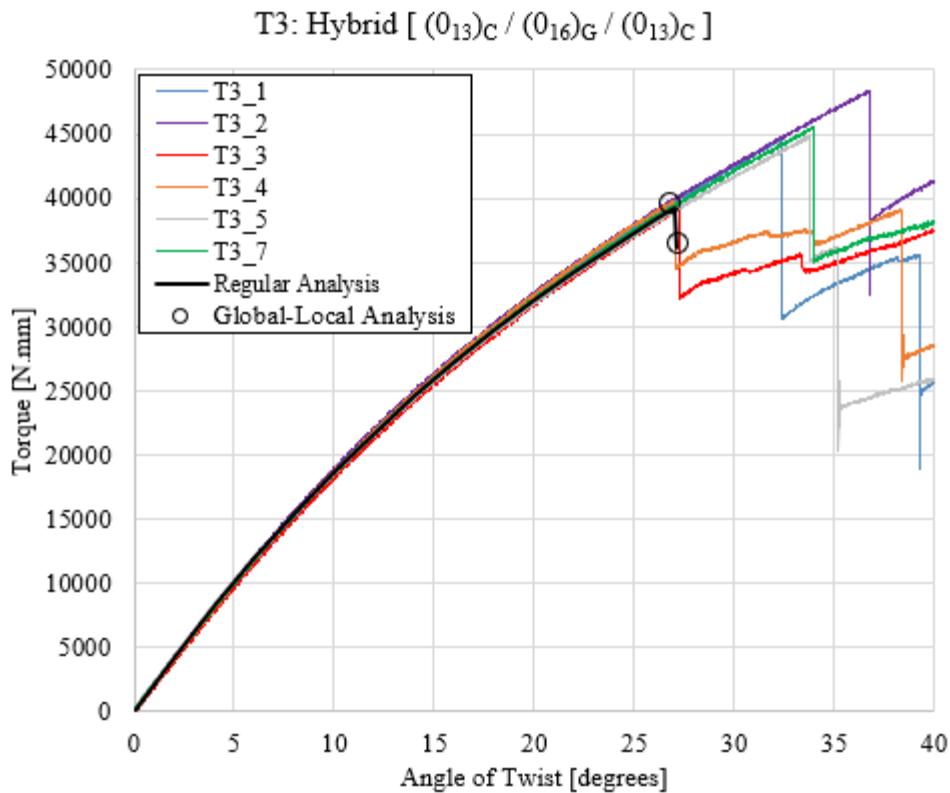


Figure 3-33 Torque vs Angle of Twist Plots of T3 Specimens

### TT3 (Hybrid Tension-Torsion) Specimen Results

Figure 3-34 shows the Torque vs. Angle of twist responses. The specimen is loaded by tension before the angle of twist loading. The failure behaviour is complicated for tension-torsion loading. A minor torque drop of one specimen is observed at an angle of twist of 28.4 degrees. After this minor drop, the specimen keeps its structural integrity up to the maximum twist angle of 40 degrees. The minimum angle of twist value for significant torque drop is around 37 degrees.

On the other hand, the regular analysis captures the failure location at 29.4 degrees, which is well below the significant torque drop but close to the minor torque drop point. Therefore, global-local analyses are performed for 29.2 and 29.6 degrees (in the vicinity of failure) to capture the delamination point correctly.

Figure 3-34 shows that damage is not observed in the global-local analysis at 29.2 degrees, just before the failure point. On the other hand, unstable damage

propagation and torque drop are observed at an angle of twist of 29.6 degrees just after the failure. Therefore, the current method can capture the correct failure point with an accuracy of 0.2 degrees.

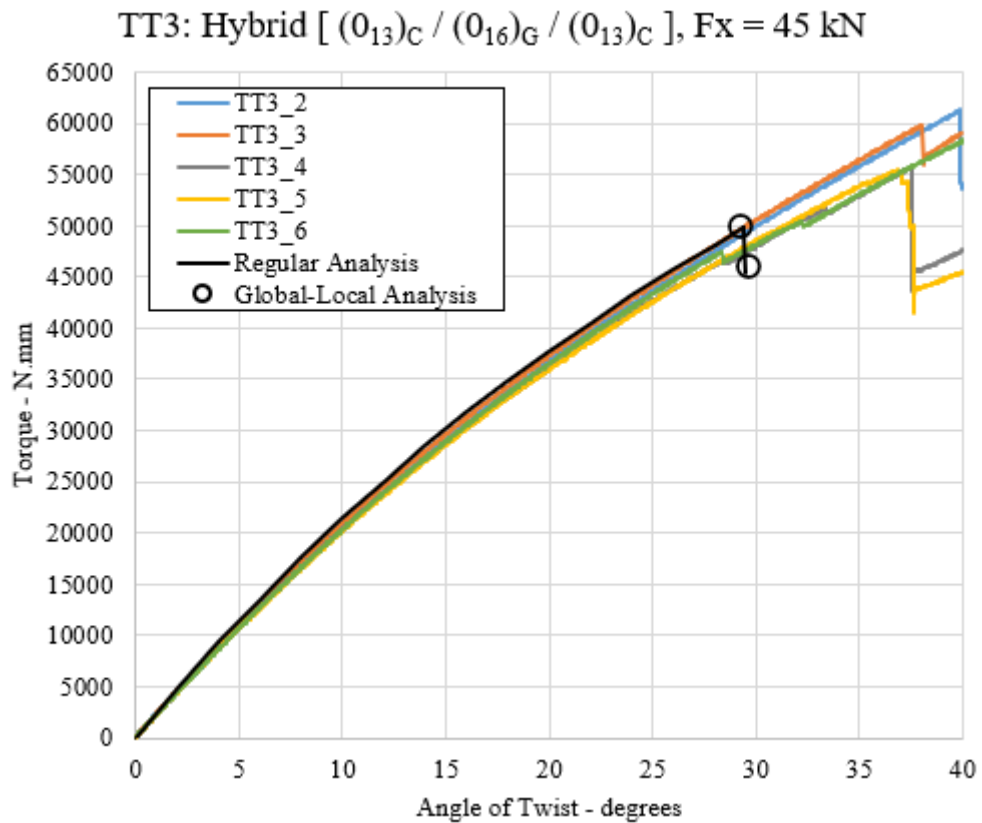


Figure 3-34 Torque vs Angle of Twist Plots of T3 Specimens

### 3.4.1 Stiffening Effect of Axial Force

Helicopter rotor blades undergo tremendous centrifugal forces, and bending and torsional stiffening are significant. T3 and TT3 specimens are identical, but one is loaded by pure torsion, and the other is loaded by tension and torsion. Therefore, it is possible to examine the effect of stiffening.

Although axial force does not significantly change shear strain and shear stress, it causes excessive torsional stiffening for wide specimens—an increase of torsional rigidity and, thus, corresponding torque at the specified angle of twist.

An increase in torque due to axial load at a specified twist angle can be expressed by Eq.(3-37) [140].

$$T = T_0 + \frac{d\varphi}{dx} \int_A \sigma_x (y^2 + z^2) dA \quad (3-37)$$

Where  $T_0$  is torque without tension (Pure torsion),  $T$  is the torque of the same beam under tension (Tension-Torsion). For wide rectangular laminate  $w \gg t$ , and for the average angle of twist gradient, torque expression simplifies to Eq.(3-38) [141].

$$T = T_0 + \frac{\varphi}{L} \frac{w^2}{12} F_x \quad (3-38)$$

Using Eq.(3-38), the Torque response of the TT3 specimen is estimated and compared by test results. Adding linear term  $\frac{\varphi}{L} \frac{w^2}{12} F_x$  The pure torsion response gives an estimated torque response as a function of the angle of the twist under tension and torsion.

Figure 3-35 shows the effect of torsional stiffening and its estimation by Eq.(3-38). The blue line represents the average test response of specimen T3 under pure torsion, solid orange lines represent the average test response of the corresponding specimens TT3 under tension and torsion, and dashed orange lines represent estimated torque curves of tension-torsion specimens by Eq.(3-38) from pure torsion curves which are consistent with the experimental curve.

On the other hand, the “X” sign represents the earliest failure point, according to analyses. The axially loaded specimen has a failure point with the angle of twist value larger than that of the pure torsion specimen. This contradicts Biot’s [140] conclusion.

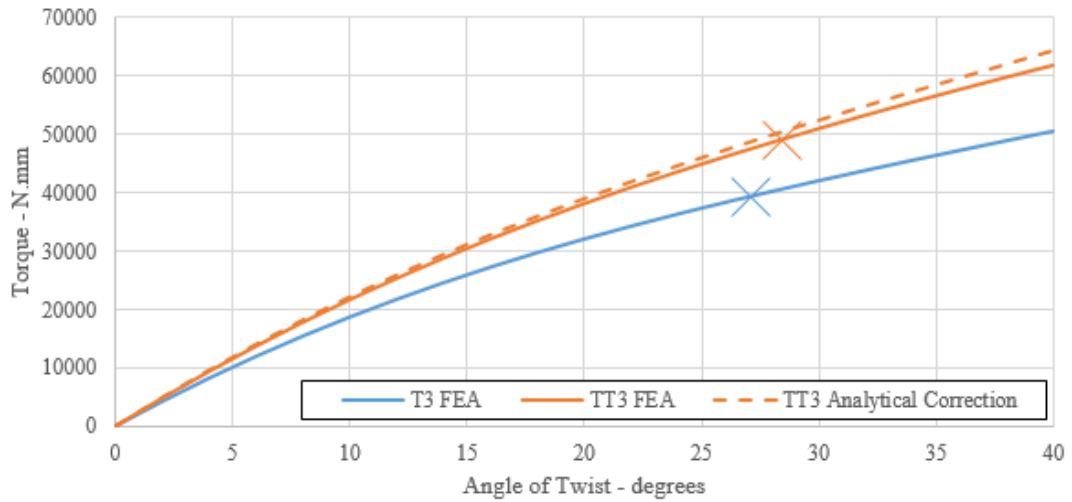


Figure 3-35 Effect of axial force on Hybrid (T3 and TT3) specimens

According to Biot [140], introducing axial force does not cause significant shear stress and strain change. Conversely, axial force decreases the tests' shear strain and corresponding shear stress magnitudes. However, the primary reason for this reduction is not the axial load itself. Shear strain is proportional to the span-wise angle of twist gradient  $d\phi/dx$  at the corresponding span-wise location unless it is close to the clamping (i.e. grip) region. The axial force causes torsional stiffening, which changes the angle of twist distribution and the corresponding span-wise derivative. If the specimen is stiffer in torsion, the angle of twist distribution is more uniform, which reduces the maximum angle of the twist gradient in the middle (See Figure 3-36).

The distribution of  $\phi$  and  $d\phi/dx$  severely depends on boundary conditions and specimen length. For very long beams,  $d\phi/dx$  is almost uniform, and the introduction of axial load does not result in a significant change in  $d\phi/dx$ . Therefore, introducing axial load does not decrease shear strain significantly for very long beams. Closed-form solutions for the span-wise angle of twist distribution are available in the literature but are not discussed here, as they are out of scope. In summary, especially for very long beams, it should be conservatively assumed that the introduction of axial load does not change shear stress and shear strain distribution. However, severe material interface discontinuities still exist under axial load.

Therefore, for the angle of twist-controlled analyses, the angle of twist values at failure are similar for pure torsion and tension-torsion specimens. On the other hand, there is a significant change in failure torque values. Hence, for tension-torsion specimens, the effect of axial force should be estimated by the angle of twist input. The current methodology can capture this effect correctly. Therefore, the method is also efficient under large centrifugal force applications.

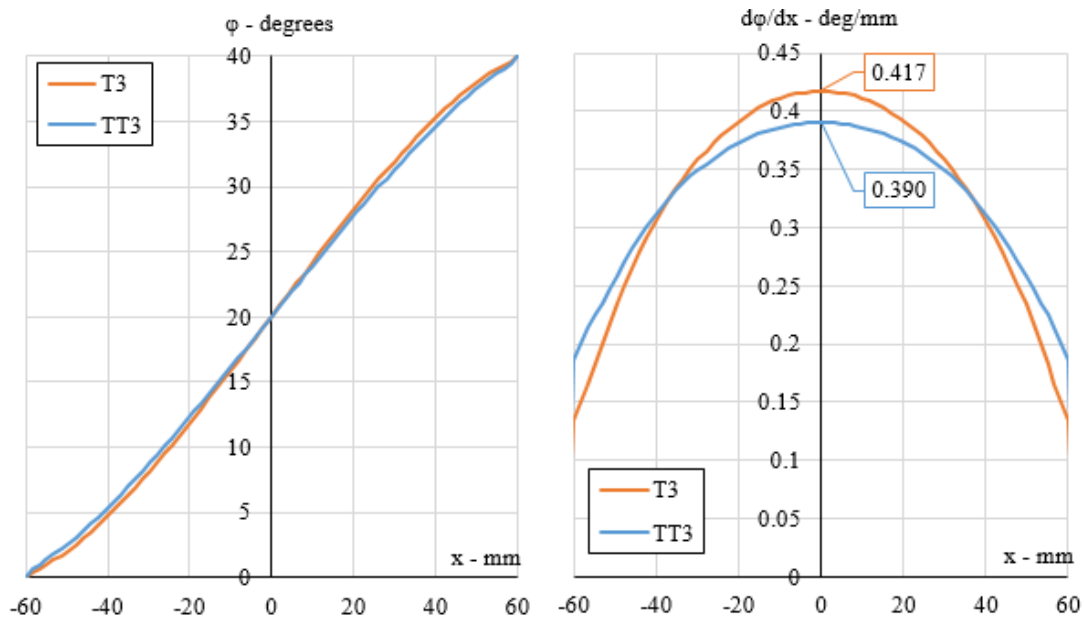


Figure 3-36 Effect of Axial Force on Distribution of Angle of Twist and its Spanwise Derivative

### 3.5 Conclusions

DCB is the simplest model for observing the interlaminar response and, therefore, is selected for the current method verification. The DCB material parameters are extracted from the standard experiments, and the analytical response and FEM are well correlated with experimental results.

Four different mesh sizes are selected in static analyses, and the mesh convergence study is performed. If mesh regularisation is not applied, a mesh size of 0.1 mm is necessary. By mesh regularisation application, an element size of 1 mm is sufficient

for the static analysis. However, this approach results in an error in the elastic region due to early softening. Moreover, the effect of the extent of the local region is assessed. The maximum computational reduction has a local region extent of 22 mm, corresponding to the local-to-global model's DOF ratio of 0.43.

This verified method in static analyses is applied to modelling tension-torsion experiments. Sensitivity analyses show that fracture toughness has a significant effect on failure load as well as ILSS.

The method can estimate failure load as its results are consistent with regular finite element analyses. The torsional stiffening effect due to axial force is significant in helicopter rotor blades. This increases failure torque, although the angle of twist value is similar. The global-local method also correctly captures this effect.

Table 3-13 compares the computation times of regular analysis and the two-way global-local coupling method. The current method has a significant computational advantage over regular analysis in DCB modelling, with a reduction of 36% for the local mesh sizing of 0.1 mm. On the other hand, this method shows a 44% to 52% computational advantage.

Table 3-13. Comparison of Computational Effort

	3D DCB Model Computational Effort		
	Regular Analysis	Global-Local	Difference
3D DCB Analyses	878 min	597 min	-36%
Pure Torsion Analyses (T1 Specimen)	55 min	26 min	-52 %
Pure Torsion Analyses (T3 Specimen)	56 min	27 min	-52 %
Tension-Torsion Analyses (TT3 Specimen)	61 min	34 min	-44 %



## CHAPTER 4

### FATIGUE ANALYSES BY TWO-WAY GLOBAL-LOCAL COUPLING METHOD

#### 4.1 Introduction

The methodology concerns interlaminar failure with CZM. Cohesive elements allow static analyses in Finite Element software such as Abaqus [126]. However, they lack the capability for material modelling under fatigue loads. Consequently, a UMAT material Subroutine, developed from the detailed formulation presented in Turon's dissertation [26], has been incorporated into the ABAQUS solver to enable fatigue analyses.

Figure 4-1 shows a typical fatigue crack growth law curve. This curve has three regimes. When the Strain Energy Release Rate (SERR) at the crack tip is below the threshold value ( $G_{th}$ ), there is no fatigue crack growth. When SERR is close to critical value (fracture toughness  $G_c$ ), fatigue crack growth is fast. If SERR is between threshold and critical value, crack growth obeys the Paris Law regime with a linear slope in a log-log plot. The vertical axis always has a crack growth rate, preferably on a log scale. The horizontal axis can be maximum or oscillatory SERR, as well as in log scale. The horizontal axis may be normalised by critical SERR. This study follows the Paris Law formulation in Eq.(4-1) for modelling the interlaminar fatigue crack growth.

$$\frac{da}{dN} = C(\Delta G)^m, \quad G_{th} < G < G_c \quad (4-1)$$

Threshold ( $G_{th}$ ) and critical ( $G_c$ ) strain energy release rates and Paris Law constants ( $C$  and  $m$ ) are material interface parameters. These parameters are determined from standard coupon-level experiments. In general, these material constants are failure

mode dependent. Paris law parameters selected in this study are mode-independent in this study. In Figure 4-2 in the study of Asp et al. [28],  $G$  vs  $da/dN$  trends are similar for different modes, being the most conservative for Mode I (DCB) loading.

The damage parameter in fatigue analyses combines static and fatigue damage parameters, as shown in Eq.(4-2). In the UMAT subroutine for fatigue analysis, this parameter is named “SDV1”, the solution-dependent variable in the subroutine.

$$\mathcal{D} = \mathcal{D}_{static} + \mathcal{D}_{fatigue} \quad (4-2)$$

The formulation given in the previous chapter applies to the static part. The analyses calculate static damage in the first cycle under maximum loading governed by pseudo-time (i.e. Step time) between 0 and 1. After this point, Eq.(4-3) gives the fatigue damage evolution.

$$\frac{d\mathcal{D}}{dN} = \frac{1}{a_{cz}} \frac{[\delta_f(1 - \mathcal{D}) + \delta_0\mathcal{D}]^2}{\delta_f\delta_0} \frac{da}{dN} \quad (4-3)$$

where for Pure Mode I loading, cohesive zone length is estimated by Eq.(4-4) [26].

$$a_{cz} = \frac{9\pi E_3 G_{max}}{32 T_0^2} \quad (4-4)$$

$E_3$  is the out-of-plane Young’s modulus of the host material. Crack length growth rate  $da/dN$  is determined by Paris law expression, which requires the calculation of oscillatory SERR given by Eq.(4-5).

$$\Delta G = \frac{T_0}{2} \left[ \delta_0 + \frac{(\delta_f - \delta_{max})^2}{\delta_f - \delta_0} \right] (1 - R^2) \quad (4-5)$$

The two-way global-local coupling methodology assesses the impact of localised changes within a computational model without requiring extensive modifications. The methodology explained in Section 3-1 is extended to fatigue analyses in this chapter.

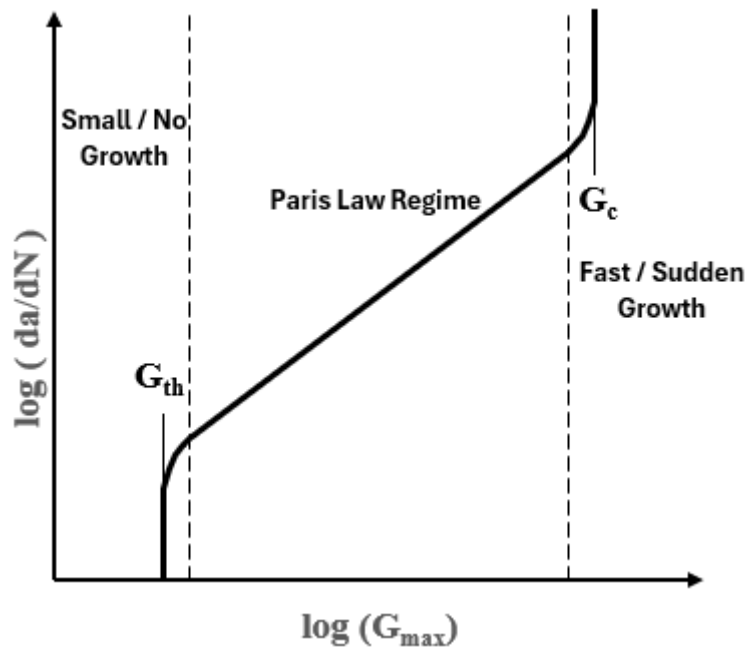


Figure 4-1 Cohesive Element Fatigue Response [26]

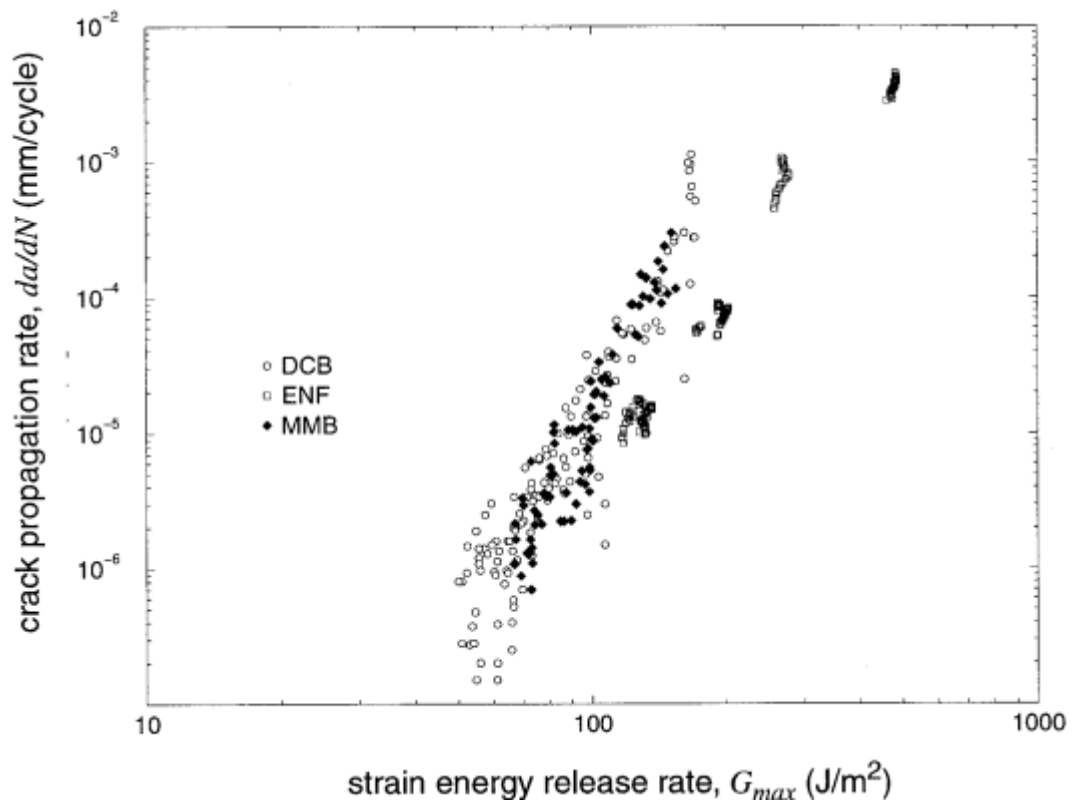


Figure 4-2 Typical  $G$  vs  $da/dN$  Plot for Mode I (DCB), Mode II (ENF) and Mixed Mode (MMB) Failure [28]

Using the Paris Law regime, the local model now involves cohesive elements with fatigue material formulation. In this framework, the pseudo-time in the static analysis step is replaced by the number of cycles. The Static General Step in Abaqus software also applies this analysis procedure. Figure 4-3 shows actual cyclic loading in fatigue analyses and the corresponding applied load in the Static General step in Abaqus software.

In cycles between 0 and 1, the load gradually increases to the maximum to calculate the static damage state. After this point, maximum load is constantly applied to the model. The load fluctuation is governed by the load ratio  $R$  embedded in the UMAT subroutine. Applying the maximum load with specified  $R$  in the Abaqus programme represents the actual sinusoidal loading.

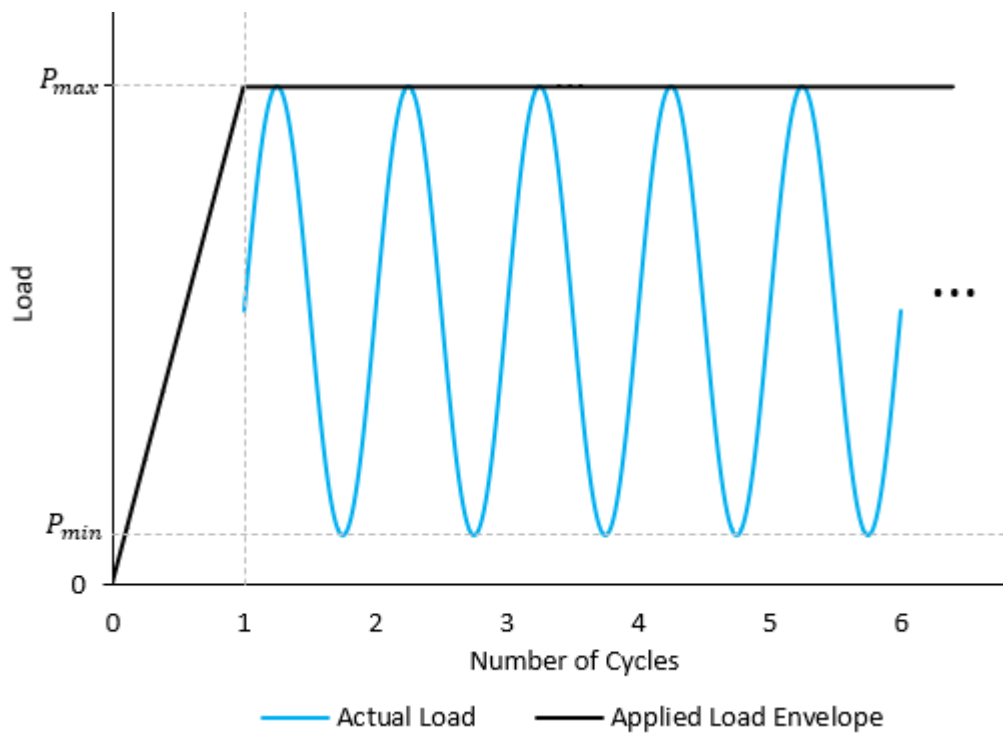


Figure 4-3 Actual Cyclic Load and Applied Load Envelope in FEA

## 4.2 Description of the Global-Local Finite Element Model

Figure 4-4 shows the Double Cantilever Beam (DCB) model. It is the simplest model for observing the interlaminar response in fatigue analyses. Because of its simplicity, closed-form solutions derived in Appendix D are available for comparison. Moreover, it suits the two-way global-local coupling analysis as the global stiffness is highly sensitive to local crack length.

Modelling was performed using the Abaqus CAE [126] interface. C3D8I brick elements with incompatible modes, with a side length of 1 mm for global and auxiliary models and 0.1 mm for local models, are selected. These elements are assigned orthotropic material properties of CFRP oriented at 0 degrees. Beams in the models are divided into two parts, connected by tie constraints in the global and auxiliary models and cohesive (COH3D8) elements in the local model.

In the global model, the left end of the beam is fixed, while the ends of the beam arms at the right are vertically opened relative to each other by an amount of  $\delta$ . Nonlinear geometric effects (large displacements - large strains) are included in the analyses. Maximum arm separations for static and fatigue analyses are shown in Table 4-1. The interface parameters are listed in Table 4-2.

## 4.3 Baseline Solutions

Regular finite element analysis has also been conducted to compare the accuracy and computation times of the global-local analyses. This model encompasses the entire structure. The damaged region of the structure is densely meshed, and the damage is modelled using cohesive elements. The parts of the model away from the damage are coarsely meshed, and the damage surfaces are connected with tie constraints. This model is an adaptation of the global-local model described in the previous section to the regular method, and it is expected that the solutions of the global-local analyses are consistent with the solution of this model.

Table 4-1. DCB Model Arm Separation Boundary Conditions

	Loading
Maximum Arm Separation $\delta_{\max}$	4.0 mm
Load Ratio R ( $\delta_{\min} / \delta_{\max}$ )	0.1

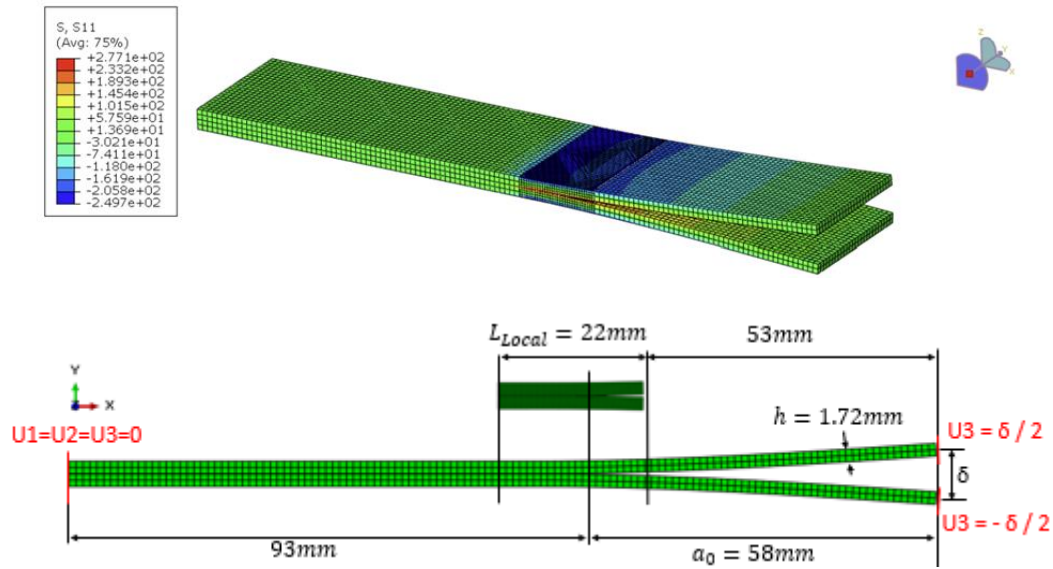


Figure 4-4. Double Cantilever Beam Finite Element Model

Table 4-2. Mode-I Interface Parameters

Parameter	Definition	Value
$G_{IC}$	Mode-I Fracture Toughness	0.20 N/mm
$G_{Ith}$	Mode-I Threshold SERR	0.06 N/mm *
$T_{no}$	Interlaminar Tensile Strength	30 MPa
$C$	Paris Law Constant	2440000 *
$m$	Paris Law Exponent	10.61 *

\*Taken from [142]

The DCB (Double Cantilever Beam) structure can also be solved analytically, and analytical solutions are provided as references for all solutions.

Under fatigue loading, the Paris law equation given by Eq.(4-1) has been integrated using the MBT expressions, resulting in the analytical solutions shown in Eq.(4-6) to (4-8). The derivation is given in Appendix D.

$$G_{max} = \frac{P_{max}^2(a + \chi h)^2}{D} \quad (4-6)$$

$$P_{max} = \frac{3D\delta_{max}}{2(a + \chi h)^3} \quad (4-7)$$

$$a + \chi h = \left\{ (a_0 + \chi h)^{4m+1} + (4m + 1)C \left[ (1 - R^2) \frac{9D\delta_{max}^2}{4} \right]^m N \right\}^{\frac{1}{4m+1}} \quad (4-8)$$

where  $\chi h$  is the crack length correction, and its expression is given in the study of Harper and Hallett [110]. A crack length correction of 3.2 mm from the static experiments is selected.

#### 4.4 Mesh Independency Study

For the DCB model, four mesh sizes—1 mm, 0.5 mm, 0.25 mm, and 0.1 mm—are selected. A mesh independence study is applied for static and fatigue analyses.

Figure 4-5 shows the DCB's fatigue response for four different mesh sizes and the analytical solution without mesh regularisation (Constant interface strength). Convergence is not achieved at a mesh size of 0.1 mm, but the solution with a mesh size of 0.1 mm is consistent with the analytical solution.

Figure 4-6 shows the fatigue response of the DCB for four different mesh sizes together with the analytical solution with mesh regularisation. However, mesh regularisation does not improve the solutions sufficiently, unlike static analysis. Moreover, the reduction of interfacial strength significantly reduces initial response (N=1) because of excessive softening.

Therefore, convergence is not achieved to a mesh size of 0.1 mm. The solution with a mesh size of 0.1 mm is consistent with the analytical solution. Furthermore, a global-local solution with a local mesh size of 0.1 mm is also shown. With a slight difference, the global-local solution is consistent with the regular one.

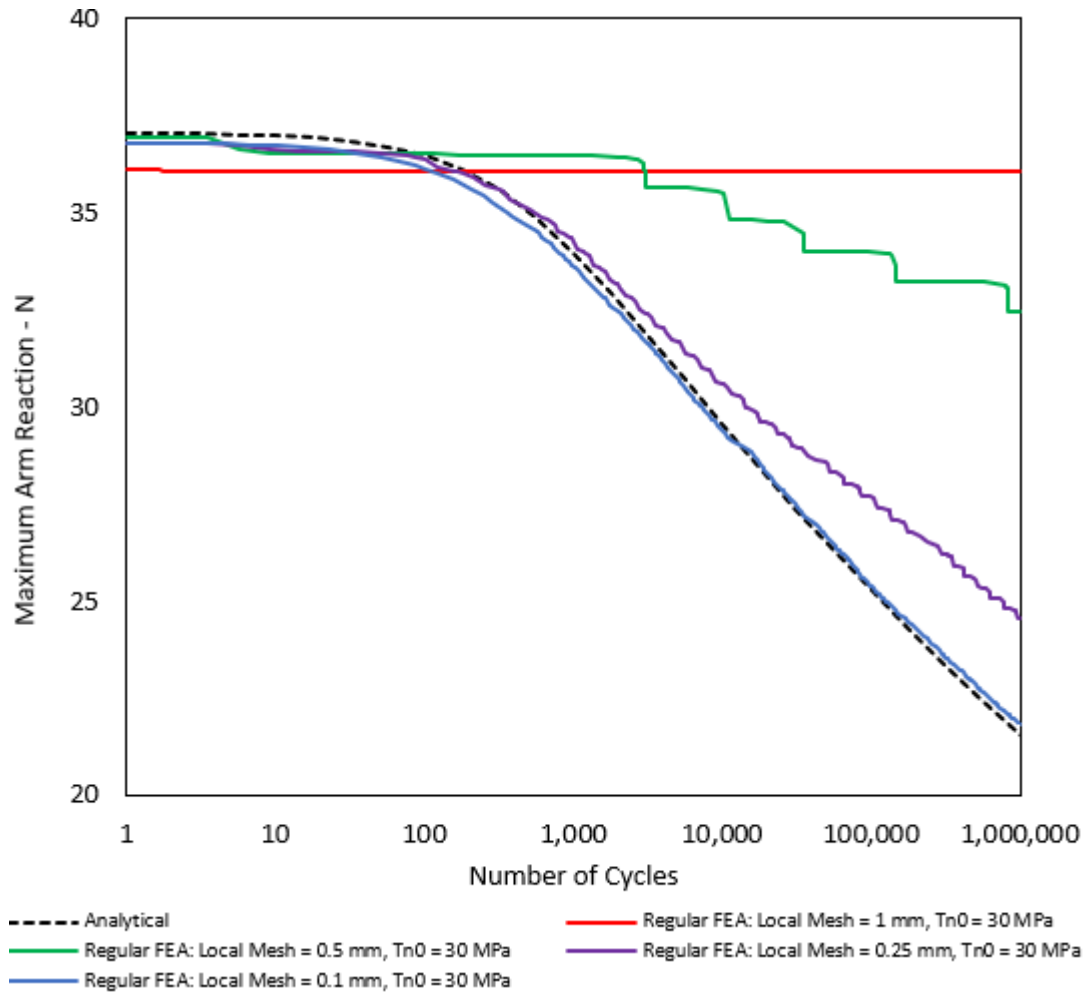


Figure 4-5 DCB Fatigue Response for Different Mesh Sizes without Mesh Regularisation (Mesh Size other than the local region is 1 mm)

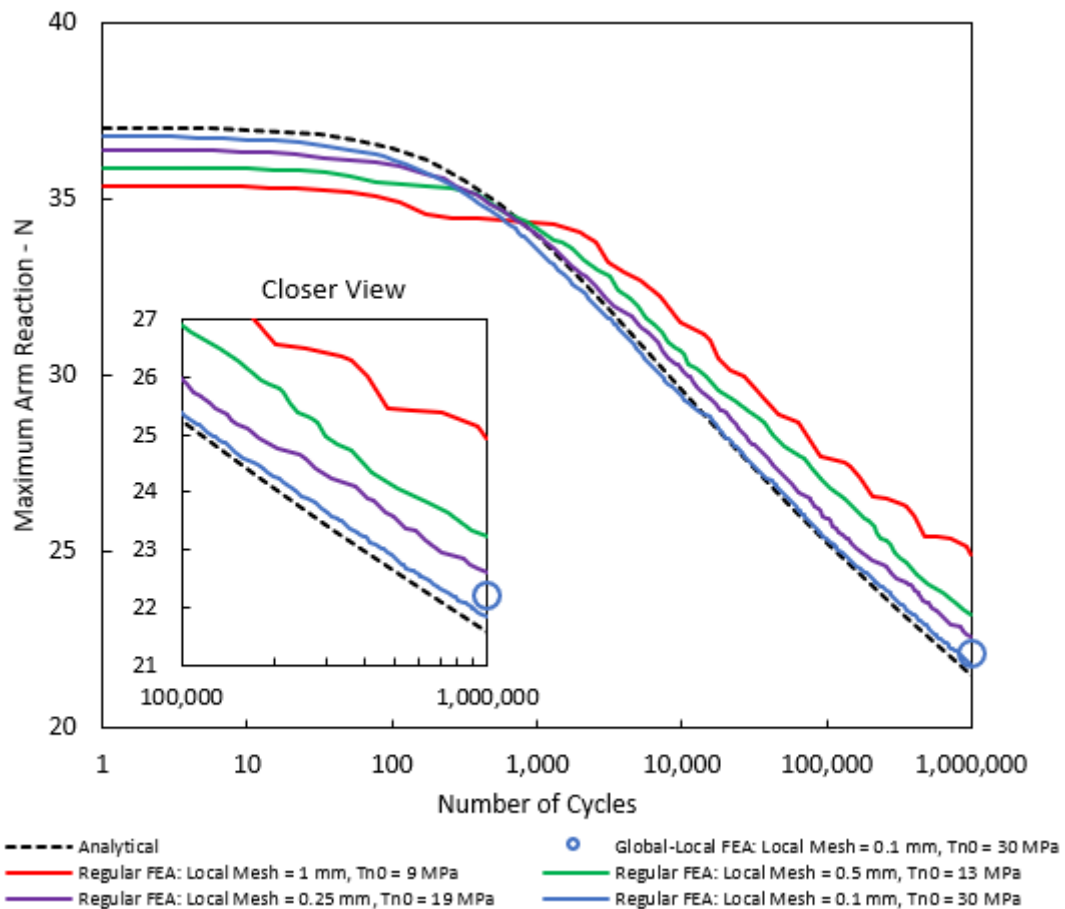


Figure 4-6 DCB Fatigue Response for Different Mesh Sizes with Mesh Regularisation (Mesh Size other than the local region is 1 mm)

#### 4.5 Comparison of the Current Methodology with the Sub-Modelling Approach

In the current DCB analyses, the crack length cannot be estimated, as shown in Figure 4-7, by the sub-modelling method. On the other hand, the current two-way coupling methodology accurately calculates the crack propagation by comparing it with regular analysis. This shows that in the current example, where global model stiffness change is significant, a two-way global-local method is essential, which involves updating the global model according to the damage state of the local model.

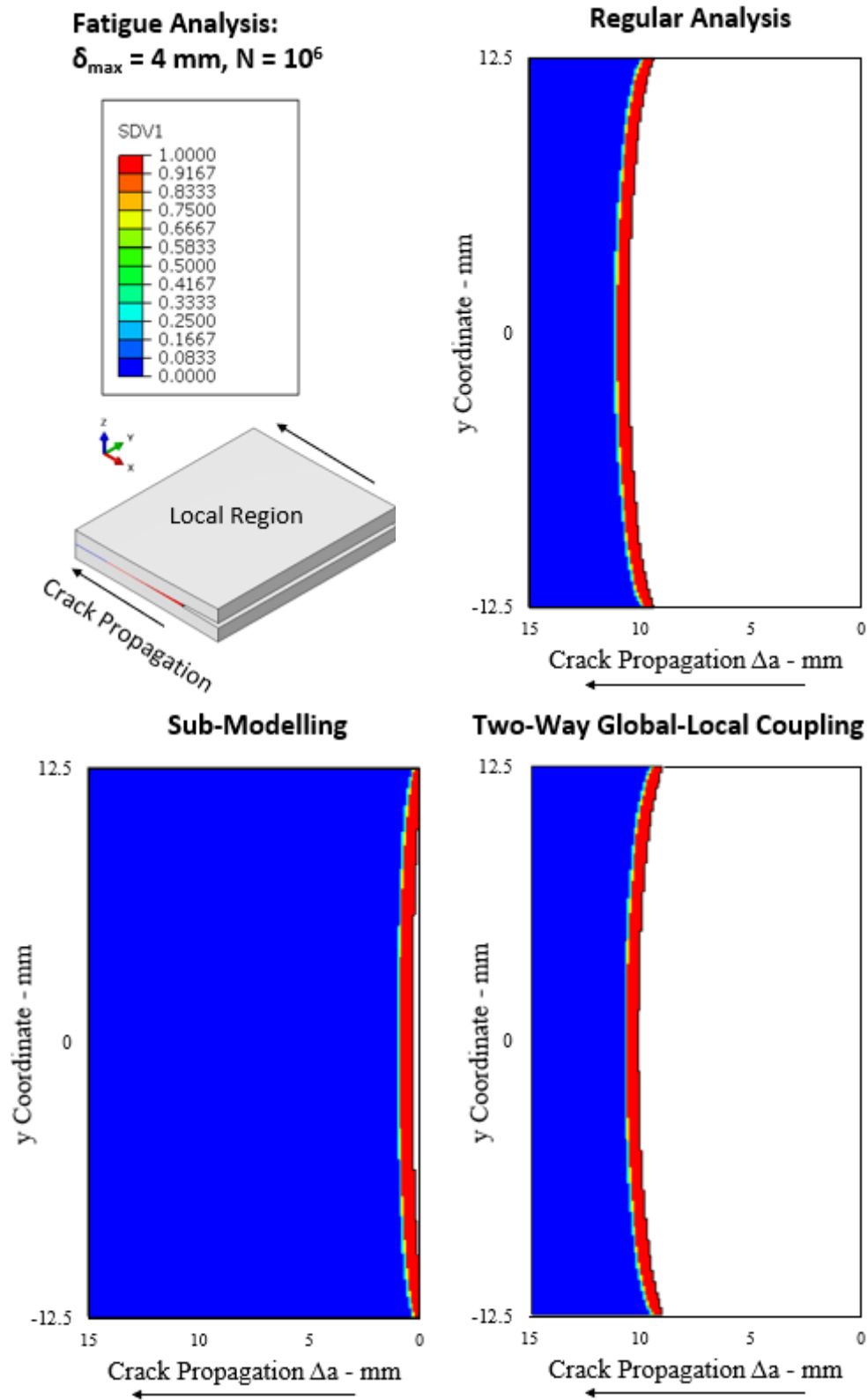


Figure 4-7 Damage of Cohesive Elements for the Fatigue Analyses

## 4.6 Results and Discussions

Figure 4-8 shows fatigue analysis results in the Maximum Arm Reaction versus Number of Cycles plot. The current method is in agreement with regular analyses and analytical solutions.

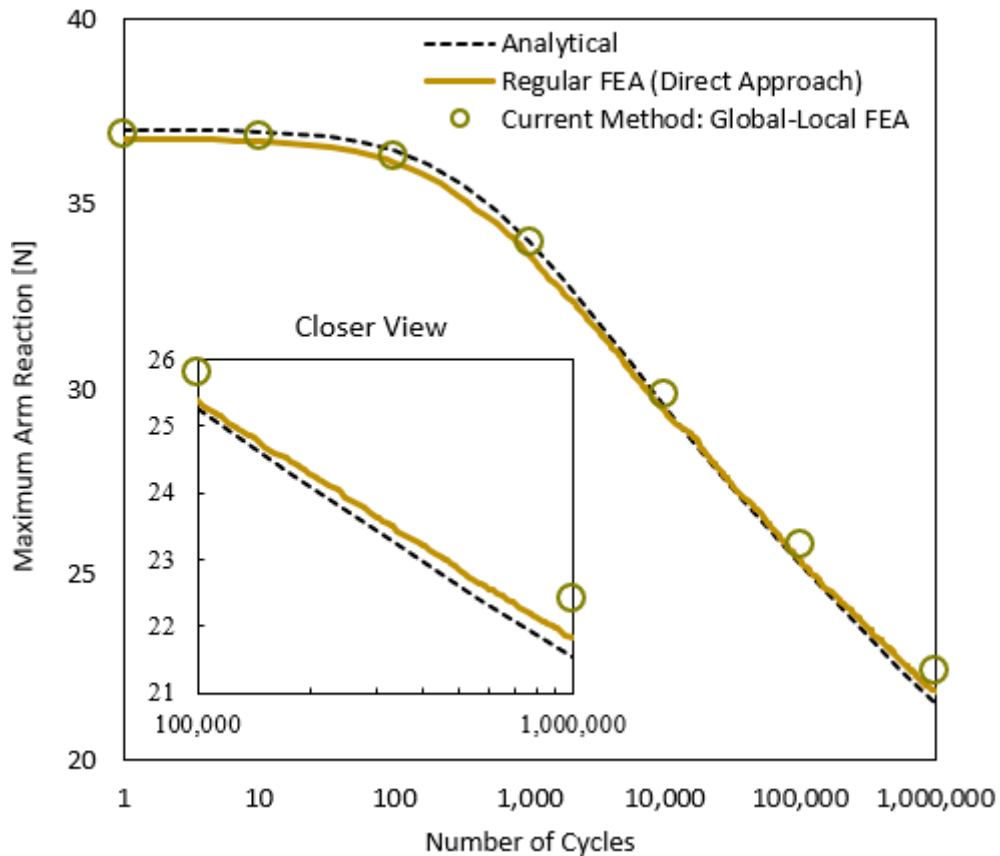


Figure 4-8 Arm Reaction Plots of the Fatigue Analyses

Table 4-3 lists the arm reaction results and corresponding differences. Analytical solution is the baseline for difference calculations.

Fatigue analyses suffer from mesh dependency. A Smaller mesh size like 0.05 mm results in enormous computation times and, therefore, is not considered, although mesh convergence is better.

Regular analysis has a difference of 3%, and the current method has an additional difference of 1.2%. The selection of smaller mesh sizes is expected to improve FEA

solutions. In conclusion, although there is a 3% difference between the regular analysis and analytical baseline, the global-local method is consistent with the regular analysis.

On the other hand, the current global-local methodology has a difference of 4.2% from the analytical solution. This is similarly due to mesh size selection. This method has a 1.2% difference from the regular analyses, which can verify this method.

Table 4-3. Summary of Arm Reaction Results

3D DCB Model Arm Reactions			Arm Reaction Differences	
Analytical Solution	Regular Analysis	Global Local	Regular Analysis	Global Local
21.50 N	22.14 N	22.41 N	3.0 %	4.2 %

Tables 4-4 summarise delamination extent results, and list the corresponding differences concerning the analytical solution as the baseline.

The current methodology is consistent with regular analysis and the analytical solution. Regular analysis has a difference below 1%, and the current method has a difference of 1.2%. In conclusion, the global-local method is consistent with the regular analysis and analytical baseline.

Table 4-4. Summary of Delamination Length Results

3D DCB Model Delamination Length			Delamination Length Differences	
Analytical Solution	Regular Analysis	Global Local	Regular Analysis	Global Local
69.1 mm	68.6 mm	68.3 mm	-0.7 %	-1.2 %

## 4.7 Conclusions

Four different mesh sizes are selected in fatigue analyses, and the mesh convergence study is performed. Mesh regularisation is insufficient in fatigue analyses. A mesh size of 0.1 mm is necessary for the correct solution. Section 4-6 show that the current methodology is verified in Fatigue Analysis.

Table 4-5 also compares the computation times of regular analysis and the two-way global-local coupling method. The current analysis method has a significant computational advantage over the regular analysis, with a reduction of over 30%.

Table 4-5. Comparison of Computational Effort

3D DCB Model Computational Effort		
Regular Analysis	Global-Local	Difference
2512 min	1708 min	-32%



## CHAPTER 5

### INTERLAMINAR FAILURE ANALYSES OF A T-JOINT STRUCTURE THROUGH THE TWO-WAY GLOBAL-LOCAL COUPLING METHOD

#### 5.1 Introduction

This method, validated for fatigue analyses, is applied to a T-Joint model, an element-level aerospace structure. The three-dimensional finite element model of the T-Joint has been adopted from the study by Ma et al. [143]. The study provides geometry and dimensions.

The static test setup is given in Figure 5-1, and the failure image after static pull-off loading is given in Figure 5-2.

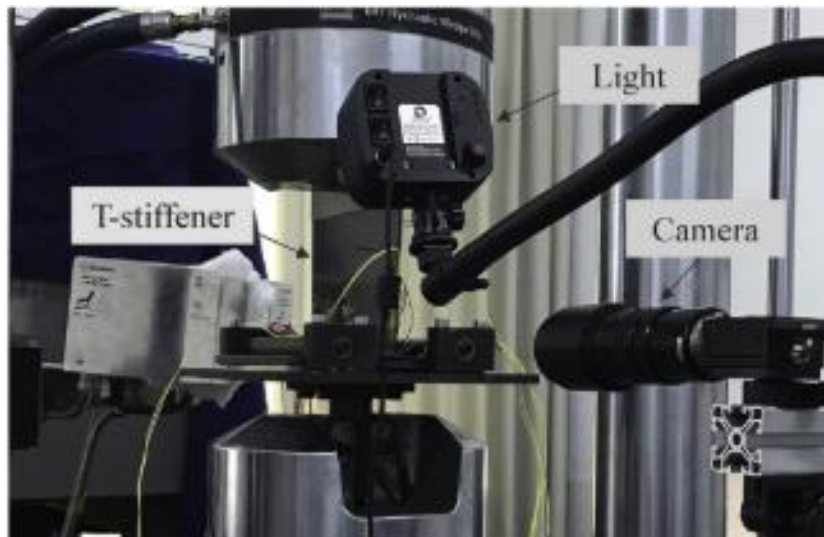


Figure 5-1 T-Joint Pull-off Quasi-Static Test Setup in the Study of Ma et al. [143]

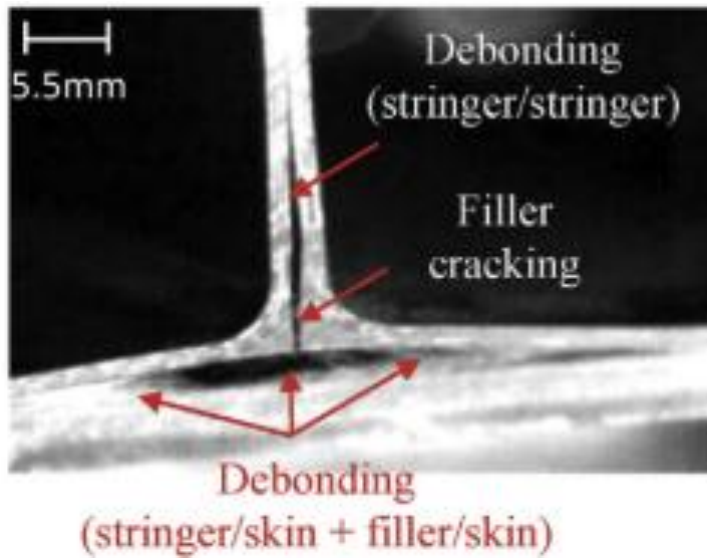


Figure 5-2 Failure Modes of the T-Joint Specimen after Pull-out Load [143]

First, the model validation is performed based on the experiments and static analyses from the study by Ma et al. [44]. The Global-Local method is not used in the validation phase, and the solution is carried out directly (i.e., the Regular method). This is because damage progression in the structure is unstable and sudden. Therefore, tracking minor damage, as in damage tolerance applications, is not feasible.

Regular analyses are performed on the finite element model discussed in Section 5.2. A displacement-controlled pull-off load of  $\Delta = 4$  mm is applied to the structure. Figure 5-3 compares the experimental data and FEA results from the referenced study [143] with the regular finite element analysis in the present study. The results are in good agreement.

## 5.2 Fatigue Analyses

The Global, Local, and Auxiliary models are shown in Figure 5-4. The out-of-plane width of all models is 200 mm. The mesh element sizes for the Global and Auxiliary models are approximately 1 mm. In the Local model, the mesh element size is set to 0.1 mm near the cohesive elements and 0.3 mm in more distant regions.

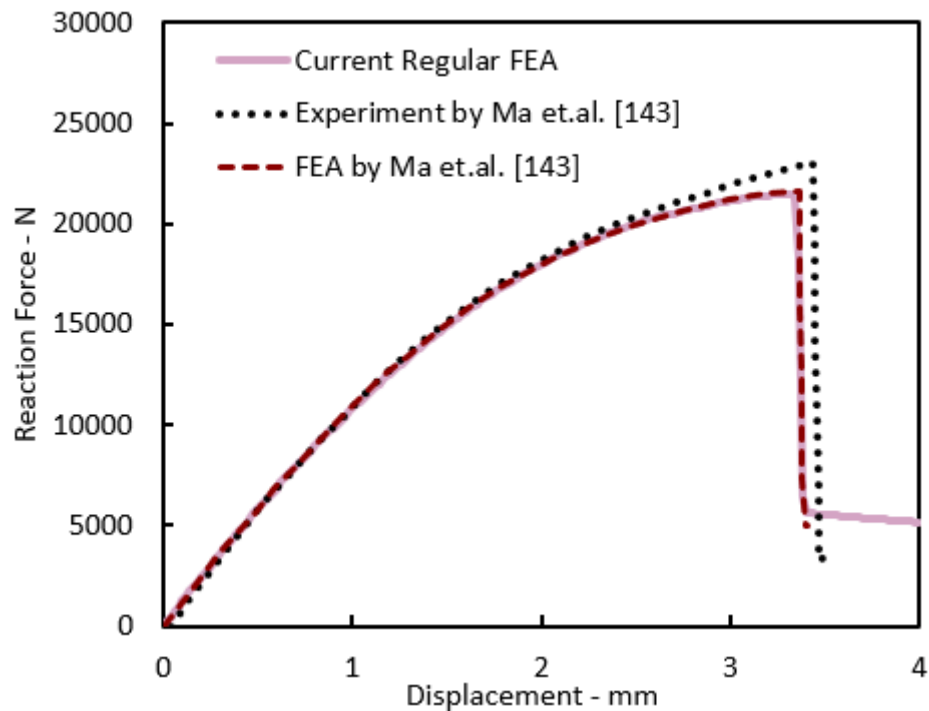


Figure 5-3 Comparison of Regular Analyses with the Results of Ma et al. [143]

The boundary conditions in the model are shown in Figure 5-5 and have been selected to be consistent with the study by Ma et al. [143]. The structure is constrained in the translation degrees of freedom at a distance of 20 mm from both the left and right ends. The end of the stiffener is first connected using the Continuum Distributing Coupling method and then pulled upward by a displacement of  $\Delta$  while keeping the other degrees of freedom fixed.

Ply layup directions are shown in Figure 5-6, and stacking sequences are shown in Table 5-1. The  $0^\circ$  ply is laid down in the out-of-plane direction (along the z-axis), while 90-degree plies are along the x-direction, shown in Figure 5-6.  $45^\circ$  plies of the stringer on the horizontal are symmetrical about the y-z plane, while stringers have the same  $45^\circ$  directions on the left and right sides of the joint at the vertical wall. This induces unsymmetric stacking in the left and right stringer-skin co-bonded sections. Moreover, the stringer layup sequence is unbalanced and also unsymmetric. Therefore, a slight asymmetry in the results is expected, although mesh structures

shown in Figure 5-4 are symmetric about the midplane of the vertical section of the stiffeners.

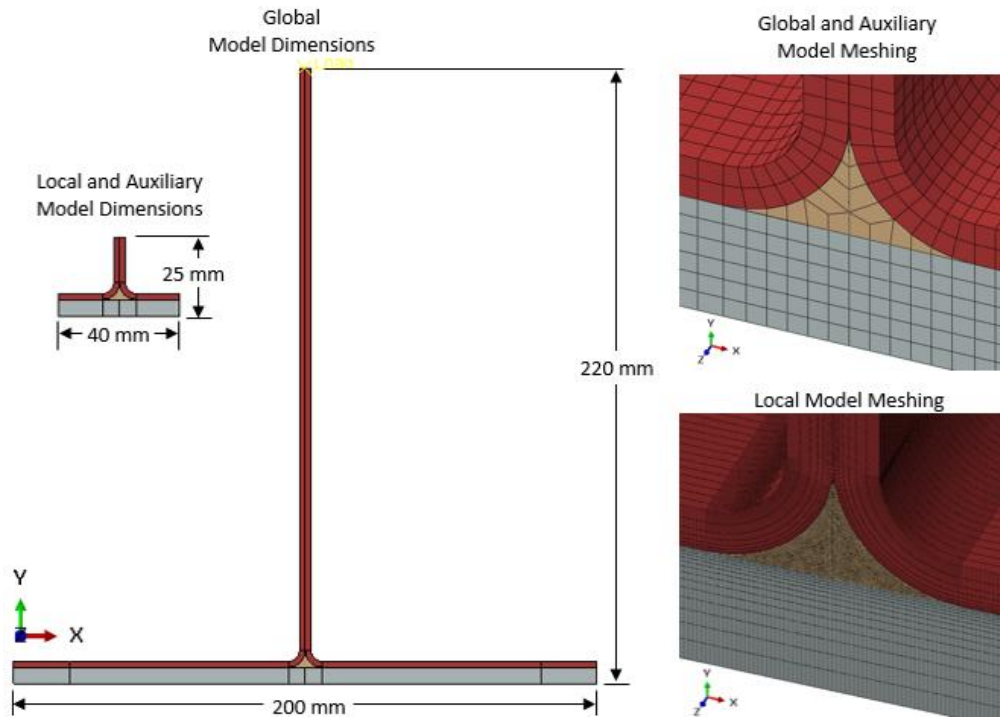


Figure 5-4 Global, Auxiliary and Local Finite Element Models of T-Joint Structure

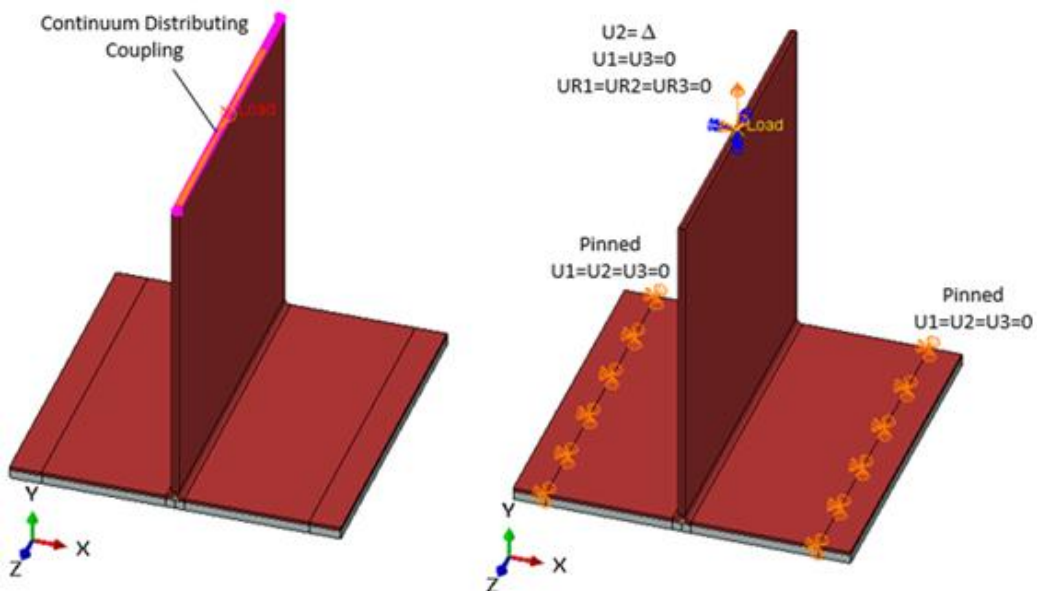


Figure 5-5 Boundary Conditions Applied on the Global Finite Element Model of T-Joint Structure

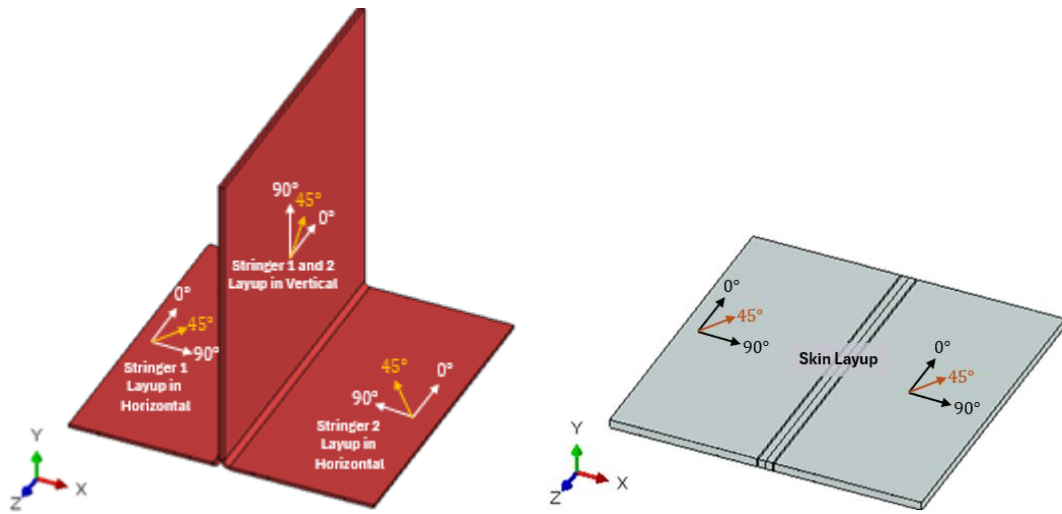


Figure 5-6 Ply Layup Directions of the T-Joint

Table 5-1. Skin and Stringer Stacking Sequences and Total Thicknesses [143]

	Stacking Sequence	Thickness
Skin	[45°/0°/-45°/90°/45°/0°/90°/0°/-45°/90°/45°/0°/45°]	2.0 mm
Stringer	[-45°/0°/45°/90°/0°/-45°/0°/45°/90°/0°/-45°/0°/45°/0°/-45°/45°] <sub>s</sub>	5.5 mm

Subsequently, fatigue analyses are performed on this model. The applied actual displacement load is given in Figure 5-7. According to the formula in the Abaqus software, the constant displacement value is applied as  $\Delta_{max} = 1.2$  mm. The oscillatory response is controlled using the UMAT subroutine with an input load ratio of  $R = 0.1$ .

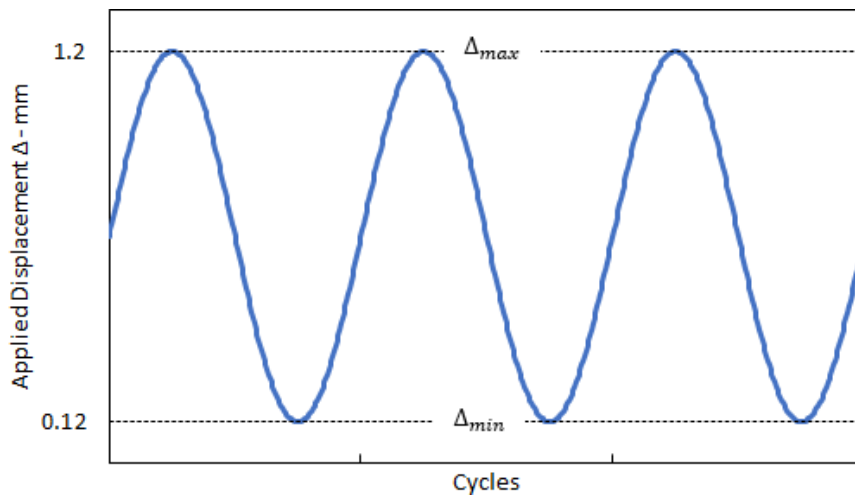


Figure 5-7 Applied Cyclic Displacement

### 5.3 Results and Discussions

The reaction force under this displacement load is plotted for the regular analysis in Figure 5-8. Additionally, the damage conditions at the numbered points indicated in Figure 5-8 are shown in Figure 5-9. The damage state at the one-millionth cycle is presented in the three-dimensional model. However, to provide a clearer view of the damage conditions, subsequent damage states will be illustrated on a cross-section taken from the middle x-y plane of the structure.

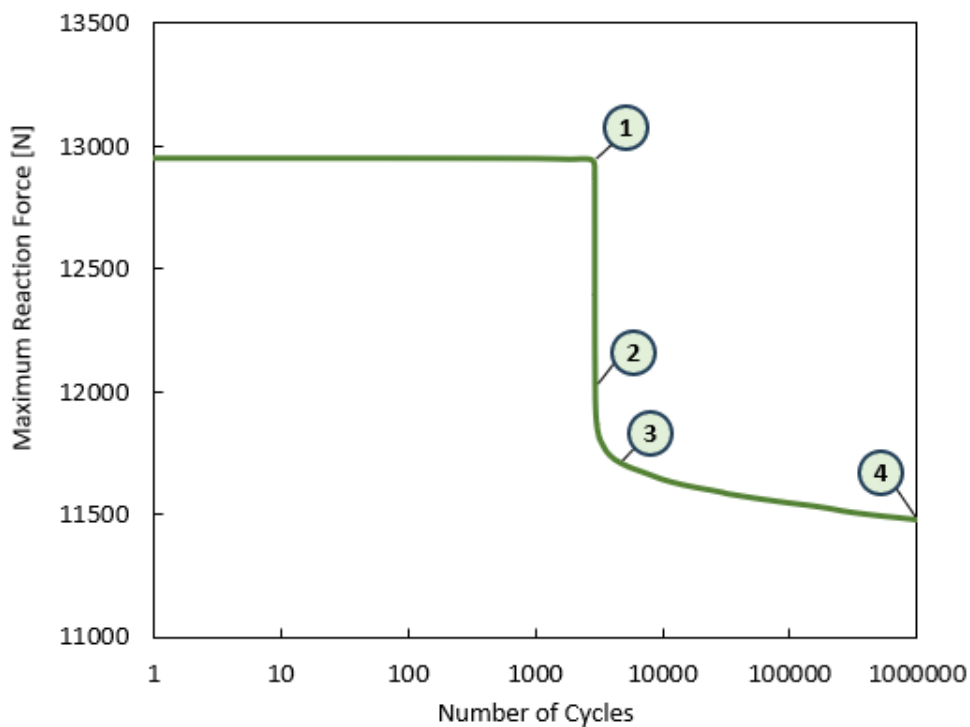


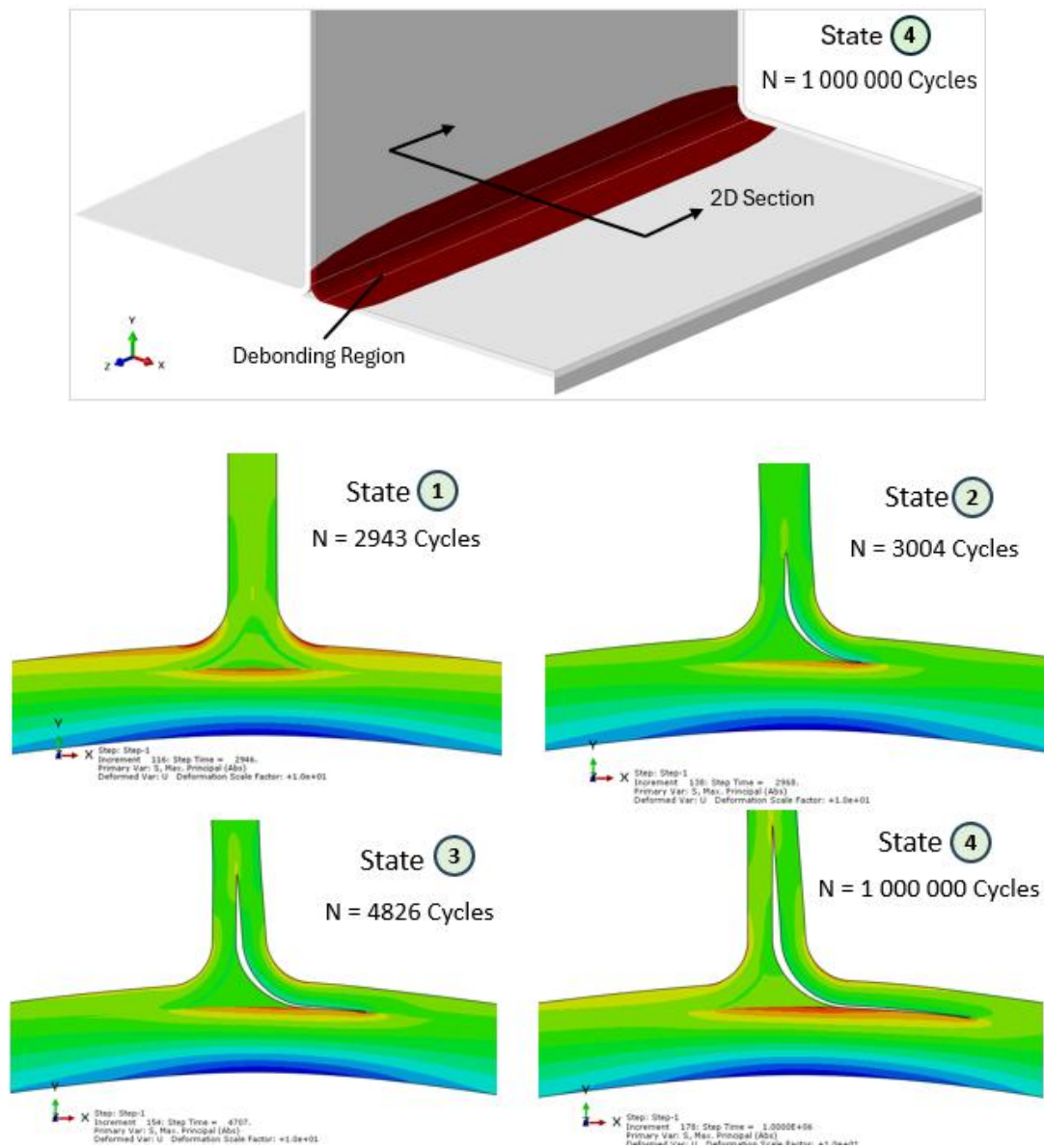
Figure 5-8 Fatigue response of the T-Joint under cyclic displacement load

When examining the damage conditions, the propagation is not symmetric about the midplane of the vertical section of the stringers due to unsymmetric layup directions and unbalanced and unsymmetric stacking sequence of the stiffeners.

It is observed that damage initiates at point (1) and progresses unstably toward the vicinity of point (3). In this region, a complete separation between the noodle and the stringer is observed, along with some damage in the Stringer-Stringer and Skin-Stringer interfaces on the same side. At the intermediate point (2), the progression of

Skin-Stringer debonding, moving to the right, has begun. After point (3), the damage propagates stably until reaching point (4).

The proposed method, which is the focus of this study, is applied in the next stage. In Figure 5-10, the reaction forces calculated using the Global-Local method are plotted alongside those obtained through the regular approach. The damage state at the one-millionth cycle is also presented for the regular and Global-Local analyses. Global-local methodology demonstrates that damage and reaction forces can be accurately predicted.



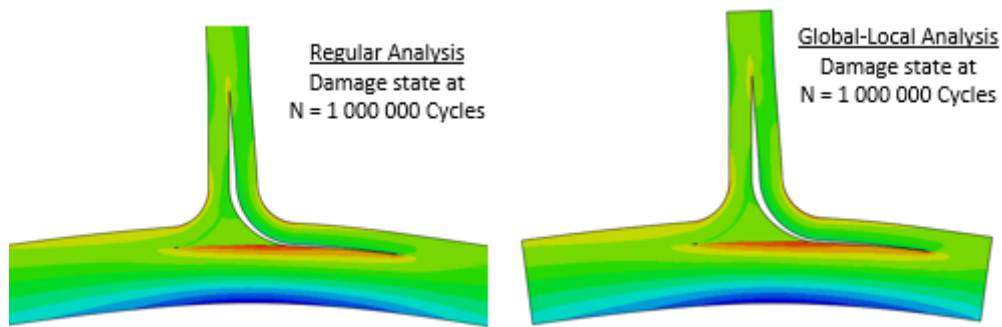
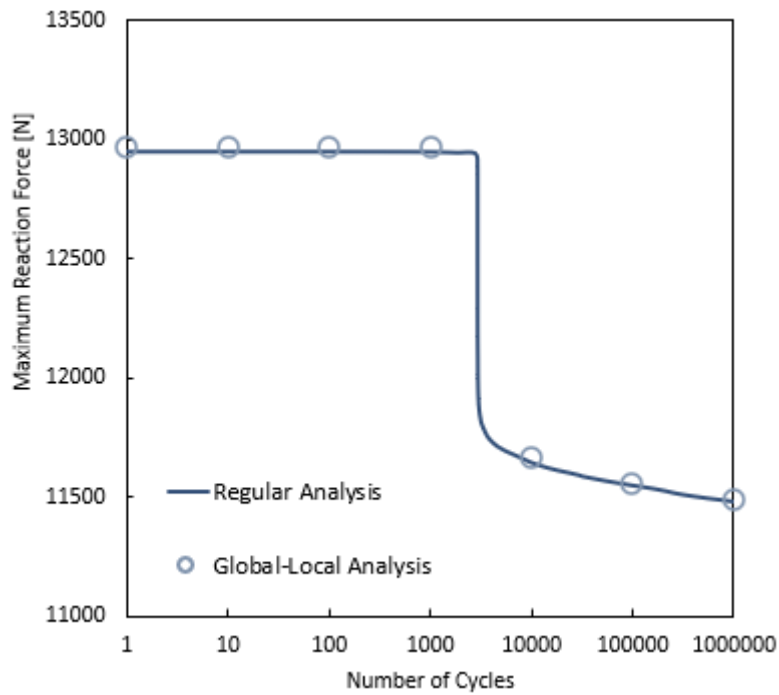


Figure 5-10 Comparison of Fatigue Response of the T-Joint and Damage State at One-Millionth Cycle

Next, the damage magnitudes and reaction forces at the mid-section in the one-millionth cycle will be compared between the Global-Local method and the regular analysis. Two paths have been defined for damage comparison, as shown in Figure 5-11. The first path represents the damage extent between the stringer and the skin, denoted as  $\Delta a_1$ . The second path corresponds to the damage extent between the stringers, represented as  $\Delta a_2$ .

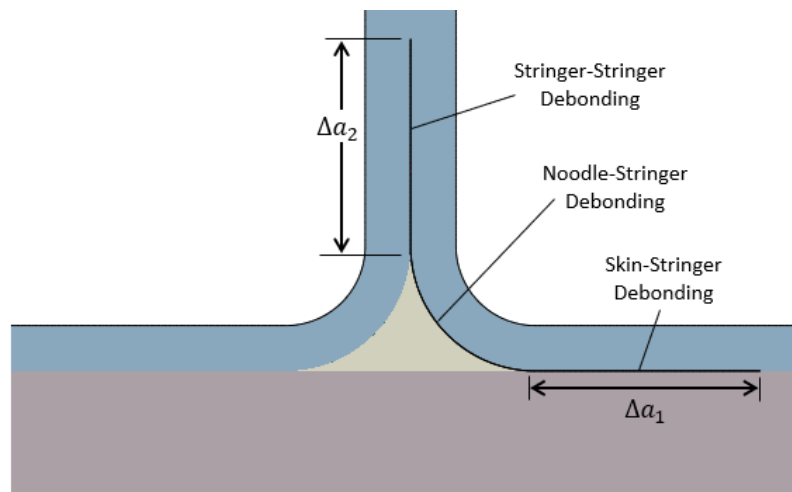


Figure 5-11 Definition Debonding Propagation Paths

Table 5-2 presents the reaction forces and damage propagation lengths calculated at the one-millionth cycle. The difference between the two methods is 0.3% for reaction forces and less than 1.5% for damage extents. As a result, the proposed approach successfully analyses fatigue-induced interlaminar damage in aerospace applications.

Table 5-2. Comparison of Computational Effort Reaction Force and Delamination Extent Results

	Regular Analysis	Global-Local	Difference
Reaction Force	11476 N	11494 N	0.2 %
Stringer-Skin Delamination $\Delta a_1$	15.4 mm	15.2 mm	-1.3 %
Stringer-Stringer Delamination $\Delta a_2$	14.6 mm	14.4 mm	-1.4 %

## 5.4 Conclusions

The method is successfully applied in the T-Joint model under fatigue loading. The results are close to the regular analysis, with a difference below 1.5%.

The validated method's computational advantage, which has been demonstrated in an aerospace application, is discussed. The computation summaries are presented in Table 5-3. The proposed method provides a computational advantage of 40%. Therefore, this method can be utilised in aerospace applications to reduce computational effort in progressive interlaminar damage modelling.

Table 5-3 Comparison of Computational Effort

Regular Analysis	Global-Local	Difference
10120 min	6070 min	-40%

## CHAPTER 6

### CONCLUSIONS AND RECOMMENDATIONS

#### 6.1 General Conclusions

This study aims to develop an accurate and computationally efficient interlaminar damage modelling methodology compatible with fatigue analyses. The general conclusions of this study are summarised:

- None of the studies in the literature cover the global-local method for fatigue analyses. Therefore, a new global-local method is proposed that is compatible with fatigue analyses for assessing interlaminar damage of composite structures.
- The method does not require modification of the simple global model. The application of corrective nodal forces is sufficient for the algorithm. Therefore, this model is efficient in Finite Element Modelling.
- Static and fatigue DCB analyses verify the method by showing consistent results with regular analyses and closed-form solutions.
- In static analyses, the method is applied to Tension-Torsion experiment specimen models. The results are consistent with regular analyses.
- In Tension-Torsion applications, ILSS and fracture toughness selection are critical, as shown in sensitivity studies.
- The method can capture the effect of torsional stiffening due to axial force observed in helicopter rotor blades.
- The method is applied to a T-Joint specimen model under fatigue loading and shows consistent results with the regular analyses.
- In all applications, the computational advantage of the global-local method varies between 32% to 52%. Therefore, this method proves its superior computational efficiency in aerospace applications.

## **6.2 Recommendation for Future Work**

The method is verified by Static Mode-I DCB applications. It can also be verified under Mode-II and Mixed Mode loading with a standardised experimental setup.

Verification in the static analysis includes the static DCB experiments. Fatigue experiments can also be performed to strengthen the fatigue DCB FEM.

This method is applied to solid continuum elements. It can be extended to shell elements, and shell-to-solid global-local coupling formulations can be developed.

## REFERENCES

- [1] M. Akterskaia et al., “Progressive Failure Analysis of Stiffened Composite Panels Using a Two-Way Loose Coupling Approach Including Intralaminar Failure and Debonding”. AIAA/ASME/ASCE/AHS/ASC Structures, Structural Dynamics, and Materials Conference, Kissimmee, Florida, 8–12 January 2018.
- [2] M. A. Minnicino II, D.A. Hopkins, «Overview of Reduction Methods and Their Implementation into Finite-Element Local-to-Global Techniques», Army Research Laboratory Report, ARL-TR-3340, 2003.
- [3] J.D. Whitcomb, «Three-Dimensional Analysis of a Postbuckled Embedded Delamination», *Journal of Composite Materials*, 23(9), 862-889, 1989.
- [4] K.L. Singh, et al.. "Delamination tolerance studies in laminated composite panels." *Sadhana* 25 (2000): 409-422, 2000.
- [5] C. Xing and C. Zhou. "Finite element modeling of crack growth in thin-wall structures by method of combining sub-partition and substructure." *Engineering Fracture Mechanics* 195 (2018): 13-29.
- [6] L. Gendre et al.. "Non-intrusive and exact global/local techniques for structural problems with local plasticity." *Computational Mechanics* 44 (2009): 233-245.
- [7] M. Duval et al., “Non-intrusive Coupling: Recent Advances and Scalable Nonlinear Domain Decomposition”, *Arch. Computat. Methods Eng.* 23:17–38, 2016.
- [8] M. Duval et al., “Local/global non-intrusive parallel coupling for large scale mechanical analysis”. 11th World Congress on Computational Mechanics - 5th European Conference on Computational Mechanics. IACM-ECCOMAS, Barcelona, Spain, June 2014.

- [9] L. Gendre et al., "A two-scale approximation of the Schur complement and its use for non-intrusive coupling", *Int. J. Numer. Meth. Engng.*; 87:889–905, 2011.
- [10] P. Gosselet et al., "Non-invasive global–local coupling as a Schwarz domain decomposition method: acceleration and generalization" *Adv. Model. and Simul. in Eng. Sci.*, 5:4, 2018.
- [11] W. Z. Nie, and W. K. Binienda. "A meso-macro mechanical approach to analyzing triaxially-braided composites with failure subjected to impact." In *Earth and Space 2012: Engineering, Science, Construction, and Operations in Challenging Environments*, pp. 1218-1226. 2012.
- [12] J. Reinoso, et al. "Experimental and three-dimensional global-local finite element analysis of a composite component including degradation process at the interfaces." *Composites Part B: Engineering* 43.4, 1929-1942, 2012.
- [13] E. Oterkus et al. "Combined finite element and peridynamic analyses for predicting failure in a stiffened composite curved panel with a central slot." *Composite Structures* 94.3, 839-850, 2012.
- [14] E. Pietropaoli, and A. Riccio. "A global/local finite element approach for predicting interlaminar and intralaminar damage evolution in composite stiffened panels under compressive load". *Applied Composite Materials*, 18, pp.113-125, 2011.
- [15] E. Oterkus et al.. "Damage growth prediction from loaded composite fastener holes by using peridynamic theory". In *51st AIAA/ASME/ASCE/AHS/ASC Structures, Structural Dynamics, and Materials Conference 18th AIAA/ASME/AHS Adaptive Structures Conference 12th* (p. 3026), April 2010.
- [16] O.R. Shah, M. Tarfaoui, «The identification of structurally sensitive zones subject to failure in a wind turbine blade using nodal displacement based finite element sub-modeling», *Renewable Energy* 87, 168-181, 2016.

- [17] Y. Su, et al. "Mechanical behavior in bending deformation of thermoplastic composite laminates with different stacking sequences." *Journal of Composite Materials* 50.8, 1037-1048, 2016.
- [18] H.L. Liu, et al. "Numerical investigation of macro-and micro-mechanics of a ceramic veneer bonded with various cement thicknesses using the typical and submodeling finite element approaches." *Journal of dentistry* 37.2,141-148, 2009.
- [19] K. Woo, J. D. Whitcomb, «Global/Local Finite Element Analysis for Textile Composites», *Journal of Composite Materials*, vol.28, no. 14, 1994.
- [20] J.D. Whitcomb, and K. Woo, Application of iterative global/local finite-element analysis. Part 1: Linear analysis. *Communications in numerical methods in engineering*, 9(9), pp.745-756, 1993.
- [21] J. D. Whitcomb (1991), "Iterative Global/Local Finite Element Analysis", *Computers & Structures* Vol. 40, No 4, pp. 1027-1031.
- [22] S. Hühne et.al. (2016), "A two-way loose coupling procedure for investigating the buckling and damage behaviour of stiffened composite panels", *Composite Structures* Vol.136, pp. 513-525.
- [23] C.E. Covington, "Composite Structural Applications in Helicopter Rotors". *World Aerospace Technology* 90, March 1990.
- [24] A.A. Işık, "Structural Optimization of Composite Helicopter Rotor Blades". M.S. Thesis, Department of Aerospace Engineering, Middle East Technical University, 2018.
- [25] M. Jimenez, et al., "Estimated S-N curve for nodular cast iron: A steering knuckle case study". *Int.J Automot. Technol.* 15, 1197–1204, 2014
- [26] A. Turon Travesa, "Simulation of Delamination in Composites Under Quasi-static and Fatigue Loading Using Cohesive Zone Models". Ph.D.

Dissertation, Dept. of Mechanical Engineering and Industrial Construction, University of Girona, 2006.

- [27] M. Hoj, et al., “Effect of Stress Ratio on Near-threshold Propagation of Delamination Fatigue Cracks in Unidirectional CFRP”, *Composites Science and Technology* 29, 273-292, 1987.
- [28] L.E. Asp, et al., “Delamination Growth and Thresholds in a Carbon/Epoxy Composite Under Fatigue Loading,” *Journal of Composites Technology & Research, JCTRER*, Vol. 23, No. 2, pp.55–68, 2001.
- [29] L. Gornet, H. Ijaz, “A high-cyclic elastic fatigue damage model for carbon fibre epoxy matrix laminates with different mode mixtures”. *Composites Part B: Engineering, Elsevier*, 42 (5), pp.1173-1180, 2011.
- [30] M. Kenane, M. L. Benzeggagh, “Mixed-Mode Delamination Fracture Toughness of Unidirectional Glass/Epoxy Composites under Fatigue Loading”. *Composites Science and Technology* 57, pp.597-605, 1997.
- [31] F. Pegorin, et al., “Mixed-mode I/II delamination fatigue strengthening of polymer composites using Z-Pins”, *Composites Part B*, 123, pp.219-226, 2017.
- [32] G.B. Murri, “Evaluation of Delamination Onset and Growth Characterization Methods under Mode I Fatigue Loading”. *NASA Report, NASA/TM–2013-217966*, 2013.
- [33] C. Rans, et al., “Misinterpreting the results: How similitude can improve our understanding of fatigue delamination growth”. *Composites Science and Technology* 71, 230– pp.238, 2011.
- [34] N.V. de Carvalho, G.B. Murri, “A Novel Method for Characterizing Fatigue Delamination Growth Under Mode I Using the Double Cantilever Beam Specimen”, *Conference: American Society for Composites Technical Conference; 29th; At: San Diego, CA; United States, September, 2014.*

- [35] S. Maiti, P.H. Geubelle, "A cohesive model for fatigue failure of polymers". *Engineering Fracture Mechanics* 72, pp.691–708, 2005.
- [36] L.R. Gambone, "The Effect of R-Ratio on the Mode II Fatigue Delamination Growth of Unidirectional Carbon/Epoxy Composites", M.S. thesis, Department of Metals and Materials Engineering, University of British Columbia, 1991.
- [37] H. Bansemir, S. Emmerling, "Fatigue Substantiation and Damage Tolerance Evaluation of Fiber Composite Helicopter Components", RTO AVT Specialists' Meeting on "Application of Damage Tolerance Principles for Improved Airworthiness of Rotorcraft", Corfu, Greece, April 1999.
- [38] A.J. Vinciquerra, et al., "Determination of the Mode II Fatigue Delamination Toughness of Laminated Composites". *Journal of Reinforced Plastics and Composites* 21, No. 07/2002, pp.663-677, 2002.
- [39] N. Blanco Villaverde, "Variable mixed-mode delamination in composite laminates under fatigue conditions: testing & analysis". Ph.D. Thesis, Dept. of Mechanical Engineering and Industrial Construction, University of Girona 2004.
- [40] O. Al-Khudairi, et al., "Characterising mode I/mode II fatigue delamination growth in unidirectional fibre reinforced polymer laminates", *Materials and Design* 66, pp. 93–102, 2015.
- [41] G. Androuin, et al., "Characterization of fatigue delamination growth under mode I and II: Effects of load ratio and load history". *Engineering Fracture Mechanics*, 203, pp.172-185, 2018.
- [42] J. Kang, et al., "Fatigue Life Prediction of Composite Laminates Based on Progressive Damage Analysis", *Advanced Materials Research*, 1064, pp 108-114, 2015.
- [43] M. Bizeul, et al., "Influence of woven ply degradation on fatigue crack growth in thin notched composites under tensile loading" *International*

Journal of Fatigue, vol; 32(1), pp. 60-65, 2010.

- [44] B. Vieille, “Fatigue accumulated damage in notched quasi-isotropic composites under high temperature conditions: A discussion on the influence of matrix nature on the stress energy release rate”, *Journal of Composite Materials*, Vol. 52(17), pp.2397–2412, 2018.
- [45] M.H.R. Jen, et al., “Fatigue damage in centrally notched GR/EP laminates”, *Experimental Mechanics* volume 30, pp. 360–366, 1990.
- [46] S. R. Prabhu, Y.J. Lee, “Derivation of Paris’ Law Parameters from S-N Curve Data: a Bayesian Approach”, *The 2017 World Congress on Advances in Structural Engineering and Mechanics (ASEM17)*, Ilsan (Seoul), Korea, 28 August-1 September, 2017.
- [47] D. A. Virkler, et al., “The statistical nature of fatigue crack propagation”, *U.S. Airforce Technical Report, AFFDL-TR-78-43*, 1978.
- [48] L. Dong, et al. “On Improving the Celebrated Paris’ Power Law for Fatigue, by Using Moving Least Squares”, *CMC*, vol.45, no.1, pp.1-15, 2015.
- [49] A.R. Shahani, S. Mohammadi, “Damage tolerance approach for analyzing a helicopter main rotor blade”, *Engineering Failure Analysis*, 57, pp. 56–71, 2015.
- [50] Y. Qiao, et al. “A study on the multi-axial fatigue failure behavior of notched composite laminates”. *Composites Part A*, 127, 105640, 2019.
- [51] S. DorMohammdi, et al., “Damage-tolerant composite design principles for aircraft components under fatigue service loading using multi-scale progressive failure analysis”, *Journal of Composite Materials*, Vol. 51(15) 2181–2202, 2017.
- [52] M.A. Laribi, et al., “Fast fatigue life prediction of short fiber reinforced composites using a new hybrid damage approach: Application to SMC”, *Composites Part B: Engineering* 139, pp.155- 162, 2018.

- [53] C.M. Manjunatha, et al., “The tensile fatigue behaviour of a silica nanoparticle-modified glass fibre reinforced epoxy composite”, *Composites Science Technology*, 70, pp.193-199, 2010.
- [54] Y.Huh, et al.,” Effect of stress ratio on fatigue life of GFRP composites for WT blade”, *Journal of Mechanical Science and Technology*, 26 (7), pp.2117-2120, 2012.
- [55] A. Malpot, et al., “Fatigue behaviour of a thermoplastic composite reinforced with woven glass fibres for automotive application”, 6th Fatigue Design conference, *Fatigue Design 2015, Procedia Engineering* 133, pp. 136 – 147, 2015.
- [56] H.Liu, et al., “Fatigue Modeling for Carbon/epoxy Unidirectional Composites under Various Stress Ratios Considering Size Effects”, *International Journal of Fatigue*, 120, pp. 184-200, 2019.
- [57] P.Mu, et al., “A new S-N curve model of fiber reinforced plastic composite”, *Key Engineering Materials*, Vols. 462-463, pp. 484-488, 2011.
- [58] İ. Burhan, H.S. Kim, “S-N Curve Models for Composite Materials Characterisation: An Evaluative Review”, *J. Compos. Sci*, 2(38), pp.1-29, 2018.
- [59] J. Nakai-Chapman, et al., “Implementation of progressive failure for fatigue based on cycle-dependent material property degradation model”. *Multiscale and Multidiscip. Model. Exp. and Des.*, <https://doi.org/10.1007/s41939-020-00080-4>, (2020).
- [60] J.T. Ryder, F.W. Crossman, “A study of stiffness, residual strength and fatigue life relationships for composite laminates”, *NASA Contract Report CR-172211*,1983
- [61] C. Sola, et al. “Bearing fatigue of composite laminates: Damage monitoring and fatigue life prediction”. *Composites Part B: Engineering*, 110. pp. 487-496, 2017.

- [62] H.T. Han, et al., “The Effect of Loading Parameters on Fatigue of Composite Laminates: Part III”. Report No. DOT/FAA/AR-99/22, U.S. Department of Transportation Federal Aviation Administration, 1999.
- [63] N. Uda, et al., “Compression Fatigue Failure of CFRP Laminates with Impact Damage”, *Composites Science and Technology* 69 (14), pp. 2308-2314, 2009.
- [64] J. Jeandrau, et al., “Fatigue behaviour of adhesive joints”, 6th Fatigue Design conference, Fatigue Design 2015, *Procedia Engineering* 133, pp. 508 – 517, 2015.
- [65] J.A. Pascoe, “Delamination of Bonded Repairs - A Damage Tolerance Approach”, M.S. Thesis, Faculty of Aerospace Engineering, Delft University of Technology, 2012.
- [66] R.C. Alderliesten, “Damage tolerance of bonded aircraft structures”, *International Journal of Fatigue* 31, pp.1024–1030, 2009.
- [67] S. Sihm et al., “Time- and Temperature-Dependent Failures of a Bonded Joint”, Ph.D. Dissertation, Department of Mechanical Engineering, Stanford University, 1997.
- [68] G.B. Murri, et al., “Fatigue Life Methodology for Tapered Composite Flexbeam Laminates”, American Helicopter Society, 53rd Annual Forum, Virginia Beach, Virginia. April 29 - May 1, 1997.
- [69] G.B. Murri, et al., “Fatigue and Damage Tolerance Analysis of a Hybrid Composite Tapered Flexbeam”, American Helicopter Society Forum, Washington D.C., May 9-11, 2001.
- [70] J.F. Mandell, et al., “Effects Structural Details on Delamination and Fatigue Life of Fiberglass Laminates”. *Proceedings of AWASME Wind Energy Symposium*. Reno, NV. p.p. 323- 333., January 1998.

- [71] A. Satyanarayana et al., "Influence of Finite Element Size in Residual Strength Prediction of Composite Structures", 53rd AIAA/ASME/ASCE/AHS/ASC Structures, Structural Dynamics and Materials Conference, 2012.
- [72] F. Chang and Y. Chang, "A Progressive Damage Model for Laminated Composites Containing Stress Concentrations", *Journal of Composite Materials*, 21, pp.834-855, 1987.
- [73] N. Knight, "Factors Influencing Progressive Failure Analysis Predictions for Laminated Composite Structures". 49th AIAA/ASME/ASCE/AHS/ASC Structures, Structural Dynamics, and Materials Conference, Schaumburg, IL, 7 - 10 April 2008.
- [74] D.W. Sleight, "Progressive Failure Analysis Methodology for Laminated Composite Structures". NASA/TP-1999-209107, 1999.
- [75] A.V. Malakhov et al., "Progressive Failure Analysis of Variable Stiffness Composite Structures". AIP Conference Proceedings 2053, 030038, 2018.
- [76] A. Lakshminarayana et al., "Progressive Failure Analysis of Laminated Composite Plates with Elliptical or Circular Cutout Using Finite Element Method". *IOP Conf. Ser.: Mater. Sci. Eng.*, 149 012104, 2016.
- [77] Z.F Chen et al., "A Combined Elastoplastic Damage Model for Progressive Failure Analysis of Composite Materials and Structures". *Composite Structures*. Vol.94, pp.3478-3489, 2012.
- [78] V. Aitharaju et al., "Progressive Damage Modeling of Notched Composites", NASA Report, NF1676L-25017, 2016.
- [79] L. Tsau and R. Plunkett, "Finite Element Analysis of Progressive Failure for Laminated FRP Plates with inplane Loading", *Engineering Fracture Mechanics* Vol. 45, No. 4, pp. 529-546, 1993.

- [80] J. Gu et al., “A Continuum Damage Model for Intralaminar Progressive Failure Analysis of CFRP Laminates Based on the Modified Puck’s Theory”, *Materials*, 12, 3292, 2019.
- [81] K. Kodagali, “Progressive Failure Analysis of Composite Materials using the Puck Failure Criteria”. Ph.D. Dissertation, Department of Mechanical Engineering, University of South Carolina, 2017.
- [82] P. Minguet et al., “Energy-Based Stiffness Degradation for Alleviation of Mesh Sensitivity for Progressive Failure Analysis of Center-Notched Composite Panels”. 53rd AIAA/ASME/ASCE/AHS/ASC Structures, Structural Dynamics and Materials Conference, Honolulu, Hawaii, 23 - 26 April 2012.
- [83] J. Zhang et al., “A Progressive Damage Analysis Based Characteristic Length Method for Multi-Bolt Composite Joints”. *Composite Structures*. Vol.108, pp.915-923, 2014.
- [84] A. Riccio et al., “Intra-Laminar Progressive Failure Analysis of Composite Laminates with a Large Notch Damage”. *Engineering Failure Analysis*, Vol.73, pp.97-112, 2016.
- [85] A.P.K. Joseph et al., “Open Hole and Filled Hole Progressive Damage and Failure Analysis of Composite Laminates with a Countersunk Hole”, *Composite Structures*, Vol.203, pp.523-538, 2018.
- [86] A. Satyanarayana, A. Przekop, “Predicting Failure Progression and Failure Loads in Composite Open-Hole Tension Coupons”, NASA Report, NASA/CR–2010-216700, 2010.
- [87] V.K. Goyal et al., “Intralaminar and Interlaminar Progressive Failure Analyses of Composite Panels with Circular Cutouts.” *Composite Structures*, Vol.64, pp.91–105, 2004.

- [88] F. Bianchi, X. Zhang, “A Cohesive Zone Model for Predicting Delamination Suppression In Z-Pinned Laminates”. *Composites Science and Technology*, Vol.71, pp.1898-1907, 2011.
- [89] P.F. Liu et al., “A Nonlocal Finite Element Model for Progressive Failure Analysis of Composite Laminates”. *Composites: Part B*, Vol.86, pp.178–196, 2016.
- [90] H.Bao, G.Liu, “Progressive Failure Analysis on Scaled Open-Hole Tensile Composite Laminates”. *Composite Structures*, Vol.150, pp.173-180, 2016.
- [91] Q. Shen et al., “Progressive Failure Analysis of Scarf-Repaired Composite Laminate Based on Damage Constitutive Model”. *Proceedings of the Institution of Mechanical Engineers, Part L: Journal of Materials: Design and Applications*, Vol.233(2), pp.180-188, 2016.
- [92] Y. Nikishkov, et al., “Progressive fatigue damage simulation method for composites”, *International Journal of Fatigue* 48, 266–279, 2013.
- [93] K.C. Warren et al., “Progressive Failure Analysis of Three-Dimensional Woven Carbon Composites in Single-Bolt, Double-Shear Bearing”. *Composites Part B: Engineering*, Vol. 84, pp.266-276, 2016.
- [94] J.M. Hundley, et al., “Three-Dimensional Progressive Failure Analysis of Bolted Titanium-Graphite Fiber Metal Laminate Joints”. *Journal of Composite Materials*, Vol.45(7), pp.751-769, 2010.
- [95] R. Ganesan, D. Zhang, “Progressive Failure Analysis of Composite Laminates Subjected to In-Plane Compressive and Shear Loadings”. *Science and Engineering of Composite Materials*, Vol.11(2-3), pp.79–102, 2004.
- [96] A.M. Gadade et al., “Progressive Failure Analysis of Laminated Composite Plate by Using Higher Order Shear Deformation Theory.” *Applied Mechanics and Materials*, Vol. 592-594, pp.1151-1154, 2014.

- [97] R. Ganesan, D.Y. Liu, “Progressive failure and post-buckling response of tapered composite plates under uni-axial compression”. *Composite Structures*. Vol.82, pp.159-176, 2008.
- [98] S.G. Joo, C.S. Hong, “Progressive Failure Analysis of Composite Laminates using 3-D Finite Element Method”. *Key Engineering Materials*, Vol. 183-187, pp.535-540, 2000.
- [99] O. Çelik, L.Parnas, “Maximization of Ultimate Strength of Unidirectional Tapered Composite Structures Considering Different Failure Modes”. 58th AIAA/ASCE/AHS/ASC Structures, Structural Dynamics, and Materials Conference, Grapevine, Texas, 9-13 January 2017.
- [100] S.M. Spottswood, A.N. Palazotto, “Progressive Failure Analysis of a Composite Shell”. *Composite Structures*, Vol.53, pp.117–131, 2001.
- [101] D. Ranz et al., “A Cohesive Zone Model Approach to Interlaminar Behaviour of Carbon/Epoxy Laminated Curved Beams”. *Composite Structures*. Vol.238-11983, 2020.
- [102] V.H. Truong et al., “Failure load analysis of C-shaped composite beams using a cohesive zone model”. *Composite Structures*. Vol.184, pp.581-590, 2018.
- [103] A. Pirondi, G. Nicoletto, «Fatigue crack growth in bonded DCB specimens», *Engineering Fracture Mechanics*, 71, 859–871, 2004.
- [104] B. Gözlüklü, “Delamination Analysis By Using Cohesive Interface Elements In Laminated Composites”. M.S. Thesis, Department of Aerospace Engineering, Middle East Technical University, 2009.
- [105] A. Turon et al., “An Engineering Solution for Mesh Size Effects in The Simulation of Delamination Using Cohesive Zone Models”. *Engineering Fracture Mechanics*, Vol.74, pp.1665-1682, 2007.
- [106] C. Fan et al., “Cohesive Zone with Continuum Damage Properties for Simulation of Delamination Development in Fibre Composites and Failure

- of Adhesive Joints”. *Engineering Fracture Mechanics*, Vol.75, pp.3866–3880, 2008.
- [107] N. Valoroso, et al., “Identification of mode-I cohesive parameters for bonded interfaces based on DCB test”, *Engineering Fracture Mechanics* 104, 56–79, 2013.
- [108] P. Harper and S.R. Hallett, “Cohesive zone length in numerical simulations of composite delamination”, *Engineering Fracture Mechanics*, 75(16), pp.4774-4792, 2008.
- [109] P. Naghipour, et al., “Effect of fiber angle orientation and stacking sequence on mixed mode fracture toughness of carbon fiber reinforced plastics: Numerical and experimental investigations”, *Mater. Sci. Eng. A*, doi:10.1016/j.msea.2009.07.069, 2009.
- [110] P.W. Harper, et al. “A study on the influence of cohesive zone interface element strength parameters on mixed mode behaviour”, *Composites: Part A*, Vol.43, pp.722-834, 2012.
- [111] M. Li et al. “Progressive Failure Analysis of Marine Sandwich Joints with a Modified Material Degradation Model”. *Journal of Reinforced Plastics and Composites*, Vol. 38(9), pp.426–438, 2019.
- [112] A. Sane et al., “Progressive Failure Evaluation of Composite Skin-Stiffener Joints Using Node to Surface Interactions and CZM”. *CMES*, Vol.115(2), pp.281-294, 2018.
- [113] L. Wang et.al., “Continuum Damage Modeling and Progressive Failure Analysis of Carbon Fiber/Epoxy Composite Pressure Vessel”. *Composite Structures*, Vol.134, pp.475–482, 2015.
- [114] X. Chen et.al., “Understanding Progressive Failure Mechanisms of a Wind Turbine Blade Trailing Edge Section Through Subcomponent Tests and Nonlinear FE Analysis”. *Composite Structures*, Vol.214, pp.428–439, 2019.

- [115] K.R. Prashanth, C. Venkatesan. Damage “Assessment of Composite Main Rotor Blade by Finite Element Simulation and Experiment.” European Rotorcraft Forum 2016, Lille, France, 5-8 September 2016.
- [116] E.F. Rybicki, M.F. Kanninen, “A finite element calculation of stress intensity factors by a modified crack closure integral”, *Engineering Fracture Mechanics*, 9, 931–938, 1977.
- [117] I.S. Raju, “Calculation of strain-energy release rates with higher order and singular finite elements”. *Engineering Fracture Mechanics*, 38(3), 251–274, 1987.
- [118] R. Krueger, “The virtual crack closure technique: history, approach and applications”, NASA/CR-2002-211628, 2002.
- [119] G. Barenblatt, “The mathematical theory of equilibrium cracks in brittle fracture”, *Advances in Applied Mechanics*, 7, 55–129, 1962.
- [120] D.S. Dugdale, “Yielding of steel sheets containing slits.” *Journal of the Mechanics and Physics of Solids*, 8, 100–104, 1960.
- [121] A. Needleman, “A continuum model for void nucleation by inclusion debonding”, *Journal of Applied Mechanics*, 54, 525–532, 1987.
- [122] Simulia, “About submodeling”, *Abaqus Documentation Guide*, <https://abaqus-docs.mit.edu/2017/English/SIMACAEANLRefMap/simaanl-c-submodeloverview.htm> , Retrieved: 30 June 2021
- [123] Simulia, “Using substructures”, *Abaqus Documentation Guide*, <https://abaqus-docs.mit.edu/2017/English/SIMACAEANLRefMap/simaanl-c-superelements.htm>, Retrieved: 30 June 2021

- [124] Paz, Mario, and William Leigh. "Integrated matrix analysis of structures: theory and computation." Springer Science & Business Media, 2012.
- [125] M. Akterskaia et al. "Progressive delamination analysis through two-way global-local coupling approach preserving energy dissipation for single-mode and mixed-mode loading." *Composite Structures* 223, 110892, 2019.
- [126] Simulia, Abaqus Documentation, Retrieved: 29 May 2022, <https://abaqus-docs.mit.edu/2017/English/SIMACAEEXCRefMap/simaexc-c-docproc.htm>
- [127] ASTM International, "ASTM D5528-13: Standard Test Method for Mode I Interlaminar Fracture Toughness of Unidirectional Fiber-Reinforced Polymer Matrix Composites", Standard by ASTM International, 2013.
- [128] ASTM International, "ASTM D6115-97(2019): Standard Test Method for Mode I Fatigue Delamination Growth Onset of Unidirectional Fiber-Reinforced Polymer Matrix Composites", Standard by ASTM International, 2019.
- [129] K. E. Oughstun, "Electromagnetic and Optical Pulse Propagation", Springer Series in Optical Sciences 224, <https://doi.org/10.1007/978-3-030-20835-6>, 2019.
- [130] Z. Liu et.al., "Global-local fatigue assessment of an ancient riveted metallic bridge based on submodelling of the critical detail", *Fatigue Fract Eng Mater Struct*, 42 (2), pp. 546-560, 2019.
- [131] M. Giglio, "FEM submodelling fatigue analysis of a complex helicopter component", *International Journal of Fatigue* 21, 445–455, 1999.
- [132] J. M. Romera et al., "Application of the submodeling technique to the analysis of the edge effects of composite laminates", *Journal of Reinforced Plastics and Composites* 32(15) 1099–1111, 2013.

- [133] M.Cho, W.B. Kim, “A Coupled Finite Element Analysis of Independently Modeled Substructures by Penalty Frame Method”, *KSME International Journal*, Vol. 16 No. 10, pp. 1201-1210, 2002.
- [134] R. Borelli et al., “Kinematic Approach for A Global-local Coupling: Compressive Behaviour Of A Delaminated Panel”. *Advanced Composites Letters*, Vol. 20, Iss. 6, pp.150-156, 2011.
- [135] J.W. Bae et al., “Three Dimensional Fretting Wear Analysis by Finite Element Substructure Method”, *International Journal Of Precision Engineering And Manufacturing*, Vol. 10, No. 4, pp. 63-69, 2009.
- [136] T.L. Hsiao, “A Global-local Finite Element for General Composite Structure”, *Computers & Structures*, Vol.40, Iss. 3, 1991, pp. 719-730. 1991.
- [137] A.T. Diamantoudis, G.N. Labeas, “Stress intensity factors of semi-elliptical surface cracks in pressure vessels by global-local finite element methodology”, *Engineering Fracture Mechanics* 72, 1299–1312, 2005.
- [138] M. Ferraiuolo et al., “Global/local finite element analyses supporting the design of a ceramic matrix composite wing leading edge of a re-entry vehicle”, *Materials Today: Proceedings* 34, 31–35, 2021.
- [139] Budynas and J. K. Nisbett, "Shigley's Mechanical Engineering Design, 11th edition," McGraw-Hill, Jan 2019.
- [140] M.A. Biot. “Increase of torsional stiffness of a prismatical bar due to axial tension”, *Journal of Applied Physics*, American Institute of Physics, 1939, 10 (12), pp.860-864, 1939.
- [141] J.K. Sen, “The Influence of Tension Loads on Laminates under Torsion”, *Journal of American Helicopter Society*, 40(4), 71-78, 1995.

- [142] E. Smeets, “Development of a Fatigue Analysis Tool Using Cohesive Zone Modelling for Composite Specimens”, M.Sc. Thesis, Delft University of Technology, Faculty of Aerospace Engineering, 2019.
- [143] X. Ma et al., “Numerical and Experimental Investigation of the interface properties and failure strength of CFRP T-Stiffeners subjected to pull-off load”, *Materials & Design*, 185, 108231, 2020.



## APPENDICES

### A. Derivation of the Exact formulation of the DCB response

The exact solution of the DCB is calculated by SERR expression in Eq.(A-1).

$$G_I = \frac{P^2(a + \chi h)^2}{D} \quad (\text{A-1})$$

The parameter “ $\chi h$ ” is the crack correction parameter. SERR should be expressed as a function of separation input instead of reaction force for displacement-controlled loading. Reaction force expression is given in Eq.(A-2) with the cantilever beam formula.

$$P = \frac{3D\delta}{2(a + \chi h)^3} \quad (\text{A-2})$$

By combining Eq.(A-1) and (A-2), SERR becomes the expression shown in Eq.(A-3).

$$G_I = \frac{9D\delta^2}{4(a + \chi h)^4} \quad (\text{A-3})$$

If  $G_I < G_{IC}$ , there is no crack propagation and  $a = a_0$  for Eq.(A-1) to (A-3). Otherwise, the new crack length should be calculated so that  $G_I = G_{IC}$  substituted in Eq.(A-3). Then, the exact solution for the propagated crack length is expressed in Eq.(A-4).

$$a + \chi h = \sqrt[4]{\frac{9D\delta^2}{4G_{IC}}} \quad (\text{A-4})$$

The corresponding displacement at the start of crack propagation can be determined by substituting  $G_I = G_{IC}$  and  $a = a_0$  in Eq.(A-3).

$$\delta_{cr} = \frac{2}{3} \sqrt{\frac{G_{IC}}{D}} (a_0 + \chi h)^2 \quad (\text{A-5})$$

The new crack length can be substituted into previous equations. In summary, the arm reaction-arm separation response is explicitly shown in Eq. (A-6). Moreover, the crack length response is given in Eq.(A-7). Where  $\delta_{cr}$  is shown in Eq.(A-5).

$$P = \begin{cases} \frac{3D\delta}{2(a_0 + \chi h)^3} & , \delta \leq \delta_{cr} \\ \sqrt[4]{\frac{4DG_{IC}^3}{9\delta^2}} & , \delta > \delta_{cr} \end{cases} \quad (\text{A-6})$$

$$a = \begin{cases} a_0 & , \delta \leq \delta_{cr} \\ \sqrt[4]{\frac{9D\delta^2}{4G_{IC}}} - \chi h & , \delta > \delta_{cr} \end{cases} \quad (\text{A-7})$$

## B. Derivation of Global and Local Region Expressions of the Analytical DCB Model

### Determination of Local Boundary Conditions from the Global Model

According to Figure 3-7, the beam deflection and slope formula of the DCB are given in Eq.(B-1) and Eq.(B-2) respectively [139]. A Minus sign is introduced in front of the slope expression, since by increasing  $x$ , deflection decreases due to the selection of the coordinate system. In the formulations, only the upper half of the beam is considered. Flexural rigidity  $EI$  is replaced by  $D$  for composites, and forces and moments are per unit width.

$$w(x) = \frac{P}{6D} (a - x)^2 (2a + x) \quad (\text{B-1})$$

$$\theta(x) = -w'(x) = \frac{P}{2D} (a^2 - x^2) \quad (\text{B-2})$$

Tip deflection ( $x=0$ ) of the upper beam is the half of the arm separation. Substituting  $x=0$  to Eq.(B-1) gives half separation as shown in Eq.(B-3).

$$\frac{\delta}{2} = \frac{Pa^3}{3D} \quad (\text{B-3})$$

Eliminating  $P/D$  from Eq.(B-1) and (B-2) by using Eq.(B-3) gives beam deflection formulae in terms of input separation as shown in Eq.(B-4) and (B-5).

$$w(x) = \frac{\delta}{4} \left(1 - \frac{x}{a}\right)^2 \left(2 + \frac{x}{a}\right) \quad (\text{B-4})$$

$$\theta(x) = \frac{3\delta}{4a} \left(1 - \frac{x^2}{a^2}\right) \quad (\text{B-5})$$

Local boundary conditions can be determined by substituting  $x=l$  to Eq.(B-4) and (B-5) as shown in Eq.(B-6) and (B-7).

$$w_l = \frac{\delta}{4} \left(1 - \frac{l}{a}\right)^2 \left(2 + \frac{l}{a}\right) \quad (\text{B-6})$$

$$\theta_l = \frac{3\delta}{4a} \left(1 - \frac{l^2}{a^2}\right) \quad (\text{B-7})$$

### Determination of the New Crack Length from the Local Model Solution

SERR is calculated by differentiation of strain energy of the local region as shown by Eq.(B-8).

$$G_I = \frac{\partial U}{\partial a} \quad (\text{B-8})$$

The strain energy of the local region is given in Eq.(B-9). As there are two beams, the strain energy expression of the upper beam is multiplied by 2.

$$U = 2 \int_l^a \frac{[M(x)]^2}{2D} dx \quad (\text{B-9})$$

Moment distribution is given in Eq. (B-10). Where  $P_l$  and  $M_l$  are reaction transverse force and bending moment of the upper beam at  $x=l$  respectively.

$$M(x) = M_l + P_l(x - l) \quad (\text{B-10})$$

By using Eq.(B-9) and (B-10), SERR expression given in (B-8) becomes Eq.(B-11).

$$G_I = \frac{\partial}{\partial a} \left\{ \frac{[M_l + P_l(a - l)]^3 - M_l^3}{3P_l D} \right\} \quad (\text{B-11})$$

$M_l, P_l$  are dependent on the crack length and inputs of  $w_l$  and  $\theta_l$ . In that case, evaluation of Eq.(B-11) is complicated. Instead, by using the path independency property of SERR,  $M_l$  and  $P_l$  are taken, as if they were inputs. For constant  $M_l$  and  $P_l$ , SERR expression is evaluated in (B-12).

$$G_I = \frac{[M_l + P_l(a - l)]^2}{D} \quad (\text{B-12})$$

However,  $M_l, P_l$  are not known. They should be calculated from the deflection of the local region in terms of  $w_l$  and  $\theta_l$ .

The deflection and slope of the upper beam in the local region are expressed in Eq.(B-13) and (B-14).

$$w(x) = \frac{P_l}{6D}(a-x)^2(2a+x-3l) + \frac{M_l}{2D}(a-x)^2 \quad (\text{B-13})$$

$$\theta(x) = -w'(x) = \frac{P_l}{2D}(a+x-2l)(a-x) + \frac{M_l}{D}(a-x) \quad (\text{B-14})$$

By substituting  $x=l$ ,  $w_l$  and  $\theta_l$  can be expressed in terms of  $P_l$  and  $M_l$  as shown in Eq.(B-15) and (B-16).

$$w_l = \frac{P_l}{3D}(a-l)^3 + \frac{M_l}{2D}(a-l)^2 \quad (\text{B-15})$$

$$\theta_l = \frac{P_l}{2D}(a-l)^2 + \frac{M_l}{D}(a-l) \quad (\text{B-16})$$

By solving Eq.(B-15) and (B-16) simultaneously gives Eq.(B-17) and (B-18) which gives  $P_l$  and  $M_l$  in terms of  $w_l$  and  $\theta_l$ .

$$P_l = D \left[ \frac{12w_l}{(a-l)^3} - \frac{6\theta_l}{(a-l)^2} \right] \quad (\text{B-17})$$

$$M_l = D \left[ \frac{4\theta_l}{(a-l)} - \frac{6w_l}{(a-l)^2} \right] \quad (\text{B-18})$$

Substituting Eq.(B-17) and (B-18) into Eq.(B-12) gives SERR expression in terms of local boundary conditions as shown in Eq.(B-19).

$$G_I = D \left[ \frac{6w_l}{(a-l)^2} - \frac{2\theta_l}{(a-l)} \right]^2 \quad (\text{B-19})$$

The value of  $G_I$  must be greater than critical SERR  $G_{IC}$ . Otherwise, the crack does not propagate, and the response is elastic. For  $G_I > G_{IC}$ , crack length should be corrected so that  $G_I = G_{IC}$ . Then by using Eq.(B-19) with  $G_I = G_{IC}$  and  $a = a_{new}$  gives a quadratic equation in terms of new crack length as shown in Eq.(B-20).

$$\sqrt{DG_{IC}}(a_{new} - l)^2 + 2D\theta_l(a_{new} - l) - 6Dw_l = 0 \quad (\text{B-20})$$

The real and positive root of the new crack length is given in Eq.(B-21).

$$a_{new} = l + \frac{D\theta_l + \sqrt{D^2\theta_l^2 + 6w_l\sqrt{D^3G_{IC}}}}{\sqrt{DG_{IC}}} \quad (\text{B-21})$$

Then this crack length is the new crack for the global model for the next iteration (i.e  $a_{new} \leftarrow a$ ).

### C. Supplementary Plots of Static DCB Response for Different Selection of Mesh Sizing at the Vicinity of Damage Region

#### Solutions without Mesh Regularisation

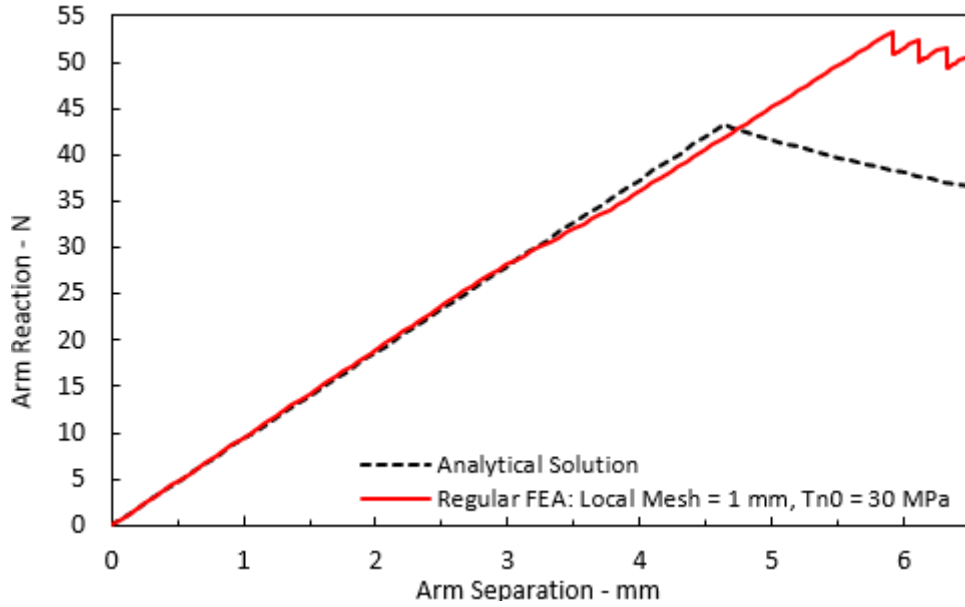


Figure C-1 Static Response of the DCB Model with Local Mesh Size Selection of 1 mm without Mesh Regularisation

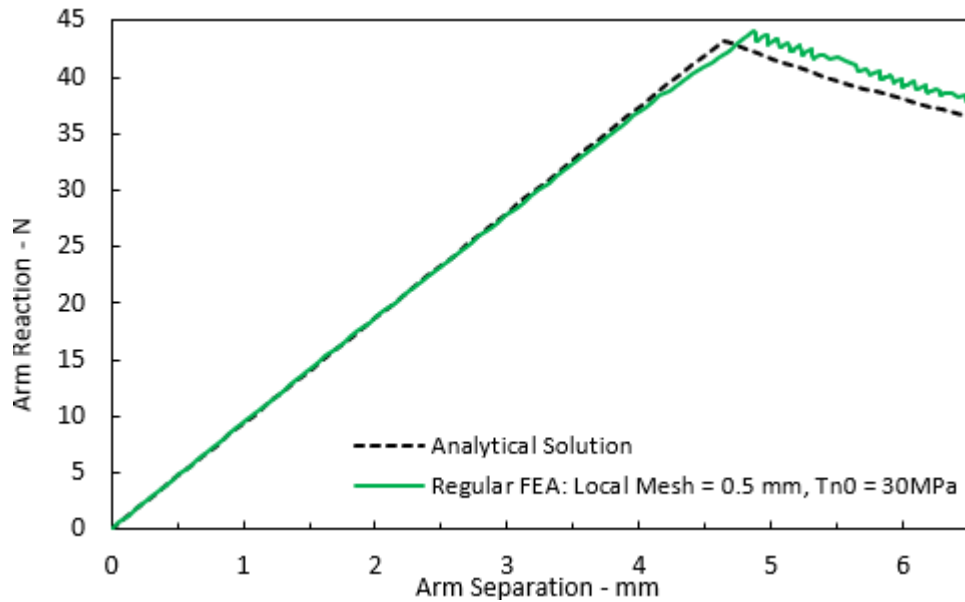


Figure C-2 Static Response of the DCB Model with Local Mesh Size Selection of 0.5 mm without Mesh Regularisation

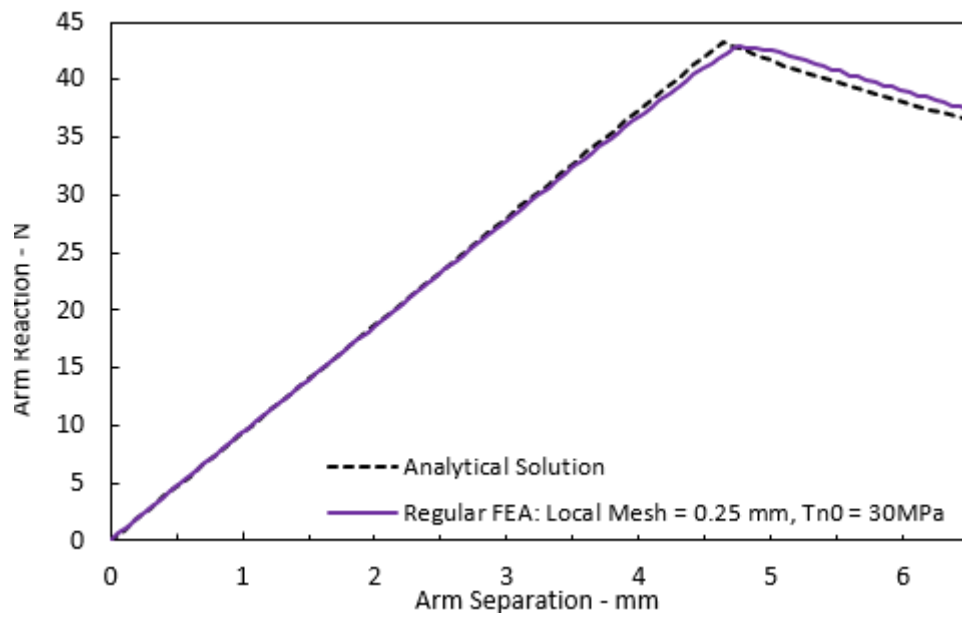


Figure C-3 Static Response of the DCB Model with Local Mesh Size Selection of 0.25 mm without Mesh Regularisation

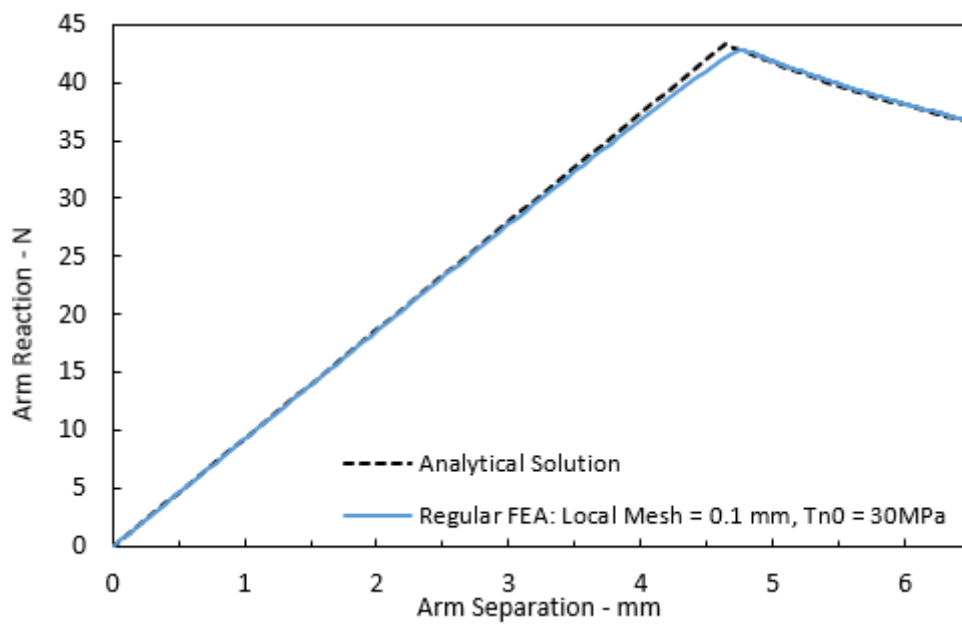


Figure C-4 Static Response of the DCB Model with Local Mesh Size Selection of 0.1 mm without Mesh Regularisation

### Solutions with Mesh Regularisation

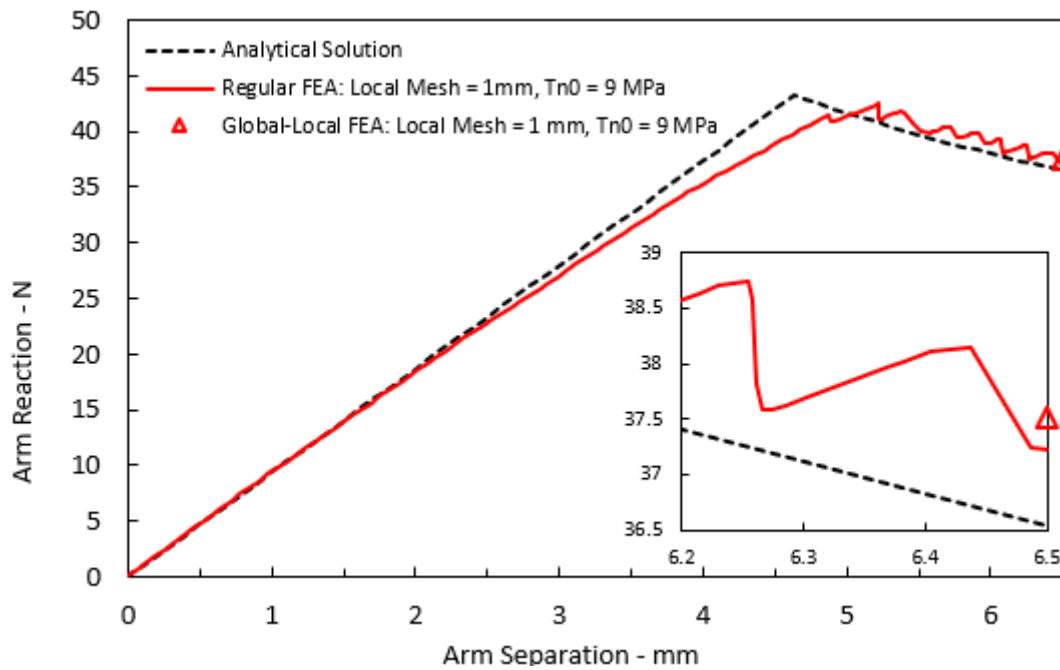


Figure C-5 Static Response of the DCB Model with Local Mesh Size Selection of 1 mm with Mesh Regularisation

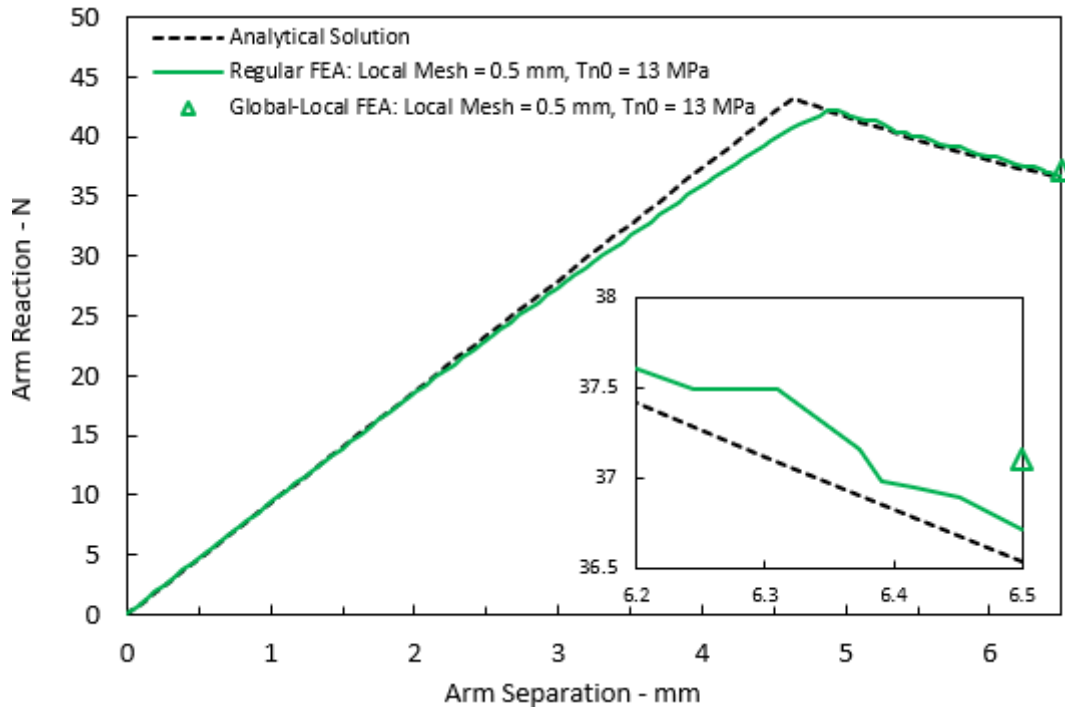


Figure C-6 Static Response of the DCB Model with Local Mesh Size Selection of 0.5 mm with Mesh Regularisation

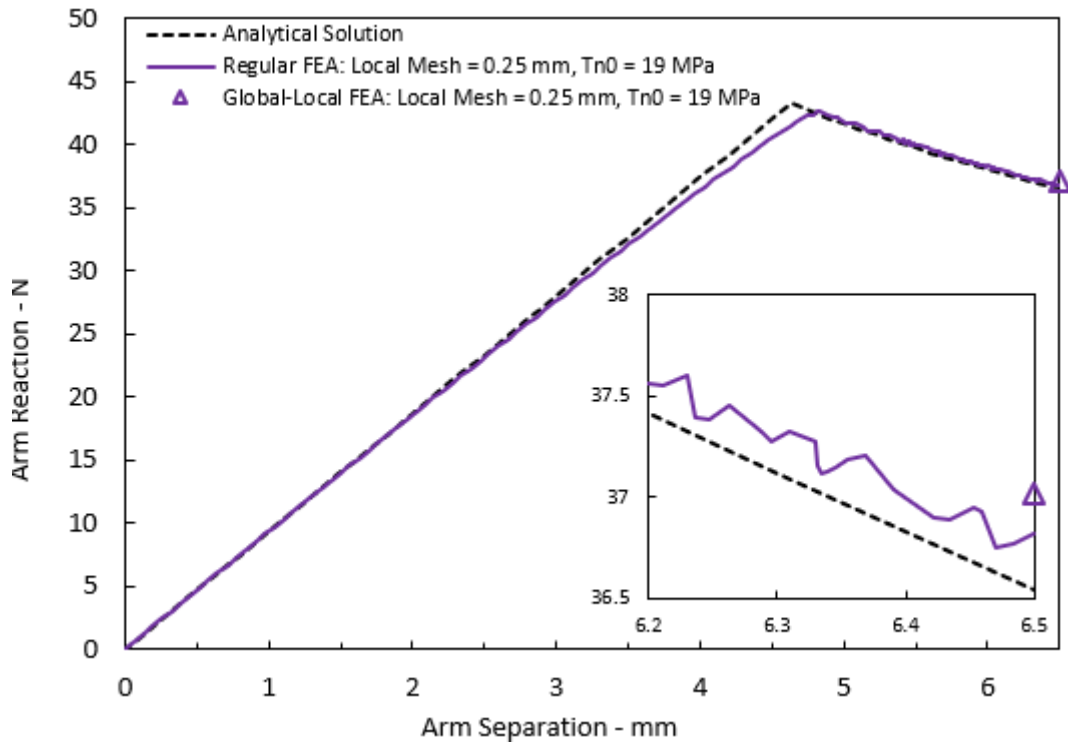


Figure C-7 Static Response of the DCB Model with Local Mesh Size Selection of 0.25 mm with Mesh Regularisation

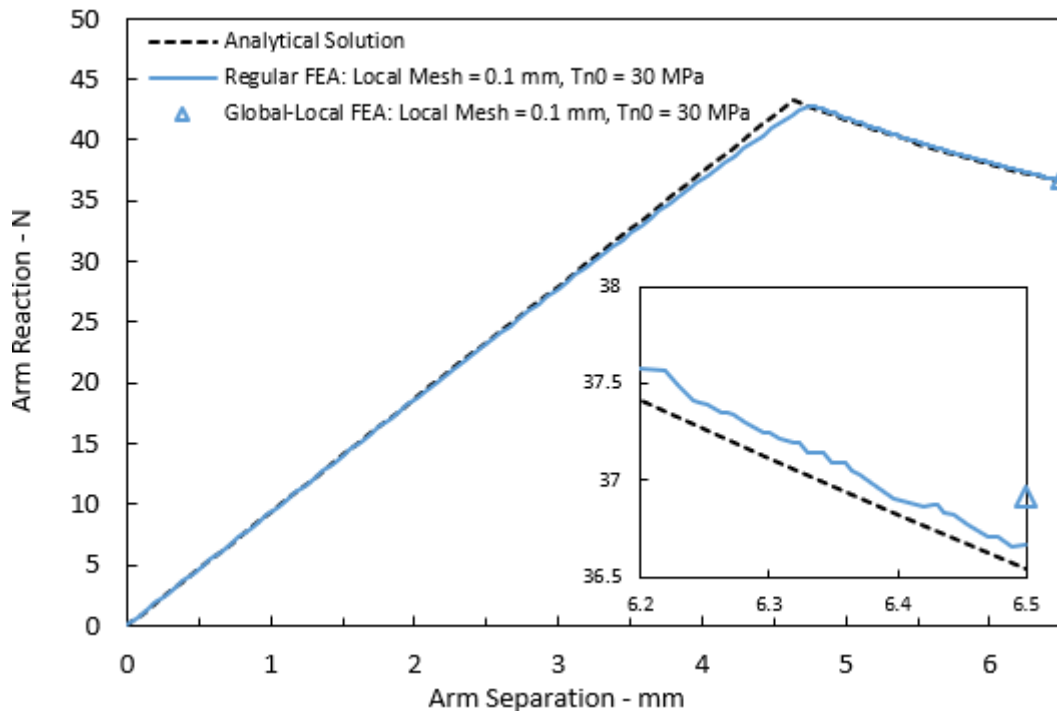


Figure C-8 Static Response of the DCB Model with Local Mesh Size Selection of 0.25 mm with Mesh Regularisation

## D. Derivation of Fatigue Response of the DCB Model

Similar to static loading, maximum SERR and arm reaction expressions are given in Eq.(D-1) and (D-2).

$$G_{max} = \frac{P_{max}^2(a + \chi h)^2}{D} \quad (D-1)$$

$$P_{max} = \frac{3D\delta_{max}}{2(a + \chi h)^3} \quad (D-2)$$

On the other hand, the Paris Law equation is given by Eq.(D-3).

$$\frac{da}{dN} = C(\Delta G)^m, \quad G_{th} < G_{max} < G_C \quad (C-3)$$

And  $\Delta G$  is given by Eq.(D-4).

$$\Delta G = G_{max} - G_{min} = (1 - R^2)G_{max} \quad (D-4)$$

By combining Eq.(D-1), (D-2) and (D-4),  $\Delta G$  is represented in terms of input arm separation in Eq. (D-5).

$$\Delta G = (1 - R^2) \frac{9D\delta_{max}^2}{4(a + \chi h)^4} \quad (D-5)$$

Substituting Eq.(D-5) into (D-3) give separable differential equation as shown in Eq.(D-6).

$$\frac{da}{dN} = C \left[ (1 - R^2) \frac{9D\delta_{max}^2}{4(a + \chi h)^4} \right]^m, \quad G_{th} < G_{max} < G_C \quad (D-6)$$

Separating variables gives Eq.(D-7).

$$\int_{a_0}^a (\bar{a} + \chi h)^{4m} d\bar{a} = C \left[ (1 - R^2) \frac{9D\delta_{max}^2}{4} \right]^m \int_0^N d\bar{N}, \quad (D-7)$$

Evaluation of the integrals gives Eq.(D-8).

$$\frac{(a + \chi h)^{4m+1} - (a_0 + \chi h)^{4m+1}}{4m + 1} = C \left[ (1 - R^2) \frac{9D\delta_{max}^2}{4} \right]^m N \quad (D-8)$$

Arranging Eq.(D-8) gives crack length extent as a function of number of cycles N for displacement-controlled input.

$$a + \chi h = \left\{ (a_0 + \chi h)^{4m+1} + (4m + 1)C \left[ (1 - R^2) \frac{9D\delta_{max}^2}{4} \right]^m N \right\}^{\frac{1}{4m+1}} \quad (D-9)$$

### E. Supplementary Plots of Fatigue DCB Response for Different Selection of Mesh Sizing at the Vicinity of Damage Region

#### Solutions without Mesh Regularisation

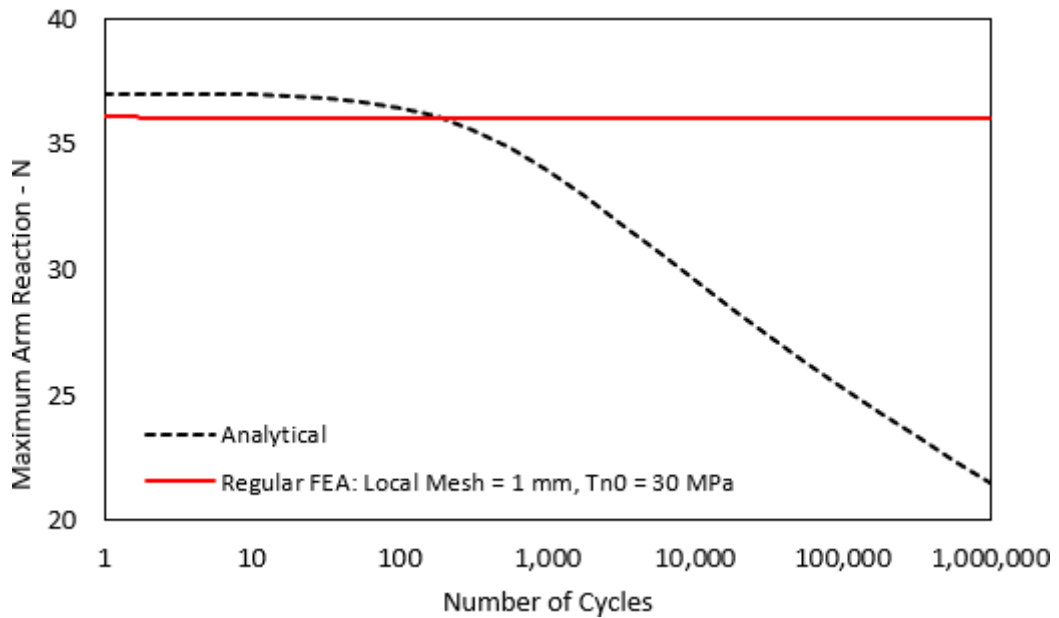


Figure E-1 Fatigue Response of the DCB Model with Local Mesh Size Selection of 1 mm without Mesh Regularisation

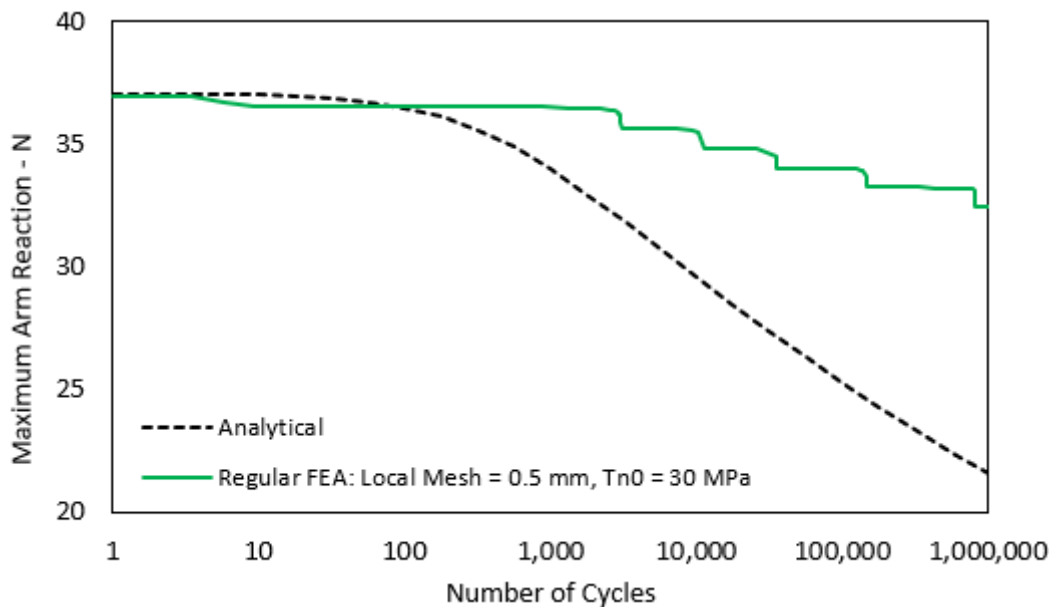


Figure E-2 Fatigue Response of the DCB Model with Local Mesh Size Selection of 0.5 mm without Mesh Regularisation

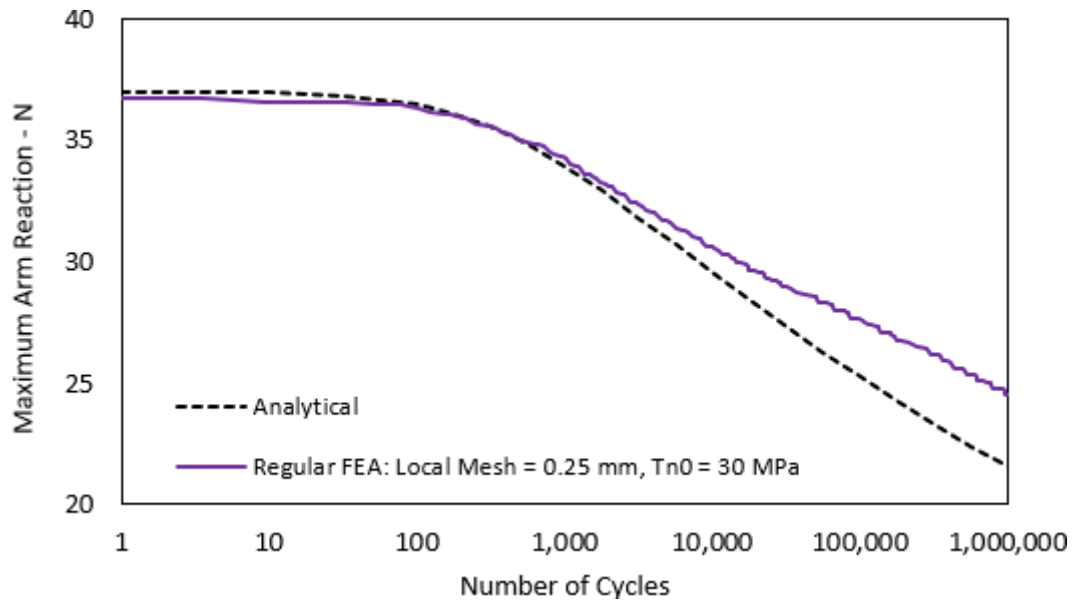


Figure E-3 Fatigue Response of the DCB Model with Local Mesh Size Selection of 0.25 mm without Mesh Regularisation

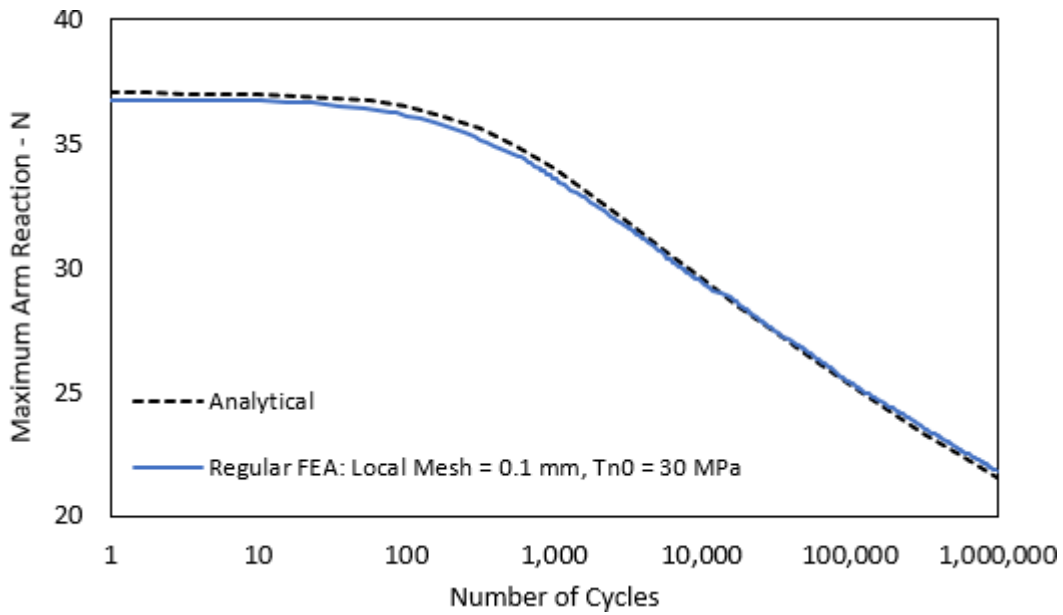


Figure E-4 Fatigue Response of the DCB Model with Local Mesh Size Selection of 0.1 mm without Mesh Regularisation

### Solutions with Mesh Regularisation

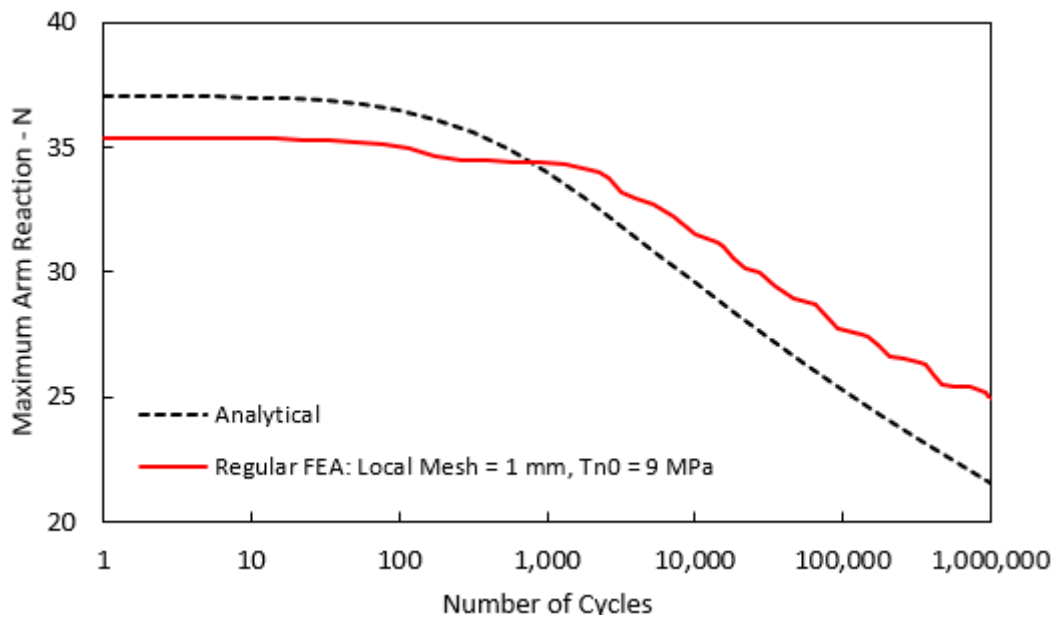


Figure E-5 Fatigue Response of the DCB Model with Local Mesh Size Selection of 1 mm with Mesh Regularisation

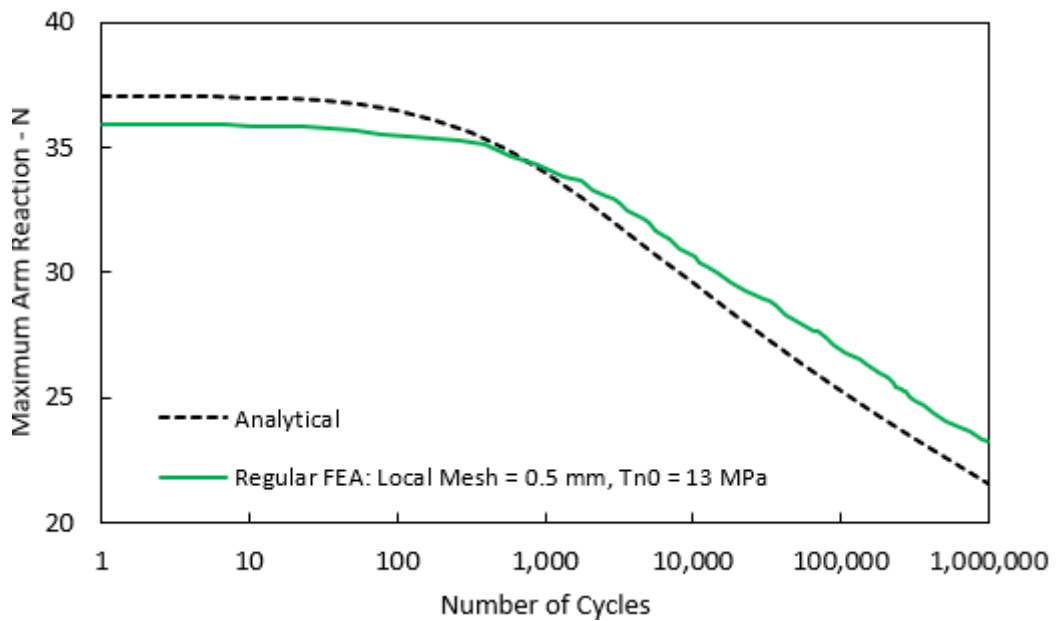


Figure E-6 Fatigue Response of the DCB Model with Local Mesh Size Selection of 0.5 mm with Mesh Regularisation

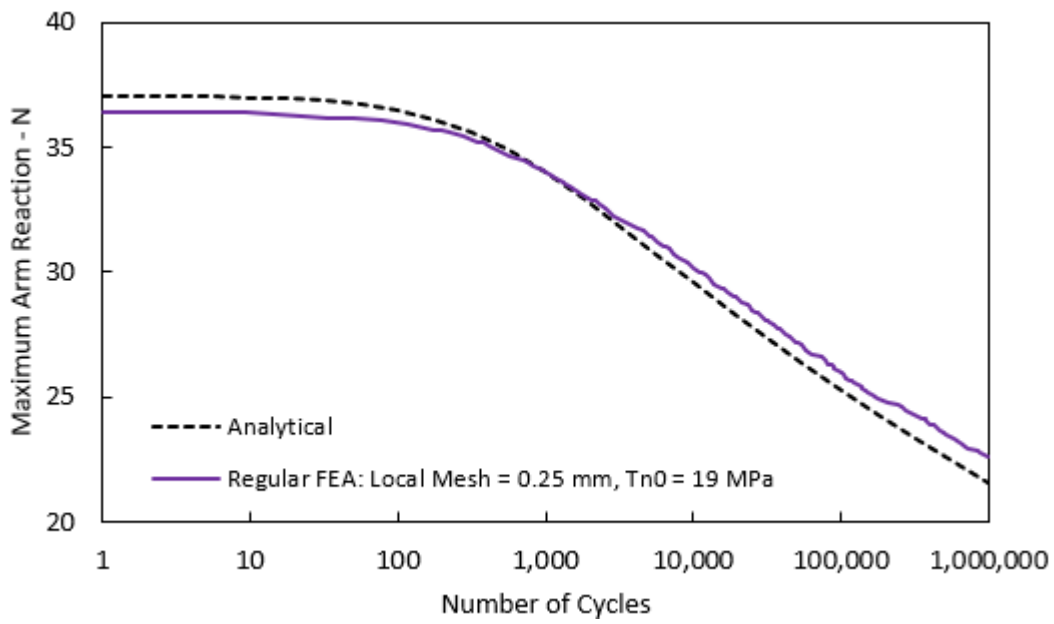


Figure E-7 Static Response of the DCB Model with Local Mesh Size Selection of 0.25 mm with Mesh Regularisation

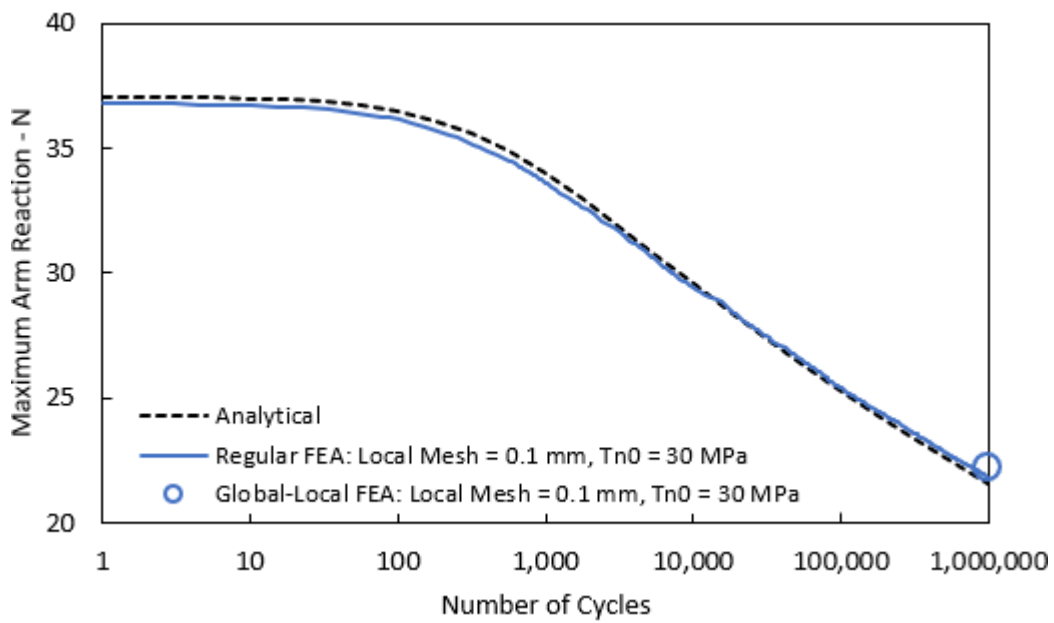


Figure E-8 Fatigue Response of the DCB Model with Local Mesh Size Selection of 0.1 mm with Mesh Regularisation

## CURRICULUM VITAE

Surname, Name: Değerliyurt, Boray

### EDUCATION

Degree	Institution	Year of Graduation
MS	METU Aerospace Engineering	2016
BS	METU Mechanical Engineering	2012
High School	Çankaya Milli Piyango Anadolu High School, Ankara	2007

### FOREIGN LANGUAGES

Advanced English

### INTERNATIONAL JOURNALS

1. Karatas, C., Degerliyurt, B., Yaman, Y. and Sahin, M. (2018), "Fibre Bragg grating sensor applications for structural health monitoring", *Aircraft Engineering and Aerospace Technology*, Vol. 92 No. 3, pp. 355-367, <https://doi.org/10.1108/AEAT-11-2017-0255>.

### INTERNATIONAL CONFERENCES

#### Presented

1. Degerliyurt, B., Sahin, M. (2024), "Investigation of Interlaminar Fatigue Damage Behaviour of Composite Structures via Two-Way Coupling Global-Local Analysis", 9th European Conference on Computational Methods in Applied Science and Engineering – ECCOMAS 2024, Lisbon, Portugal, 3-7 June 2024.

### **Contributed**

1. C. Karataş, B. Değerliyurt, M. Şahin, Y. Yaman, “Fatigue Test of a Structure Instrumented with Fibre Bragg Grating Sensors for Structural Health Monitoring Applications”, 8th Asian/Australian Rotorcraft Forum - ARF2019, Ankara, Turkey, 30 October - 02 November 2019.
2. B. Değerliyurt, C. Karataş, M. Şahin, Y. Yaman, “Comparison of Performance of Surface Mounted and Embedded Fibre Bragg Grating Sensors under Fatigue Torsion Load”, 6th Seoul International Conference on Applied Science and Engineering - SICASE 2019, Seoul, South Korea, 21 - 23 May 2019.
3. C. Karataş, B. Değerliyurt, Y. Yaman, M. Şahin, “Fiber Bragg Grating Sensor Applications for Structural Health Monitoring”, 7th EASN International Conference on Innovation in European Aeronautics Research, Warsaw, Poland, 26 - 29 September 2017.
4. B. Değerliyurt, C. Karataş, M. Şahin, Y. Yaman, “Structural Health Monitoring system of composite beams with surface bonded and embedded Fibre Bragg Grating sensors”, International Symposium on Material Science and Engineering - ISMSE 2017, Kuala-Lumpur, Malaysia, vol.744, pp.332-336, 13 - 15 January 2017.

### **NATIONAL CONFERENCES**

#### **Presented**

1. B. Değerliyurt B., M. Şahin, “Kompozit Yapılarda Birbirine Bağlı Global-Lokal Sonlu Elemanlar Yöntemi İle Katmanlar Arası İlerlemeli Hasar Modellemesi”, 10. Savunma Teknolojileri Kongresi - SAVTEK2022, Ankara, Turkey, pp.461-471, 13 - 15 September 2022.
2. B. Değerliyurt, C. Karataş, Y. Yaman, M. Şahin, “Fiber Bragg Izgara Algılayıcı Kullanılarak Kompozit Kiriş Yapıların Yapısal Sağlığının İzlenmesi”, 8. Savunma Teknolojileri Kongresi - SAVTEK 2016, Ankara, Turkey, 12 - 14 October 2016.
3. B. Değerliyurt, Y. Yaman, M. Şahin, “Kompozit Yapılarda Fiber Optik Algılayıcıların Yarattığı Gerilme Yığılımlarının İncelenmesi”, VI. Ulusal Havacılık ve Uzay Konferansı - UHUK2016, Kocaeli, Turkey, 28 - 30 September 2016.

#### **Contributed**

1. C. Karataş, B. Değerliyurt, Y. Yaman, M. Şahin, “Torsion Test of Composite Beams Using Fiber Bragg Grating Sensors for Structural Health Monitoring Applications”, 9th Ankara International Aerospace Conference, Ankara, Turkey, 20 - 22 September 2017.